Quantum Matter and Tensor Networks in Two Dimensions

Inaugural-Dissertation

zur Erlangung des Doktorgrades
der Mathematisch-Naturwissenschaftlichen Fakultät
der Universität zu Köln

vorgelegt von

Erik Lennart Weerda

aus Hamburg

angenommen im Jahr 2025

Abstract

The numerical study of quantum matter in two dimensions plays an important role in both conventional condensed matter systems and cold atom experiments. In this thesis, we explore the use of two-dimensional tensor networks — specifically, tensor product states — for this task. These states are alternatively referred to as projected entangled-pair states. We present complementary results of methodological advances for tensor product states, together with applications of these states in both finite and infinite lattice systems. On the methodological side, we introduce an accurate and computationally efficient algorithm for the contractions of the relevant two-dimensional tensor networks alongside practical schemes to achieve more efficient optimization of tensor product states. Additionally, we apply the methods of two-dimensional tensor networks to models describing several physical situations, including spin systems, Josephson junction arrays, the bosonic Harper-Hofstader model relevant for cold-atom platforms with synthetic gauge fields, as well as Rydberg atom arrays. The results of this thesis thus contribute to demonstrating and improving the versatility of tensor product states as a framework for addressing complex questions in two-dimensional quantum matter.

Publications

The following journal articles are associated with the research presented in this thesis:

I. *Fractional quantum Hall states with variational projected entangled-pair states: A study of the bosonic Harper-Hofstadter model*
Erik L. Weerda, Matteo Rizzi
Journal reference: Phys. Rev. B 109, L241117 — Chapter 5

II. *Variationally optimizing infinite projected entangled-pair states at large bond dimensions: A split corner transfer matrix renormalization group approach*
Jan Naumann*, **Erik L. Weerda***, Jens Eisert, Matteo Rizzi, Philipp Schmoll
Journal reference: Phys. Rev. B 111, 235116 —Chapter 8

III. *Efficient optimization and conceptual barriers in variational finite Projected Entangled-Pair States*
Daniel Alcalde Puente*, **Erik L. Weerda***, Konrad Schröder, Matteo Rizzi
Journal reference: Phys. Rev. B 111, 195120 —Chapter 9

IV. *An introduction to infinite projected entangled-pair state methods for variational ground state simulations using automatic differentiation*
Jan Naumann*, **Erik L. Weerda***, Matteo Rizzi, Jens Eisert, Philipp Schmoll
Journal reference: SciPost Phys. Lect. Notes 86 —Chapter 11

Additionally, the following preprints contain research presented in this thesis:

I. *Bathing in a sea of candidate quantum spin liquids: From the gapless ruby to the gapped maple-leaf lattice*
Philipp Schmoll*, Jan Naumann*, **Erik L. Weerda**, Jens Eisert, Yasir Iqbal
Arxiv reference: arXiv:2407.07145 — Chapter 7

II. *Triangular lattice models of the Kalmeyer-Laughlin spin liquid from coupled wires*
Tingyu Gao, Niklas Tausendpfund, **Erik L. Weerda**, Matteo Rizzi, David F. Mross
Arxiv reference: arXiv.2502.13223 — Chapter 6

*Both first authors have contributed equally.

Contents

CHAPTER 1

Introduction

In 1972, P. W. Anderson coined the phrase *"more is different"* to highlight that large collections of interacting components of a physical system can give rise to collective phenomena that can be qualitatively different and in practice unpredictable from the properties of the system's components alone [1]. Understanding these emergent collective phenomena in systems of electrons, atoms, or molecules governed by the laws of quantum mechanics is one of the central objectives of modern condensed matter physics. Among the various fascinating phenomena that arise in the collective behaviour of many-component condensed matter systems, some of the most striking examples include Bose-Einstein condensation and superfluidity, superconductivity, and topological order [2, 3, 4, 5].

A variety of theoretical approaches have been employed to gain insight into various aspects of these physical phenomena. One particularly fruitful method has been the construction of quantum state ansätze. These are simple, physically motivated quantum states that capture the essence of underlying physics while retaining a simple, tractable form. Prominent examples of such ansätze include the quantum state proposed by Bardeen, Cooper, and Schrieffer (BCS) to explain superconductivity or Laughlin's state for the fractional quantum Hall effect [6, 7, 8].

Due to their simple form, these quantum states do not capture every microscopic detail of a given physical system- for instance, lattice defects in a piece of superconducting aluminum or particular impurities in a sample of Gallium Arsenide exhibiting the quantum Hall effect. More importantly, however, their simplicity enables the derivation of general macroscopic physical properties. For example, the energy gap of a superconductor or the Hall conductivity of the fractional quantum Hall effect can be understood through these states, making them a powerful tool for describing the fundamental nature of these phenomena.

As such, the use of quantum state ansätze can also be seen in the context of a broader aim of theoretical physics: on one hand, to improve the accuracy of our quantitative understanding of physical systems; on the other, to express the description of nature in simpler conceptual terms.

Systematic Approach to the Construction of Quantum State Ansätze: The Tensor Network Program

The famous examples of quantum state ansätze mentioned above were each motivated by physical insight into the specific systems they were supposed to describe. Around the turn of the 21st century, however, a different, more systematic approach to quantum state ansätze began to emerge, building on ideas connected to the density matrix renormalization group method [9]. This approach gave rise to the ansätze known as the *tensor network states*. The general program of the development of these tensor network states can be understood as research towards answering the following question:

> *Can we systematically construct useful quantum state ansätze, which are of simple enough structure to be efficiently manipulated, while at the same time being expressive enough to describe the low-energy physics of the effective models used in condensed matter physics?*

A large part of the significant advances in this tensor network program can be attributed to the incorporation of concepts and perspectives from quantum information theory [10]. In particular, the analysis of the entanglement scaling of low-energy quantum states of the typically local models describing much of condensed matter physics has allowed the construction of a variety of suitable, new ansätze. By assembling these states as networks of simple tensors, physicists have been able to systematically construct generic quantum states that fulfill the desired entanglement properties. Prominent examples of such tensor network states include matrix product states for one-dimensional systems and tensor product states — also known as projected entangled-pair states — for higher dimensions [11, 12]. Other important constructions include the multiscale entanglement renormalization ansätze or tree tensor network states [13, 14].

All of the tensor network states mentioned above fulfill the central aim of the tensor network program to varying degrees. Their simple network structure enables both structural insight and efficient computational manipulation. These states allow for the calculation of local observables, correlation functions, quasi-particle excitations, and entanglement quantities, and thus help to make detailed predictions about the low-energy behaviour of physical models.

However, the techniques for the practical application of these tensor network states have not reached equal levels of sophistication and utility across all ansätze. Specifically, while significant progress has been made in the development of analytical and numerical methods for the tensor network program in two dimensions, it is not yet on par with the wealth of established, well-tested, and almost universally applicable techniques that have been produced for one dimensional tensor network states like the matrix product states.

Topic and Structure

In this thesis, we aim to advance the tensor network program in two dimensions by focusing on the paradigmatic tensor network states for this setting: the tensor product states. To this end, we present practical computational schemes and novel, efficient algorithms tailored to this ansatz. In addition, we apply the tensor product states in challenging and experimentally relevant scenarios, demonstrating the versatility of this ansatz class in previously unexplored situations. The content of this thesis is structured as follows.

In Part I we provide relevant background and introduce the tensor product state framework. Concretely, we start in Chap. 2 by defining the tensor product states and the relevant related concepts. Afterwards, we contrast the tensor product states with their one-dimensional counterparts, the matrix product states. In Chap. 3 we then highlight illustrative examples and some structures that can be used in the tensor product states. Lastly, we review some of the numerical tools for the tensor product states in Chap. 4.

Part II contains a presentation of the results obtained in the context of this thesis. We start with the application of the tensor product states, in the thermodynamic limit, to the bosonic Harper-Hofstadter model in Chap. 5. This model describes interacting bosonic particles on a lattice subject to a perpendicular magnetic field, and to date of publication has not been investigated using tensor product states. It is of particular interest as it is relevant to current efforts in cold atom experiments aimed at preparing fractional quantum Hall states. However, representing these chiral, topological quantum states using tensor product states has proven very difficult in the past, as we discuss in Sec. 3.2.4 of Part I. Despite that, using state-of-the-art gradient-based optimization, cf. Sec. 4.2.2, for the translation invariant tensor product states, we were able to successfully identify parameter regimes stabilizing the desired fractional quantum Hall states

in the thermodynamic limit.

The two following chapters concern the application of this gradient-based optimization framework for spin models. In Chap. 6, we investigate a model based on a construction of coupled wires and discuss the possibility of it hosting a chiral spin liquid as its ground state. After this, we present an investigation of the spin-$\frac{1}{2}$ Heisenberg model on the generalized maple-leaf lattice in Chap. 7 and consider the possibility of spin liquid ground states in this scenario.

We then turn to the presentation of methodological results in the context of tensor product states. As we discuss in Sec. 4.1, a central bottleneck for the application of infinite tensor product states is the contraction of the corresponding tensor networks. In Chap. 8, we present a modification of the corner transfer matrix renormalization group (CTMRG) algorithm that is conventionally used for this task. Our proposed algorithm maintains the high accuracy of the CTMRG scheme while drastically reducing the computational cost.

Next, we move from the context of infinite tensor product states, which has been the setting of the previous chapters, to the treatment of tensor product states on finite lattices in Chap. 9. Here, we propose efficient optimization schemes and analyze the difficulty of contracting the corresponding tensor networks in this use case. We also demonstrate the utility of the presented finite tensor product state framework in several situations, particularly for describing the quantum states in Rydberg atom arrays.

A different approach based on using two-dimensional tensor networks is pursued in addition to the tensor product states in Chap. 10. Here we investigate a model describing Josephson junction arrays on a dice lattice in a perpendicular magnetic field and use, among other methods, a tensor network representation of the partition function to investigate the phases of this system.

Lastly, we present practical computational schemes and a pedagogical introduction into the framework of gradient-based ground state search using infinite tensor product states in Chap 11.

We discuss the results obtained in this thesis in Chap. 12.

Part I.

BACKGROUND

CHAPTER 2

Basics for Tensor Product States

In this chapter, we will introduce the tensor product states. To do so, we introduce some fundamental definitions and corresponding notation in Sec. 2.1. With these definitions, we will proceed to discuss the tensor product states and the elementary concepts associated with them in Sec. 2.2. Finally, we discuss the justifaction for the tensor product state ansatz in the context of quantum many-body physics in Sec. 2.3 and close this section with a brief comparison of the tensor product states and their one-dimensional counterparts, the matrix product states in Sec. 2.4.

2.1 Definitions, Notations, and Fundamental Operations

The central objects of interest in the study and application of tensor networks are the eponymous tensors. In this section, we will briefly introduce the relevant definitions and fundamental operations used in this thesis. Further, to keep track of more complex expressions, it is often helpful to introduce a graphical representation for the mathematical objects and operations under consideration. Therefore, we will present the graphical representations alongside our discussion of the basic definitions[1].

2.1.1 Multi-Dimensional Arrays

We start by considering tensors as multi-dimensional arrays of numbers, essentially generalizing the picture of vectors (one-dimensional arrays of numbers) and matrices (two-

[1] These basic definitions and notations have been covered in some detail in many reviews [15, 16, 17, 18, 19, 20].

dimensional arrays of numbers). As such, the elements of the tensor T can be indexed by a set of integers $i_1, \ldots, i_n$ and its corresponding entries are usually real- (or complex) numbers

$$T_{i_1 \ldots i_n} \in \mathbb{R} \text{ (or } \mathbb{C}). \tag{2.1}$$

We graphically illustrate a tensor by a shape (here a circle) with the number of legs corresponding to the number of indices used to label its elements

$T_{i_1 i_2 \ldots i_n} =$ 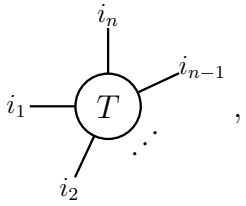

, (2.2)

$T =$ 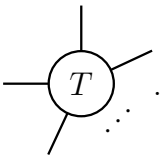

.

Whenever an index on a leg of the tensor is shown explicitly, this indicates that we fixed this index to a specific number. Hence, by labeling all legs of the shape representing the tensor, we obtain a scalar entry of the tensor.

The dimensionality of the array of numbers, or equivalently the number of integers n we are using to index the entries of the tensor, is referred to as the *rank* of the tensor. Every one of the indices i_m that we are using in the labeling of the entries of our tensor T can take the values in the set of the first $|i_m|$ integers $\{1, \ldots, |i_m|\}$. We say this index has *dimension* $|i_m|$. The choice of indexing the elements of the tensor T with a set of n indices $i_1, \ldots, i_n$, each of them of dimension $|i_1|, \ldots, |i_n|$, is of course not unique. Rather one can combine two indices i_k and i_l to a new index j_{kl}

$$T_{i_1 i_2 \ldots i_n} = \widetilde{T}_{(i_1, i_2) \ldots i_n} = \widetilde{T}_{j_{12} \ldots i_n}$$

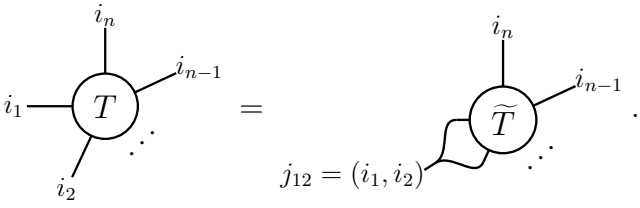

. (2.3)

As indicated in the above equation this new index j_{kl} enumerates the set of possible tuples

(i_k, i_l) of the values of i_k and i_l and hence has dimension $|j_{kl}| = |i_k| \times |i_l|$. Analogously, one can combine even more indices into one. Equivalently, one can also reverse this procedure and separate an single index j of dimension $|j| = n_1 \times n_2$, where $n_1, n_2 \in \mathbb{N}$ into two indices i_1 and i_2 of dimension $|i_1| = n_1$ and $|i_2| = n_2$ respectively. Beyond combining and separating indices of a tensor, we can also change the order of the set of indices that we use to label the entries of the tensor

$$T_{i_1 i_2 \dots i_n} = \widetilde{T}_{i_2 i_1 \dots i_n}$$

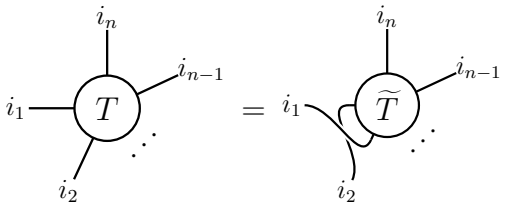

(2.4)

In light of this, the property of the rank of the tensor T and the dimension of its indices are properties of our choice of labeling we made for it. What remains invariant under the combination and separation of indices, as well as under permutation of the order of indices, however, is the product of the dimensions of all indices $|i_1| \times \cdots \times |i_n|$ used to label the tensor.

A most elementary operation that can be used with matrices and vectors is their multiplication, e.g.

$$\begin{aligned} (MN)_{ik} &= \sum_j M_{ij} N_{jk} = O_{ik}, \\ (Mv)_i &= \sum_j M_{ij} v_j = w_i. \end{aligned} \tag{2.5}$$

We extend the graphical notation introduced above by illustrating the sum over a common index of matrices or vectors by a leg that is connected on both ends to a matrix or vector, such that we obtain for the examples above

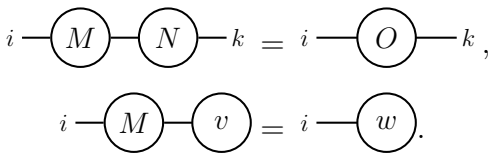

(2.6)

In this spirit, we can define a product of two tensors T and S, referred to as a contraction, by specifying a set of indices on each of the two tensors that have equal dimension and

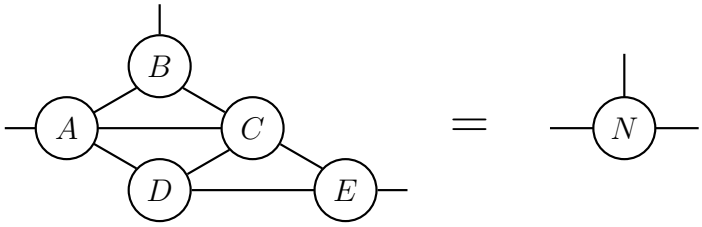

Figure 2.1.: Graphical representation of a contraction of a set of five tensors.

summing over these indices

$$\sum_k T_{i,j,k,l} S_{k,m,n} = U_{i,j,l,m,n},$$

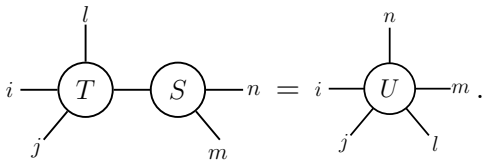

(2.7)

It is clear that one can get, e.g., the standard matrix multiplication in this form by restricting to rank-two tensors and possibly permuting the order of the indices beforehand. Other common operations are traces of matrices or partial traces of tensors, e.g.

$$\mathrm{Tr}(M) = \sum_i M_{ii} =$$

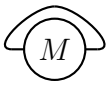

$$(\mathrm{pTr}_i(T))_k = \sum_i T_{i,i,k} =$$

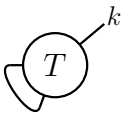

(2.8)

The utility of the graphical notation introduced above becomes obvious once we are treating more complex contractions of multiple tensors. Such a network of tensors over which a contraction is performed is commonly referred to as a *tensor network*. An example of a tensor network is shown in Fig. 2.1. The advantage of this graphical representation is that the structure of the contraction is apparent, while it becomes increasingly hard to track in an equation using the index expression.

In the tensor network literature, we often find an additional notation for the contraction of a tensor network called the *tensor trace*. Here, all indices that are contracted in the tensor network are suppressed, and only the ones that remain after the contraction are shown. We note that this notation suppresses the concrete pairing of the contracted indices, which are assumed to be known from the context or the graphical representa-

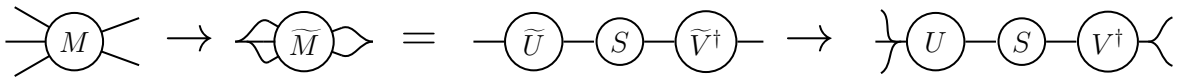

Figure 2.2.: Singular value decomposition of a higher rank tensor. The legs of the tensor M are grouped such that the resulting object $\widetilde{M}$ is a matrix. The SVD is performed on the matrix $\widetilde{M}$, after which the legs are separated again to yield an SVD of the original tensor.

tion. For example, we could denote the elements of the tensor network in Fig. 2.1 using the tensor trace notation

$$\mathrm{tTr}(A_i B_k C D E_j) = N_{ijk}. \tag{2.9}$$

It is worth mentioning that the computational cost of contracting a tensor network will generically depend strongly on the order in which the different sums over indices are performed. While finding the optimal contraction order in general is a hard problem [21], for tensor networks appearing in algorithms used in practice, we can, in most instances, easily find such an optimal contraction order.

2.1.2 Factorizations

In many applications, it is crucial to be able to factorize the tensors at hand. In the study of linear algebra, a multitude of possible factorizations are known for matrices, among which the QR-decomposition, polar decomposition, eigenvalue decomposition, and the singular value decomposition (SVD) are prominent examples.

These matrix factorizations can be easily extended to the realm of tensors. This works simply by permuting and combining the indices of the tensors, which we aim to decompose, until we have reached the form of a rank-two tensor, or a matrix. We can then apply the factorizations in this matrix form and afterwards reverse the permutation and combination of indices, such that we end up with the index structure of the tensor we started with. This procedure is illustrated in Fig. 2.2 for the example of an SVD.

The SVD is a factorization that is of particular importance to the tensor network methods studied in this thesis. A SVD can be performed on any rectangular matrix $M \in \mathrm{Mat}_{n\times m}$ of size $n \times m$

$$M = USV^\dagger, \tag{2.10}$$

and factorizes the matrix into a matrix U of size $n \times \min(n, m)$ composed of orthonormal columns, matrix $V^\dagger$ of size $\min(n, m) \times m$ and made up of orthonormal rows as well as a diagonal matrix S with non-negative entries, which are refered to as *singular values*.

As U and V are made up of orthonormal columns, they fulfill $U^\dagger U = \mathbb{1}$ and $V^\dagger V = \mathbb{1}$ and are unitary in the case of quadratic matrices.

The central importance of the SVD in the tensor network program derives from the fact that it can be used to generate *optimal*, low-rank approximations of matrices. This works by truncating the matrix S in the SVD to the k largest singular values, setting all others to zero, which we denote $S^{(k)}$. The resulting rank-k-approximation of the matrix M

$$M^{(k)} = US^{(k)}V^\dagger \tag{2.11}$$

is optimal as measured by any unitarily invariant norm [22], e.g. the Frobenius norm

$$||M - M^{(k)}||_F \leq ||M - N||_F, \quad \forall\, N \in \{W \in \mathrm{Mat}_{n\times m} | \mathrm{rank}(W) = k\}. \tag{2.12}$$

We will illustrate how this matrix factorization is related to approximations of quantum states and their entanglement in Sec. 2.3, where it is referred to as the *Schmidt-decomposition*. In almost all tensor network algorithms discussed in this thesis, cf. Chap. 2.3, we will make use of this decomposition.

2.1.3 Linear Maps

Oftentimes, in the context of quantum mechanics, it can be useful to keep track of some additional structure when talking about the tensors in our tensor networks. Specifically, to distinguish between (*ket*-) vectors and (*bra*-) dual-vectors and maps between these objects, we can reinterpret the arrays of numbers, which we have so far called tensors, as representations of more general, linear maps between vector spaces. The multi-dimensional arrays then emerge from these linear maps with the choice of a specific basis for the vector spaces. This can help to keep our notation clearer and avoid ambiguities.

To this end, we remind ourselves of the isomorphism $\mathrm{Hom}(V, W) \cong \mathrm{Mat}_{m,n}$ between linear maps $\mathrm{Hom}(V, W)$ from vector space V to W, and $n \times m$-matrices $\mathrm{Mat}_{m,n}$, where n and m are the dimensions of the vector spaces V and W respectively. This isomorphism establishes that upon choosing an arbitrary basis for V and W, we can use the matrices $\mathrm{Mat}_{m,n}$ to represent the linear maps between the two vector spaces. This picture is easily extended to the multi-dimensional arrays of numbers we have considered before, by choosing for the vector spaces V and W an additional tensor product substructure, e.g. $V = V_1 \otimes ... \otimes V_k$. Here we proclaimed that V is a tensor product space of k individual vector spaces $V_1, ..., V_k$. While we can represent any vector in this tensor product space V as a standard vector of dimension $n = \dim(V_1) \cdot ... \cdot \dim(V_k)$, we can always reshape

it into a different form, e.g. a k-dimensional array. This is achieved by separating the single index into k different ones, each of which is of the dimension of one of the corresponding vector spaces V_i in the tensor product of $V = V_1 \otimes ... \otimes V_k$. Naturally, this extends also to matrices mapping between these tensor product spaces, such that we can describe them as the multi-dimensional objects introduced as tensors in the perspective discussed in Sec. 2.1.1.

To introduce relevant notation, we examine a linear map between tensor product spaces (colloquially called a tensor)

$$T : V_1 \otimes V_2 \to W_1 \otimes W_2, \quad |v_1\rangle \otimes |v_2\rangle \mapsto |w_1\rangle \otimes |w_2\rangle \,, \tag{2.13}$$

where $|v_i\rangle \in V_i$, $|w_i\rangle \in W_i$ for $i \in \{1, 2\}$. In this context, we refer to the space $V_1 \otimes V_2$ as the *domain* of T, while the space $W_1 \otimes W_2$ is referred to as the *codomain*.

We can express this map[2] in the slightly different form

$$T = \sum_{a,b,c,d} T^{ab}{}_{cd} \, |a\rangle \, |b\rangle \, \langle c| \, \langle d| \,; \quad |a\rangle \in W_1 \, |b\rangle \in W_2, \langle c| \in V_2^*, \langle d| \in V_1^*, \tag{2.14}$$

where we additionally suppress the explicit notation of the tensor products. Notice that in the above equation, we have introduced a convention for distinguishing indices corresponding to vector spaces from those corresponding to dual-vector spaces. For $T \in W_1 \otimes W_2 \otimes V_2^* \otimes V_1^*$, we distinguish between vector spaces and dual-vector spaces by writing the indices of vector spaces as superscript, while writing the ones from the dual-vector spaces as subscript. This can be useful to avoid ill-defined contractions and, additionally, can be used to remind ourselves that the dual-vectors transform contragredient to the vectors under basis transformations.

In order to graphically represent the additional mathematical structure that we introduced for the tensors above, we will highlight the legs corresponding to the subscript indices in the tensor with a directionality pointing into the tensor. Superscript indices

[2] By the isomorphism $\mathrm{Hom}(V, W) \cong W \otimes V^*$ we can move spaces V from domain to codomain and vice versa.

will be illustrated with a directionality out of the tensor

$$T^{ab}{}_{cd} = \quad (2.15)$$

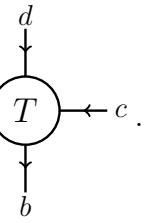

An object that is frequently used in the context of tensor product states is the conjugate tensor of the tensor T from Eq. (2.14). We denote this conjugate tensor as

$$\bar{T} = \sum_{e,f,g,h} \bar{T}^{ef}{}_{gh} \left|e\right\rangle \left|f\right\rangle \left\langle g\right| \left\langle h\right| ; \quad \left|e\right\rangle \in V_1 \left|f\right\rangle \in V_2, \left\langle g\right| \in W_2^*, \left\langle h\right| \in W_1^* \\ \text{with} \quad \bar{T}^{ef}{}_{gh} = (T^{hg}{}_{fe})^*. \quad (2.16)$$

Finally, we mention that all of the manipulations of the tensors we have discussed in Sec. 2.1.1 and 2.1.2, such as combining and seperating indices, their permutation as well as factorizations carry over into the framework if linear maps.

On the Relation of the Different Conventions

Let us stress that one can easily switch between expressions written in the notation of arrays and those of linear maps and vector spaces. For example, take an expression written in the notation of linear maps, with arrows on the legs of the tensors in the graphical notation. By just eliminating all arrows on the legs in the graphical notation and writing all indices as subscripts, we obtain the corresponding expression in the notation of multi-dimensional arrays. Conversely, if we want to promote an expression written in the notation of multi-dimensional arrays to an expression of linear maps, we just have to choose which indices label vector spaces and which label dual vector spaces for every tensor in the network in the form of Eq. (2.14). This has to be done in a way such that every contraction in the tensor network includes a vector and a dual vector.

Graphically, this just amounts to putting arrows on every leg of the graphical expressions in a consistent way, meaning equal indices on both sides of the equation need to be given arrows in the same direction.

In this thesis, we mostly drop the arrows on the graphical representations if the corresponding equations shown do not explicitly involve *bra*- or *ket* notation.

2.2 Basics of tensor product states

After having introduced the definitions and some of the properties of the mathematical objects useful for our discussion, we will, in this section, describe the basics of tensor product states, focusing exclusively on a two-dimensional setting. We further restrict the discussion to quantum states of bosonic degrees of freedom, noting that for the treatment of fermions, additional techniques have to be employed to account for the anti-commutation relations of fermions [17, 23, 24, 25, 26, 27, 28]. Tensor product states were originally introduced by Verstraete and Cirac in 2004 [12] and are part of the family of many-body states referred to as tensor network states [16, 18, 19]. All of these tensor network states are fundamentally state vectors in a many-body Hilbert space. A general state vector in such a many-body Hilbert space can be written as

$$|\psi\rangle = \sum_{s_1,\ldots,s_N} C^{s_1,\ldots,s_N} |s_1 \ldots s_N\rangle \,, \tag{2.17}$$

where the indices $s_i \in \{1, \ldots, d\}$ of the coefficient tensor $C^{s_1,\ldots,s_N}$ label the basis states of a d-dimensional local Hilbert space $\mathcal{H}_i$. The many-body Hilbert space $\mathscr{H}$ is the tensor product of N of these local Hilbert spaces

$$\mathscr{H} = \bigotimes_{i=1}^{N} \mathcal{H}_i. \tag{2.18}$$

The central problem of a quantum mechanical description in a many-body problem is the dimensionality of the many-body Hilbert space $\dim(\mathscr{H}) = d^N$, which grows exponentially with the number of constituents N in the system under consideration. The strategy of tensor network states in general and tensor product states in particular is to build the rank N coefficient tensor $C^{s_1,\ldots,s_N}$ from a collection of lower rank tensors. This is computationally advantageous as it drastically reduces the number of independent coefficients in the coefficient tensor of the many-body state vector. Remarkably, such a reduction in the number of parameters can be physically justified in the study of low-energy states of local quantum many-body systems, as we shall discuss in Sec. 2.3.

For the construction of the tensor product states [12, 29] we start with its fundamental

building block, the *local tensor*

$$A = \sum_{\alpha,\beta,\gamma,\delta,p} A^{p\alpha\beta}{}_{\gamma\delta} \left|p\right\rangle \left|\alpha\right\rangle \left|\beta\right\rangle \left\langle\gamma\right| \left\langle\delta\right| .$$

$$A^{p\alpha\beta}{}_{\gamma\delta} = \quad (2.19)$$

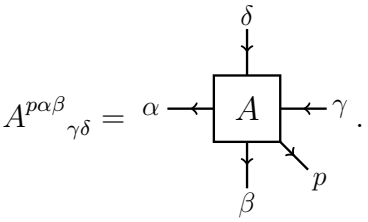

While the index p labels the basis of one of the *local* Hilbert spaces of the many-body Hilbert space under consideration, the Greek letters label indices that correspond to *virtual* spaces. We refer to all vector spaces associated with the local tensor, which are not a local Hilbert space of the physical system, as *virtual* spaces. The dimension of these virtual spaces is denoted by χ_B, and we refer to this dimensionality as the *bond dimension*. The tensor product states are then defined by a contraction over the virtual indices of many local tensors

$$\left|\psi_{\mathrm{TPS}}\right\rangle = \sum_{\{s_i\}} \mathrm{tTr}\left[\prod_i A[i]^{s_i}\right] \left|\{s_i\}\right\rangle .$$

$$\mathrm{tTr}\left[\prod_i A[i]^{s_i}\right] = \quad (2.20)$$

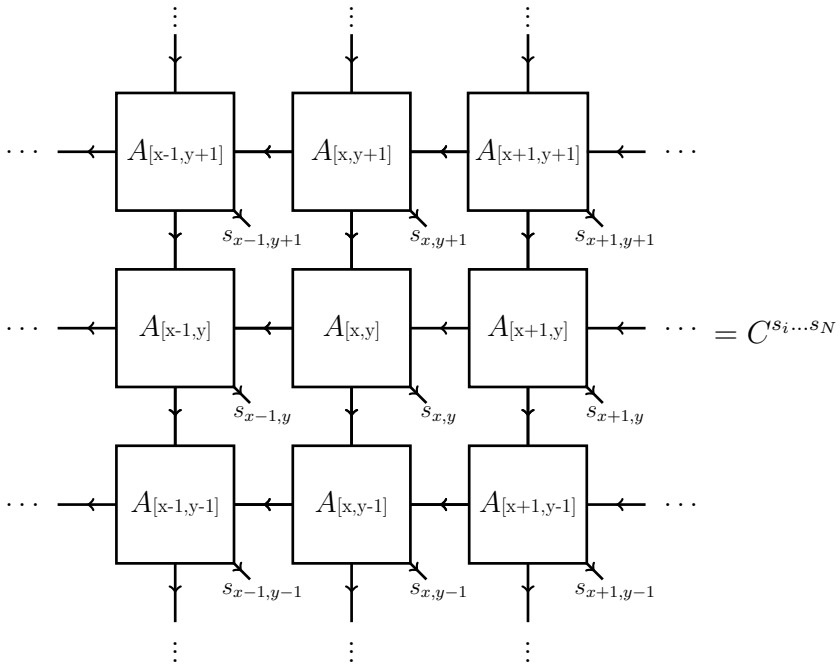

Note that the tensor trace, as defined in Sec. 2.1.1, is used to contract all virtual indices

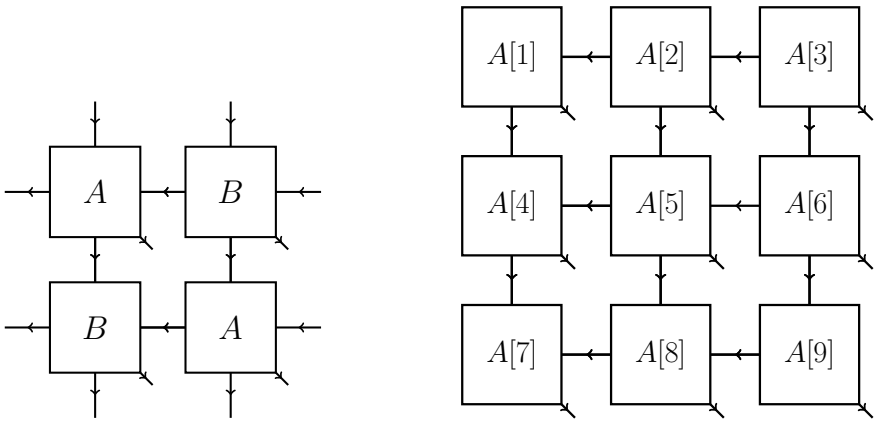

Figure 2.3.: (a) Illustration of 2×2 unit cell for a translation-invariant tensor product state on a square lattice. This structure of two independent local tensors is repeated throughout the lattice to achieve the infinite tensor product state. (b) Illustration of a tensor product state defined on a small 3×3 lattice with open boundary conditions. The tensors on every site can be chosen independently, and the local tensors on the boundary have a smaller rank.

of the tensors $A[i]$, as illustrated graphically. We specify the tensor $A[i]$ with the label of the physical Hilbert space it attaches to, to highlight that, in principle, every local tensor can be chosen independently on every site. At this point, we further note that the number of independent coefficients in the coefficient tensor of the many-body state vector is reduced from a number d^N exponential in the number of constituents, to $Nd\chi_B^4$, which is linear in the number of constituents of our system. We may already superficially observe that a many-body state defined in this form is natural from the perspective that its coefficient tensor has some correspondence to the local lattice structure on which the quantum system is set. In the above definition of the tensor product state, we have used the square lattice as a canonical example, but we stress that indeed the definition can be analogously carried out on other lattices in two dimensions.

Within the general definition of the tensor product states, we gave in Eq. (2.20), it is useful to distinguish two different cases for practical use:

2.2.1 Infinite Tensor Product States

The infinite tensor product states are defined in the thermodynamic limit, meaning on infinite two-dimensional lattices [29]. To obtain an ansatz with a finite number of variational parameters, we usually restrict to translation-invariant states. To construct

these translation-invariant states, we define a unit cell of local tensors of size $L_x \times L_y$, which we repeat periodically on the infinite lattice.

When performing calculations with the infinite tensor product states, the structure of the unit cell is often associated with the targeting of specific kinds of ground states. With an alternating unit cell, as illustrated in Fig. 2.3a, one could, for example, target a quantum state with antiferromagnetic order, while for a state with ferromagnetic order, a single repeating tensor is sufficient. It is worth highlighting that the tensor product states, defined in this way, have only a constant number of independent parameters in their coefficient tensor.

Let us stress that the infinite tensor product states are particularly appealing as a tool for investigations of ground state phase diagrams of two-dimensional quantum many-body systems, as they offer a pathway for numerical calculations directly in the thermodynamic limit. On the other hand, the infinite nature of this ansatz poses some particular challenges, e.g., for the contraction of the tensor network, which is generically required for the calculation of observables. A set of numerical techniques for this task is introduced in Chap. 4 of this thesis. We further note that the infinite tensor product states are the main theoretical approach employed in this thesis, and we refer to publications [P1,P2,P3] for application of these quantum states and to publications [P4,P6] for methodological investigations.

2.2.2 Finite Tensor Product States

In case the model of interest is defined on a finite lattice, as might be interesting for mesoscopic systems or for digital twins of cold atom experiments, the scheme of employing tensor product states works by defining an individual local tensor for every site on the lattice. Special care has to be given to the tensors located at the boundary of a finite lattice when we define a tensor product state with open boundary conditions. Here, as these lattice sites have a limited number of nearest neighbors, we employ lower rank tensors as illustrated in Fig. 2.3b.

The finite tensor product states have received renewed interest as a numerical tool, after it has been shown that an approach based on sampling techniques can be employed to great effect [30, 31, 32, 33]. In publication [P5], we investigate some conceptual questions regarding this sampling approach and further apply it, among other things, to the study of long-range interacting Rydberg atom arrays.

2.2.3 Gauge Freedom in Tensor Product States

As the formulation of the tensor product states involves the contraction of several local tensors, there is an additional freedom we have in manipulating the corresponding expressions without changing the resulting states. This is, in this context, referred to as *gauge freedom*. Concretely, this freedom can be illustrated by noting that we can insert into a matrix multiplication of two matrices $A, B \in Mat_{n\times n}(\mathbb{C})$, a suitable invertible matrix $M \in GL_{n\times n}(\mathbb{C})$ and its inverse M^{-1} without changing the result

$$AB = (AM)(M^{-1}B) = \tilde{A}\tilde{B}. \tag{2.21}$$

In complete analogy, whenever we sum over a common index in a tensor network contraction, we may insert a matrix and its inverse without changing the result

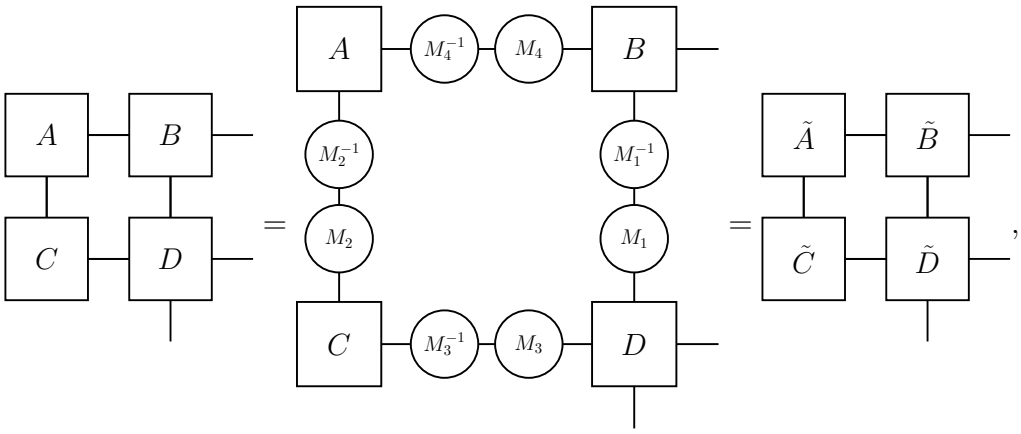

(2.22)

where the new tensors $\tilde{A}, \tilde{B}, \tilde{C}$ and $\tilde{D}$ are obtained by absorbing their neighboring invertible matrices in analogy to Eq. (2.21). As illustrated by the above equation, this gauge freedom defines different sets of tensors that are related to one another by gauge transformations and yield the same result upon contraction. It is clear that these gauge transformations can be applied to the coefficient tensors of many-body quantum states if we represent them as a tensor network.

In the study of loop-free tensor network states, like matrix product states or tree-tensor networks, particular gauge choices, referred to as canonical gauges, can be utilized in numerical calculations as well as in analytical considerations to great effect [15, 16]. In contrast to this, for tensor product states, an analogous canonical gauge does not exist, in the most general setting[3].

[3]We note, however, that approaches towards defining useful subclasses of tensor product states where such canonical gauges are possible are actively pursued [34, 35].

2.2.4 Norm and Observables

In order to use the tensor product states for the investigation of the ground states of quantum many-body systems, it is critical to be able to evaluate physical observables, e.g., expectation values of local operators. For this, it is useful to introduce some additional concepts. Given a tensor product state, we define for each local tensor A a *double-layer* tensor

$$\mathbb{A}^{\delta'\gamma'}{}_{\beta'\alpha'}{}^{\alpha\beta}{}_{\gamma\delta} := \sum_p \bar{A}^{\delta'\gamma'}{}_{\beta'\alpha'p} A^{p\alpha\beta}{}_{\gamma\delta}$$

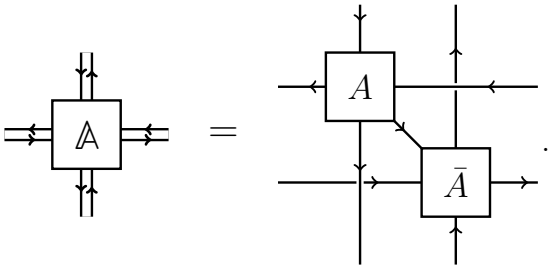

(2.23)

With this tensor at hand, we can express the norm of the tensor product state as

$$\langle \psi_{\mathrm{TPS}} | \psi_{\mathrm{TPS}} \rangle = \mathrm{tTr}\left[\prod_i \mathbb{A}[i] \right], \tag{2.24}$$

where the product runs over all local sites in the lattice. For the expression of local observables, we additionally define the double layer tensor with local operator $\hat{O}$

$$(\mathbb{A}_{\hat{O}})^{\delta'\gamma'}{}_{\beta'\alpha'}{}^{\alpha\beta}{}_{\gamma\delta} := \sum_{p,p'} \bar{A}^{\delta'\gamma'}{}_{\beta'\alpha'p'} \hat{O}^{p'}{}_{p} A^{p\alpha\beta}{}_{\gamma\delta}$$

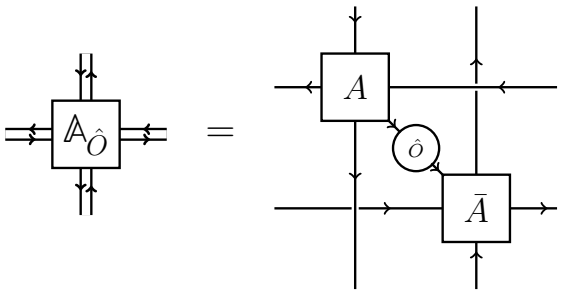

(2.25)

Hence, the expression for the expectation value of a local observable can be written as

$$\frac{\langle\psi_{\mathrm{TPS}}|\hat{O}_i|\psi_{\mathrm{TPS}}\rangle}{\langle\psi_{\mathrm{TPS}}|\psi_{\mathrm{TPS}}\rangle} = \frac{\mathrm{tTr}\left[\prod_{j\neq i}\mathbb{A}[j]\mathbb{A}_{\hat{O}}[i]\right]}{\mathrm{tTr}\left[\prod_{j}\mathbb{A}[j]\right]}$$

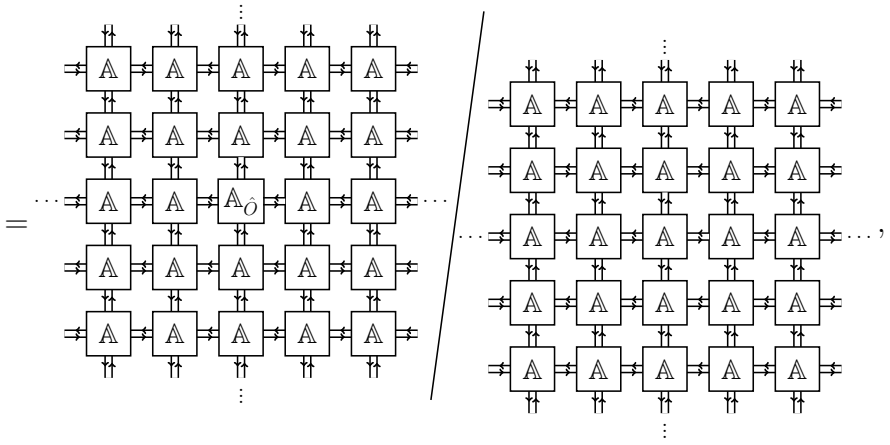

(2.26)

where we have suppressed the index labeling the sites in the graphical notation. The expressions given above for the calculations of norms and observables highlight the structure of these equations. However, they are generically very difficult to evaluate exactly, and we refer to Chap. 4 for the elaboration on how to perform computations with these expressions in a numerical setting.

2.2.5 Projected Entangled-Pair Picture

In the literature that utilizes or studies tensor product states in two-dimensional settings, they are oftentimes referred to as *projected entangled-pair states* [19, 12]. This name remains, most likely for historical reasons, quite popular. However, this name also hints at a particular procedure that can be used to construct tensor product states and can highlight some of their properties, as well as some philosophically interesting observations on long-range entanglement and projective measurements.

To review the *projected entangled-pair state* construction, we start by introducing a maximally entangled state

$$|\mathrm{EP}\rangle = \frac{1}{\sqrt{2}}(|00\rangle + |11\rangle) = \frac{1}{\sqrt{2}}\sum_{s_1,s_2}\delta^{s_1 s_2}\,|s_1 s_2\rangle\,, \tag{2.27}$$

which we exemplify here for a spin-$\frac{1}{2}$ system, but can be analogously defined on larger

local Hilbert spaces. Given such an entangled-pair state $|\mathrm{EP}\rangle$ we proceed by decomposing its coefficient tensor into two parts

$$\delta^{s_1 s_2} = \sum_{\lambda} \delta^{s_1}{}_{\lambda} \delta^{\lambda s_2} = \quad . \tag{2.28}$$

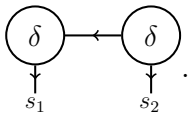

We can now assign one of these entangled-pair states to every edge of the lattice on which we want to define the tensor product state. The two spins that make up the entangled pair on one of the edges are associated with the vertices of the edge. The resulting state, where e labels the edges of the lattice

$$|\phi_{\mathrm{EP}}\rangle = \prod_{e} |\mathrm{EP}\rangle_e \,, \tag{2.29}$$

is graphically illustrated in Fig. 2.4a.

In order to assemble a tensor product state from this rather simple state $|\phi_{\mathrm{EP}}\rangle$, we define a linear map

$$P : V_{\mathrm{up}} \otimes V_{\mathrm{right}} \otimes V_{\mathrm{down}} \otimes V_{\mathrm{left}} \to V_{\mathrm{phys}} \tag{2.30}$$

$$P = \sum P^{p}{}_{\sigma_{\mathrm{l}}\sigma_{\mathrm{d}}\sigma_{\mathrm{r}}\sigma_{\mathrm{u}}} |p\rangle \langle\sigma_{\mathrm{l}}| \langle\sigma_{\mathrm{d}}| \langle\sigma_{\mathrm{r}}| \langle\sigma_{\mathrm{u}}| \tag{2.31}$$

for every site of the lattice on which we want to set up our tensor product state. In the above equation we gave, for concreteness, an example for the square lattice but stress the fact that this construction works analogously, independent of a specific lattice structure or its dimensionality.

At this point, we make use of the decomposition shown in Eq. (2.28). This allows us to construct exactly the object we defined as the local tensor, cf. Eq. (2.19) when introducing the tensor product states

$$A = \sum_{\lambda,p} \underbrace{\sum_{\sigma} P^{p}{}_{\sigma_{\mathrm{l}}\sigma_{\mathrm{d}}\sigma_{\mathrm{r}}\sigma_{\mathrm{u}}} \delta^{\lambda_{\mathrm{l}}\sigma_1} \delta^{\lambda_{\mathrm{d}}\sigma_s} \delta^{\sigma_r}{}_{\lambda_{\mathrm{r}}} \delta^{\sigma_u}{}_{\lambda_{\mathrm{u}}}}_{=:A^{p\lambda_{\mathrm{l}}\lambda_{\mathrm{d}}}{}_{\lambda_{\mathrm{r}}\lambda_{\mathrm{u}}}} |p\rangle |\lambda_{\mathrm{l}}\rangle |\lambda_{\mathrm{d}}\rangle \langle\lambda_{\mathrm{r}}| \langle\lambda_{\mathrm{u}}| \,, \tag{2.32}$$

which we graphically represent in Fig. 2.4b. It is clear that if we apply such projectors

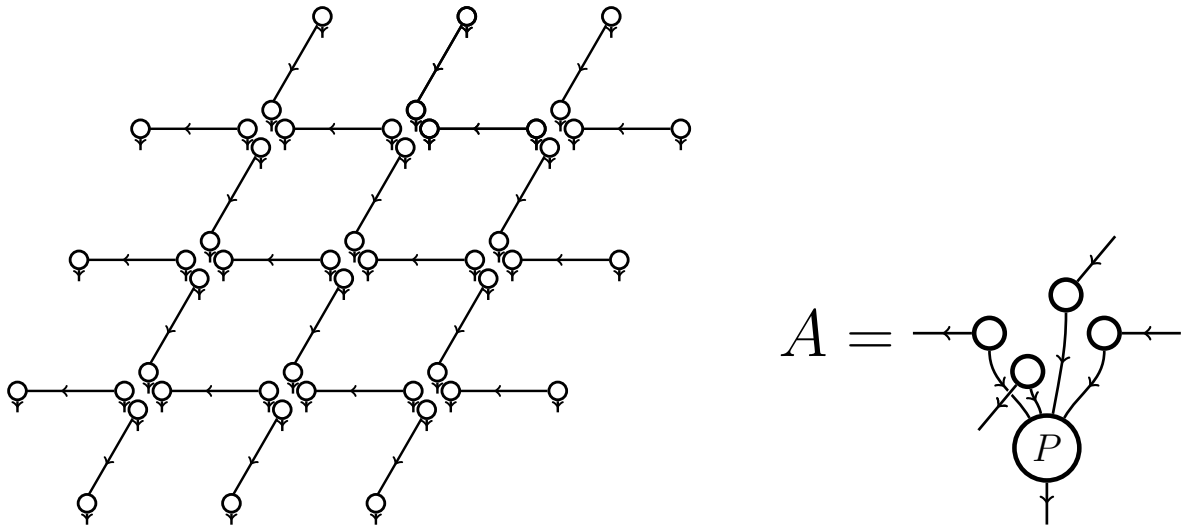

(a) (b)

Figure 2.4.: (a) Graphical representation of the state $|\phi_{\mathrm{EP}}\rangle$ on the square lattice. We show one entangled pair state for every edge of the lattice. (b) Construction of the local tensor of the tensor product state with the use of the linear map that projects from the virtual to the physical spaces.

onto every site of the lattice in question, we end up with a tensor product state

$$|\psi_{\mathrm{TPS}}\rangle = \prod_i P[i] \prod_{\mathrm{e}} |\mathrm{EP}\rangle_{\mathrm{e}} = \sum_{\{s_i\}} \mathrm{tTr}\left[\prod_i A[i]^{s_i}\right] |\{s_i\}\rangle \,. \tag{2.33}$$

We close this brief intermezzo on the projected entangled-pair construction of the tensor product state by first noting that if we restrict to a one-dimensional lattice, the resulting quantum states are the famous matrix-product states [11, 36].

Secondly, we note that in the state $|\phi_{\mathrm{EP}}\rangle$ it is by construction clear that correlation between degrees of freedom on the vertices only exists for nearest neighbors. This results in a boundary law for the entanglement entropy, cf. sect. 2.3, for this state. We only state this to note that the linear maps P, which we apply to $|\phi_{\mathrm{EP}}\rangle$ to obtain our tensor product state $|\psi_{\mathrm{TPS}}\rangle$ cannot increase the rank of a reduced density matrix of the state, and hence also the resulting tensor product state fulfills a boundary law.

Lastly, we highlight that this construction of the tensor product states gives an example of a remarkable fact of quantum states, namely that we can produce quite complicated, possibly long range correlated states from very simple, short range correlated states, like $|\phi_{\mathrm{EP}}\rangle$, by simply acting on these states with projecting linear maps.

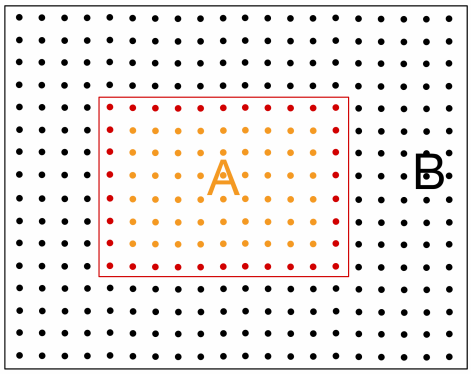

Figure 2.5.: Illustration of a lattice that is partitioned into a region A which contains all sites within the red boundary, and a region B, which contains the rest of the lattice. The sites corresponding to the boundary ∂A of A are highlighted in red. They are separated from the region B by a lattice distance of one.

2.3 Ground States as Tensor Product States

In Sec. 2.2 we have defined the tensor product states and discussed some of the basic notions associated with these states, like double-layer tensors or the projected entangled-pair picture. In this section, we are going to examine the rather pressing question, why and under which conditions the tensor product states should be useful in the study of quantum many-body systems. After all, when restricting to tensor product states, the number of independent parameters that are used in the coefficient tensor of the many-body state vector is reduced from *exponential* to *linear* in the number of constituents of the many-body system under consideration. Such a drastic reduction in descriptive freedom should be well justified. In this section, we outline the conceptual underpinnings for the use of the tensor product states in the description of ground states of gapped, local Hamiltonians in two dimensions.

To justify the use of tensor network methods, we will consider a viewpoint on correlations in quantum many-body systems that is inspired by concepts from quantum information theory [10, 37]. In this context, a central question is to ask how the entanglement between the degrees of freedom in the region of subsystem $A \subset (A \sqcup B)$ and the rest of the system B scales[4] when we increase the size of the region A, cf. Fig. 2.5.

[4]Here, the property of interest is the scaling in the asymthotic limits where both regions A and B are large.

Entanglement Entropy

Before discussing this further, we will briefly mention the relevant concepts [38]. Consider the Hilbert space of the many-body system we aim to study

$$\mathscr{H} = \mathscr{H}_A \otimes \mathscr{H}_B, \tag{2.34}$$

which we take to be made up of two subsystems A and B. We can express a completely general state vector of this Hilbert space as

$$|\psi\rangle = \sum_{i,j} C^{ij} \, |i\rangle_A \otimes |j\rangle_B \,, \tag{2.35}$$

where the set $\{|i\rangle_A\}$ is a basis of $\mathscr{H}_A$, whereas $\{|j\rangle_B\}$ is a basis of $\mathscr{H}_B$. With the goal in mind of quantifying the entanglement between the subsystems of regions A and B, we can perform a singular value decomposition of the coefficient tensor of the above state vector

$$C^{ij} = \sum_{kk'} U^i{}_k S^{kk'} V^\dagger{}_{k'}{}^j, \tag{2.36}$$

with $S^{kk'} = S_k \delta^{kk'}$ diagonal with entries S_k. This allows us to obtain a basis in which the above state vector is expressed as

$$|\psi\rangle = \sum_{k=1}^{l} S_k \, |k\rangle_A \otimes |k\rangle_B \,, \tag{2.37}$$

with $|k\rangle_A = \sum_i U^i{}_k \, |i\rangle_A$ and $|k\rangle_B = \sum_j V^\dagger{}_{k'}{}^j \, |j\rangle_B$. We notice that in this representation, the sum can be restricted to run only over the l non-zero singular values of the coefficient tensor C^{ij}. This representation is sometimes referred to as the *Schmidt decomposition*.

The procedure with which we quantify the entanglement between the two subsystems works by tracing out the degrees of freedom on one of the subsystems and considering the corresponding reduced density matrix

$$\rho_A = \mathrm{Tr}_B(|\psi\rangle \langle\psi|) = \sum_k S_k^2 \, |k\rangle_A \langle k|_A = CC^\dagger. \tag{2.38}$$

In case the state $|\psi\rangle$ contains quantum correlation between the two subsystems A and B, averaging over the states of subsystem B in this way converts these quantum correlations into statistical weight of the reduced density matrix. For pure states, the distribution of the resulting statistical weight can be used to quantify the entanglement, e.g., via the

von-Neumann entanglement entropy

$$S_{\mathrm{vN}}(\rho_A) := -\mathrm{Tr}(\rho_A \ln(\rho_A)) = -\sum_{k=1}^{l} S_k^2 \log(S_k^2). \tag{2.39}$$

With these concepts at hand, let us briefly expand on the role of the singular value decomposition (SVD), cf. Sect. 2.1.2, for the low rank approximation of quantum states. We know that the SVD decomposition allows us to construct the *optimal* low-rank approximation of a matrix via the truncation of its smallest singular values[5]. For a quantum state of a composite system made up of A and B, this optimal low rank approximation means truncation of its Schmidt values in the Schmidt decomposition in Eq. (2.37). However, we can see from Eq. (2.39), that this reduction of the rank of the coefficient tensor C^{ij} of the quantum state reduces the entanglement between subsystems A and B, as measured by the von-Neumann entanglement entropy. We infer that only quantum states that are weakly entangled between subsystems A and B, and hence only contain a few large Schmidt values in their Schmidt decomposition, can be accurately represented in a low-rank approximation.

2.3.1 Boundary Law of the Entanglement Entropy

We will now apply the concepts related to quantifying entanglement to ground states of quantum many-body systems to understand their entanglement structure.

For many purposes, the ground states of local Hamiltonians with a gap above the ground state energy in their spectrum are an interesting starting point. For such a Hamiltonian, we generically expect its ground state to fulfill the so-called *boundary law* of entanglement entropy [15, 10]. This means that the entanglement between the degrees of freedom in a connected area A and the rest of the system, as measures by the entanglement entropy, scale as the size of the boundary $|\partial A|$ [6] of the region A

$$S_{\mathrm{vN}}(\rho_A) \sim |\partial A|. \tag{2.40}$$

This is remarkable for a few reasons. First of all, it suggests that these ground states of gapped, local Hamiltonians are not as entangled as would have been possible. Secondly,

[5] How good this approximation is, is measured by the weight of the truncated singular values: $||M - M^{(k)}||_F = ||U(S - S^{(k)})V^\dagger||_F = ||(S - S^{(k)})||_F$.

[6] When speaking of the boundary $|\partial A|$ of region A, in the context of quantum lattice models, we mean those sites within A, that have a lattice distance of length one connection to a site in region B; $\partial A := \{j \in A | \exists k \in B \text{ with } \mathrm{dist}(j,k) = 1\}$. When referring to the size of this boundary $|\partial A|$ we count the number of lattice sites in ∂A.

the boundary law for the entanglement entropy that these ground states fulfill is not at all a generic property of states in the many-body Hilbert space. A generic random state from the many-body Hilbert space will instead fulfill a scaling of the entanglement entropy with the volume of region A (*volume law*)[39, 40].

In what follows, we will give a non-rigorous set of arguments that should make the boundary law for ground states of (gapped), local Hamiltonians plausible [20, 38]. For any state to minimize the energy of the local terms of the Hamiltonian, it is generically necessary to exhibit strong local quantum correlations. Conversely, for the degrees of freedom of the system that are far apart, compared to the range of interaction in the local Hamiltonian, little energetic benefit is gained from strong correlations. Further, the concept of *entanglement monogamy* [41, 42] implies that the degrees of freedom which are strongly entangled with a few other degrees of freedom in their vicinity to minimize the energy, cannot also be strongly entangled with additional degrees from which they are spatially further separated. If, in addition, the Hamiltonian under consideration is gapped, we further know from the exponential clustering of correlations [43] that the degrees of freedom can only be substantially correlated within a finite correlation length.

These quite general and heuristic arguments for gapped, local Hamiltonians suggest that the correlations between the degrees of freedom in a connected subsystem A and the rest of the system B are mainly located wherever A and B are spatially close. This is the case at the boundary ∂A of subsystem A, cf. Fig. 2.5. Thus, we expect that under these circumstances, the entanglement entropy will scale as a function of the size of the boundary. Let us note that if the local Hamiltonian is not gapped, the boundary law can be weakly violated in some cases, as we discuss in Sec. 2.3.2.

The boundary law of entanglement entropy has been proven to be a property of ground states in several situations, most notably for gapped, local Hamiltonians in one dimension with a non-degenerate ground state [44]. In two or more dimensions, such a general statement is not available. Results obtained so far require additional assumptions about the density of states in the system under consideration [45]. For more in-depth discussions on further cases of proven boundary law, see [10, 37]. While there is no rigorous proof yet[7], we still expect, for the heuristic reasons sketched above, the boundary law to be a generic feature of the ground state of gapped, local Hamiltonians even in higher dimensions.

The tensor product states, which we have introduced in Sec. 2.2, fulfill the area law of entanglement entropy by construction. This can be easily seen with the tools introduced

[7]We also note that there is no known counterexample.

above[8]. We can first write every tensor product state in the form of Eq. (2.35).

$$|\psi_{\mathrm{TPS}}\rangle = \sum_{i,j} C^{ij}_{\mathrm{TPS}} \, |i\rangle_A \otimes |j\rangle_B \,, \tag{2.41}$$

where we know, due to the structure of the tensor product state, that we can decompose the coefficient tensor as

$$C^{ij}_{\mathrm{TPS}} = \widetilde{A}^{i}{}_{v} \widetilde{B}^{vj}. \tag{2.42}$$

The matrix $\widetilde{A}^{i}{}_{v}$ is the contraction of all local tensors in region of subsystem A, while $\widetilde{B}^{vj}$ corresponds to the contraction of all local tensors in the rest of the system. After the contraction over all local tensors within one connected region, the physical indices that are open are combined into one index (i and j), while all open virtual indices from the boundary of the region are combined into the index v, such that

$$\begin{gathered} \widetilde{A} : V^{\partial A}_{\mathrm{virt}} \to V^{A}_{\mathrm{phys}}, \quad \widetilde{B} : (V^{B}_{\mathrm{phys}})^{*} \to V^{\partial A}_{\mathrm{virt}} \\ V^{\partial A}_{\mathrm{virt}} = \bigotimes_{k \in \partial A} V_{\mathrm{virt}}[k], \quad V^{A}_{\mathrm{phys}} = \bigotimes_{l \in A} V_{\mathrm{phys}}[l], \quad V^{B}_{\mathrm{phys}} = \bigotimes_{l \in B} V_{\mathrm{phys}}[l]. \end{gathered} \tag{2.43}$$

We will in the following assume that the dimensions of all local physical spaces $V_{\mathrm{phys}}[l]$ on the sites l of the lattice are identical and that the same is true for all virtual spaces $V_{\mathrm{virt}}[k]$. From the fact, that the dimension of V^{A}_{phys} grows exponentially with the volume of the region A, while the dimension of $V^{\partial A}_{\mathrm{virt}}$ grows exponentially with the boundary of the region A, we conclude that in the limit of a large region A, the rank of the matrix $\widetilde{A}^{i}{}_{v}$ is limited by the dimension of the virtual space at the boundary, $\dim(V^{\partial A}_{\mathrm{virt}}) = \dim(V_{\mathrm{virt}})^{|\partial A|}$. Hence, we can conclude from the Schmidt decomposition that there are at most $\dim(V_{\mathrm{virt}})^{|\partial A|}$ singular values of C^{ij}_{TPS}. This allows us to give an upper bound on the entanglement entropy

$$\begin{aligned} S_{\mathrm{vN}}(A) &= - \sum_{k=1}^{\dim(V_{\mathrm{virt}})^{|\partial A|}} (S^{\mathrm{TPS}}_{k})^2 \log((S^{\mathrm{TPS}}_{k})^2) \\ &\leq - \sum_{k=1}^{\dim(V_{\mathrm{virt}})^{|\partial A|}} \frac{1}{\dim(V_{\mathrm{virt}})^{|\partial A|}} \log(\frac{1}{\dim(V_{\mathrm{virt}})^{|\partial A|}}) = |\partial A| \log(\dim(V_{\mathrm{virt}})), \end{aligned} \tag{2.44}$$

which scales as the size of the boundary of the region A. Hence, the tensor product states fulfill the boundary law of entanglement entropy. Since at zero temperature, all

[8] Alternatively, it can be concluded from the construction of the tensor product states as projected entangled-pair states, as we noted in Sec. 2.2.5.

connected correlations are due to entanglement, this correct scaling of the entanglement entropy can be used to justify that the tensor product states will be a good variational ansatz to describe the ground states of local Hamiltonians[9].

2.3.2 Remarks on and beyond the Boundary Law

It is, of course, also worthwhile to ask under which conditions the ground states of local Hamiltonians do not fulfill a boundary law for the entanglement entropy. In fact, in two dimensions, the list of examples of such boundary-law-violating behaviour is quite limited. The known examples involve gapless fermion systems (free fermions or Fermi-liquids or even non-Fermi liquids [47]) with a Fermi-surface which are known to display a logarithmic violation[10] to the area law [49, 50, 51]

$$S^{\mathrm{Fermi}}(A) \sim |\partial A| \log(A). \tag{2.45}$$

Interestingly, disorder effects can "smear out" the Fermi surface and restore boundary law behaviour [52, 53]. If the analog of a Fermi surface is constructed for bosons, these can also give rise to a logarithmic violation of the boundary law [54].

The gapless systems with a Fermi surface (or its bosonic analog) are, however, not representative of all gapless systems. Indeed, for other generic kinds of gapless systems like systems with spontaneously broken global symmetries, the boundary law is expected to hold, with only subdominant corrections

$$S^{\mathrm{SSB}}(A) \sim \alpha|\partial A| + \frac{n_G}{2}\log(|\partial A|), \tag{2.46}$$

where n_G labels the number of Goldstone modes present in the system [37, 55].

Further, we can even give examples of quantum states that can be constructed explicitly as a tensor product state with diverging correlation length that fulfill the boundary law of entanglement entropy. For example, the short-range resonating valence bond state on the square lattice is known to have algebraically decaying dimer-dimer correlations, but has an exact representation as a bond-dimension three tensor product state [56, 57, 58, 59] and hence fulfills the boundary law of entanglement entropy. We introduce the

[9] We note, however, that there exist states with a boundary-law, which cannot be efficiently represented as a tensor product state [46].

[10] Swingle and Senthil have even conjectured, that in two spatial dimensions such a logarithmic violation of the area law might be the strongest form of area law violation for local systems [48].

tensor product state representation of this state in Sec. 3.2.2 and numerically investigate its correlation length in Sec. 4.3.1. We note that further examples of this kind are known [58, 60].

We close this section by mentioning, that even in situations where there are violations of the boundary law, like for gapless free fermions, the tensor product states might still be an efficient ansatz [61], in the sense that the bond dimension necessary to archive a certain precision grows only as a power law[11].

2.4 $2 \neq 1$: Tensor Product and Matrix Product States

In many ways, the tensor product states (TPS) generalize the well-established matrix product states (MPS) [15, 19] to two dimensions. The coefficient tensor of the many-body state vector for a MPS is constructed analogously to Eq. (2.20) for one dimension and is given by

$$\mathrm{tTr}\left[\prod_i A^{s_i}[i]\right] = \quad (2.47)$$

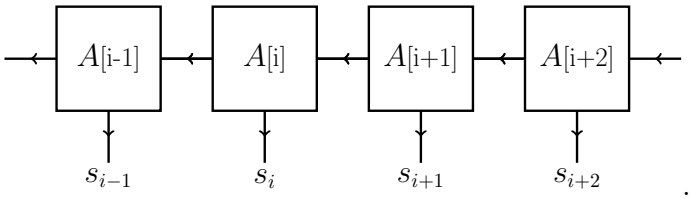

.

However, the physics of two-dimensional quantum systems can be, in many ways, different and more complex than its one-dimensional counterpart. So it might not be surprising that not all of the lessons learned for the paradigmatic one-dimensional tensor network states, the matrix product states, translate directly to their two-dimensional generalizations, the tensor product states. To highlight this fact, we will list and discuss a few prominent examples of the differences between matrix product states and tensor product states in this section.

The most computationally relevant difference between one- and two-dimensional quantum states expressed as MPS or TPS, respectively, is that for MPS, the double-layer tensor networks that appear for the calculations of norms or observables are *efficiently contractible*. Specifically, this means that the cost for the contraction of expectation values for an MPS scales as $\mathcal{O}(Nd\chi^3)$ for finite MPS or $\mathcal{O}(d\chi^3)$ in the case of translation invariant, infinite MPS [15]. Here χ is the bond dimension of the MPS while d is the

[11] While analogous statements in one dimension [62, 63] have been exploited in numerical calculations, in two dimensions this is substantially more expensive and hence this statement has (to date) to be taken as a conceptual one.

dimension of the physical Hilbert space. For TPS, the exact calculation of observables is, in general, exponentially hard as it involves the contraction of two-dimensional tensor networks. To illustrate this, consider a finite two-dimensional tensor network on a square lattice of size $L \times L$. After having contracted half of the sites in the square lattice (and assuming all of these sites are connected), the resulting contracted tensor has at least the number of open indices that it takes to perform the shortest cut to achieve an equal bipartition of the lattice. In this case, the resulting tensor would have L open legs. Hence, just storing this tensor requires memory that scales exponentially in L[12].

Going one step beyond this, a central difference between MPS and TPS is that MPS are finitely correlated[13]. Even further, the finite correlation length of a translation-invariant MPS can be exactly calculated efficiently [15]. The fact that an MPS is finitely correlated is implied if it fulfills a property called *injectivity*[14] [65]. Injectivity also implies that we can construct a gapped, local Hamiltonian (so-called *parent Hamiltonian*) of which the MPS is the unique ground state [65].

While a completely analogous notion of injectivity can be defined for TPS, it no longer implies that the TPS has a finite correlation length [66]. Indeed, even for the task of calculating the correlation length of a TPS exactly no known efficient method exists[15]. In fact, on can construct TPS that have infinite correlation length and algebraically decaying correlations [58] and can even find this behaviour in physically motivated cases as we explore for the short-range resonating valence bond state [56, 57, 58, 59], cf. Sec. 3.2.2, numerically in Sec. 4.3.1. The fact that TPS can have an infinite correlation length also complicates the question of them being ground states of gapped, local Hamiltonians. While we can, for injective TPS, still construct local parent Hamiltonians, these can be gapless [66].

Another conceptual difficulty that appears for TPS is that the question of whether the translation-invariant TPS built from two different local tensors represents the same quantum state is, in general, undecidable. This means that there cannot exist an algorithm that resolves this question in a systematic way [67]. Answering this question is

[12] We note that the complexity class of the general task of contracting TPS has been studied and found to be computationally hard [64].

[13] MPS are generically finitely correlated [65], meaning they have a finite correlation length ξ. At most, they are a superposition of a finite number of finitely correlated states.

[14] We call an MPS injective if there exists a finite number L, such that after contracting L adjacent local tensors of the MPS, the resulting tensor can be seen as an injective map from the virtual to the physical space.

[15] We can, however, extract it numerically in an approximate fashion, as we discuss in Sec. 4.3.1.

only possible for certain subsets of the TPS [19, 68, 69]. For MPS, on the other hand, this question is settled in full generality by the *fundamental theorem of MPS* [19].

A physical phenomenon that is excluded in one-dimensional quantum systems is that of *intrinsic topological order*. To qualitatively understand this, consider that we can generically use a MPS to represent the ground state of a gapped, local Hamiltonian. When using a MPS to represent a quantum state, however, its short-range entangled nature makes the representation of intrinsic topological order impossible [20, 70, 71].

However, in two dimensions, this behaviour is possible, with the canonical example being the toric code model [72]. It turns out that the ground state of this paradigmatic model can be constructed exactly as a TPS. Moreover, not only can TPS exactly represent the ground state of the toric code tensor, but one can even link the global phenomena of topological order to *virtual* symmetries of the local tensors of the TPS. We will discuss this in Sec. 3.2.3

CHAPTER 3

Tensor Product States: Structure and Examples

Tensor product states are a very versatile tool for the study of ground states of local many-body Hamiltonians. This is because these states are well-suited for numerical studies with the use of modern computing machinery, as we discuss in Chap. 4. At the same time, since they are built up from simple local tensors, tensor product states allow for structural insights into many-body states, as well as for the construction of illustrative examples.

In this chapter, we first briefly introduce the incorporation of symmetries in tensor networks and the impact on the structure of the local tensor in Sec. 3.1. Afterwards, we move to the construction of several illustrative examples of tensor network states in Sec. 3.2. Among these, we specifically treat the short-range resonating valence bond states and the toric code states, which we already mentioned in the previous chapter and which will serve as example states for numerical procedures in Chap. 4.

3.1 Symmetries in Tensor Networks

In situations where a global symmetry is present, it can be useful to consider state vectors or general tensor networks that are invariant under the action of a certain symmetry group $\mathcal{G}$ [16, 73, 74, 75, 76]. In a quantum system, in such a case, the Hamiltonian commutes with the corresponding symmetry operator. This means we can simultaneously diagonalize these operators and hence label the eigenstates of the Hamiltonian with the eigenvalues of the symmetry operator.

It is possible to guarantee that a state vector (or a general tensor network) is invariant under the symmetry of the group $\mathcal{G}$ by choosing the tensors from which the network is built to be invariant under the same symmetry action [74]. As an example, we can enforce that the local tensors of a tensor product state are invariant under the application of

unitary representations U_g, W_g of every element $g \in \mathcal{G}$

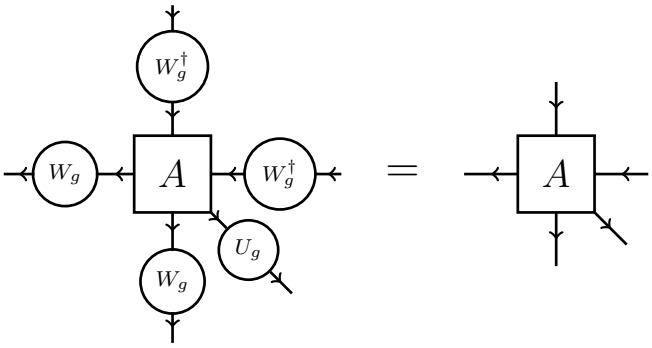

(3.1)

where the dual spaces transform contragredient to the vector spaces. The state vector $|\psi_{\text{TPS}}\rangle$ resulting from the contraction of the virtual indices is then guaranteed to be invariant under the global, on-site action of the symmetry group $\mathcal{G}$, as the action on the virtual indices cancels out

$$\otimes_i U_g[i] \, |\psi_{\text{TPS}}\rangle = |\psi_{\text{TPS}}\rangle \, . \tag{3.2}$$

Here i indexes the sites of the lattice. Beyond the guarantee of a certain symmetry of the tensor network, the enforcement of a symmetry on the level of a local tensor can also be exploited computationally. This is because the physical and virtual spaces V can be decomposed into a direct sum of irreducible representations V^a of the group $\mathcal{G}$

$$V \cong \bigoplus_a d_a V^a. \tag{3.3}$$

We label the number of times the irreducible V^a appears in the decomposition as d_a. In the familiar case of a matrix, such a decomposition results in a block structure, in which only states from identical sectors of the irreducible representations can couple to each other, while all other matrix elements are zero. For higher rank tensors, such a decomposition of the spaces of the local tensor also results in an internal block structure of the tensors, allowing us to store and manipulate only a reduced number of parameters [74]. This sparse tensor structure can hence result in more efficient computations.

We note that we make use of these techniques in Chap. 10 when describing a $U(1)$-symmetric partition function as a tensor network.

3.2 Examples of Tensor Product States

We will now present a few concrete examples of tensor product states, highlighting some of the remarkable properties these states can exhibit. These examples further allow us

to emphasize the general strategies used in constructing specific tensor product states.

3.2.1 Simplest Examples

The simplest example of quantum states that can be explicitly expressed as tensor product states are trivial product states $|\psi\rangle = \bigotimes_i |\phi_i\rangle$, where i labels the local Hilbert spaces from which the many-body Hilbert space is built. Product states are tensor product states of bond dimension one, such that the local tensors just encode the coefficients of the local, single-particle state, and the multiplication of the local tensors becomes just a simple multiplication of numbers.

Going one step beyond the trivial product states, we can construct the Greenberger–Horne–Zeilinger (GHZ) state

$$|\psi_{\mathrm{GHZ}}\rangle = \frac{1}{\sqrt{2}}\big(\otimes_i |0_i\rangle + \otimes_i |1_i\rangle\big) \tag{3.4}$$

in the tensor product state language [20]. As the canonical example in two dimensions, let us consider such a state on the infinite square lattice, in which case we can use a single translational invariant local tensor of the form

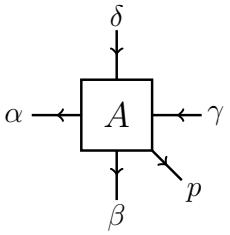

$$= \begin{cases} 1 & \text{if } p = \alpha = \beta = \gamma = \delta \\ 0 & \text{otherwise} \end{cases}, \tag{3.5}$$

where p labels the basis of the local Hilbert space $\{|0\rangle, |1\rangle\}$ and the Greek indices label an identical basis for the virtual spaces. The resulting tensor product state thus has bond dimension $\chi_B = 2$. Let us note that we ignore the normalization of the state here, which needs to be taken into account for the calculation of observables, cf. Sec. 2.2.4. The reason this local tensor results in the GHZ-state upon contraction of all virtual indices is that its only non-zero entries are for identical values of virtual and physical indices. Hence, the only way to obtain a non-vanishing many-body coefficient, cf. Eq. (2.20), is to choose the local, physical configurations to be either all $|0\rangle$ or all $|1\rangle$, such that the contraction contains a contribution, where only non-vanishing elements of the local tensors are multiplied.

3.2.2 Resonating Valence-Bond States

A more intricate construction of a prominent quantum state as a tensor product state is the short-range resonating valence bond (RVB) state [56, 57]. We already mentioned in the previous chapter that this state on the square lattice is an example of a tensor product state that hosts algebraically decaying quantum-dimer correlations [59]. The RVB state was originally proposed as a ground state candidate for the Heisenberg model on the triangular lattice [56]. Although it has since been shown that the ground state for this model is a state with 120°-order [77, 78], the RVB states remain of interest as examples of spin-liquid states [79].

The construction of the RVB state as a tensor product state works by translating the local properties of the state into the structure of the local tensors. The RVB state is defined by an equal-weight superposition of all possible dimer coverings of the lattice

$|\psi_{\mathrm{RVB}}\rangle =$ 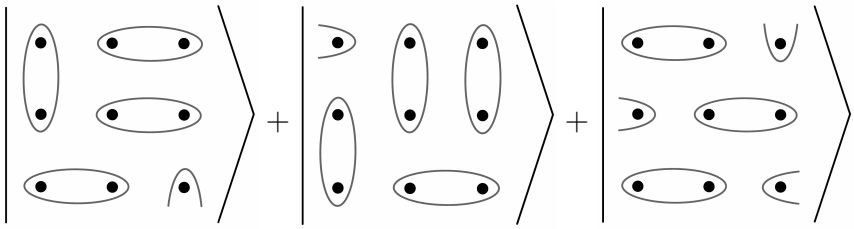 $+ \ldots$ (3.6)

where the dimers are singlets for two neighboring spin-$\frac{1}{2}$ degrees of freedom. In the above illustration, we show these singlets as encircled sites of the lattice.

The construction as a tensor product state[1] is easiest in the framework of the projected entangled-pair picture of the tensor product states, which we discussed in Sect. 2.2.5. In the projected entangled-pair construction of the short-range RVB state [58], the starting point is again a product state of entangled pairs, specifically, we cover the bonds of the lattice, cf. Fig. 2.4a, with states of the form

$$|\mathrm{EP}_{\mathrm{RVB}}\rangle = |{\uparrow\downarrow}\rangle - |{\downarrow\uparrow}\rangle + |00\rangle\,. \tag{3.7}$$

We thus will end up with a bond dimension three tensor product state as the virtual spaces are spanned by $\{|{\uparrow}\rangle, |{\downarrow}\rangle, |0\rangle\}$. Given the covering of the lattice with the virtual state in this way, we proceed by acting on the virtual degrees of freedom on every lattice site with a projector, cf. Eq. (2.33), to create the RVB state. It is within this projector that we encode the local structure of the RVB state. Concretely, the relevant local structure is that for every dimer covering of the lattice, every physical spin is part of

[1] Note that we again ignore the normalization of the state here.

exactly one singlet. We can thus define the projectors by giving their non-zero entries

$$P^{s}{}_{000s} = P^{s}{}_{00s0} = P^{s}{}_{0s00} = P^{s}{}_{s000} = 1 \quad \text{for} \quad s \in \{\uparrow, \downarrow\}, \tag{3.8}$$

and recall that the superscript index corresponds to the physical Hilbert space, whereas the subscript indices correspond to the virtual indices. These projectors have a simple interpretation. They assign a non-zero contribution only in case exactly one of the four virtual spins on a given lattice site is in a state $|\uparrow\rangle$ or $|\downarrow\rangle$, which is then translated one-to-one to the local physical degree of freedom. At the same time, the remaining three virtual degrees of freedom have to be in state $|0\rangle$. Together with the virtual states on each bond given in Eq. (3.7), this is exactly the local rule which, if enforced on every site, results in the RVB state.

To illustrate why this works, it is useful to imagine two neighboring sites i and j on the lattice and the possible configurations that result upon the application of these projectors. The entangled-pair state $|\mathrm{EP}^{ij}_{\mathrm{RVB}}\rangle$, which is defined on the edge connecting the two lattice sites we are considering, is a superposition of two parts. One which is a singlet and one which is $|00\rangle$. The above projectors will take the singlet contribution and translate it one-to-one to the two physical sites, while simultaneously only allowing for configurations of $|00\rangle$ on all other entangled pairs that connect sites i and j to the rest of the lattice sites. At the same time, the projectors will take the contribution $|00\rangle$ to the virtual entangled-pair between our two lattice sites i and j, and project such that exactly one of the remaining entangled pairs for each of the two lattice sites that connects to the rest of the lattice is part of a singlet. Thus, we end up with a physical state in which for every resulting configuration, every physical spin is part of one singlet. As we gave all non-zero elements in the projectors the same value, we end up with an equal-weight superposition of these dimer coverings as we desired.

In the case of the RVB state, the representation as a tensor product state has some practical advantages. For example, the usual expression of the state as an equal-weight superposition of all singlet coverings has the downside that the singlet coverings are an over-complete basis and are not orthogonal. This can make practical calculations more difficult, whereas, e.g., the identification that the short-range RVB state hosts algebraically decaying correlation functions can be easily done in the numerical tensor product state framework as we demonstrate in Sect. 4.3.1. Furthermore, once we have expressed a state as a tensor product state, we can also use this to construct parent Hamiltonians, which host these states as ground states [80, 81][2].

[2]We note that the parent Hamiltonians can be complicated and involve many-spin interaction terms.

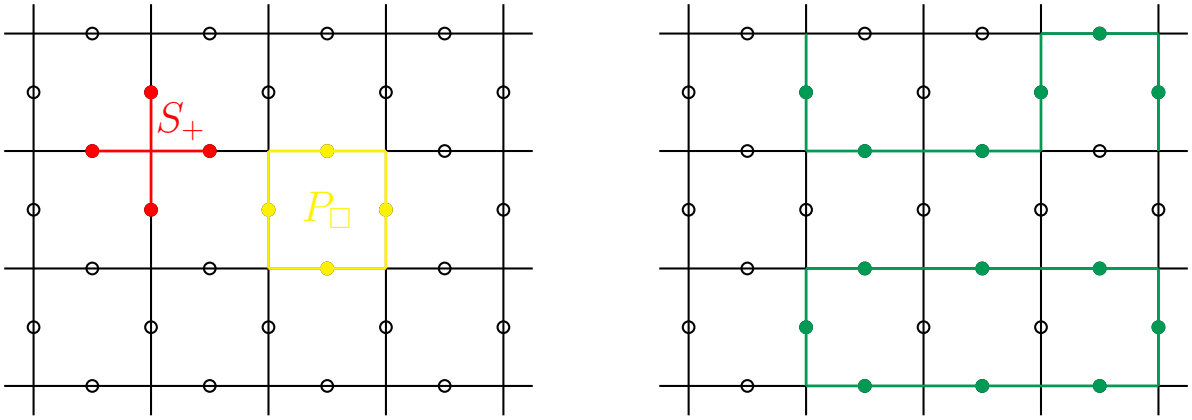

Figure 3.1.: (a) Illustration of the star and plaquette operators of the toric code Hamiltonian and their support. (b) Illustration of a product state with closed loops and open "strings". Here, the filled circles represent a $|1\rangle$ configuration of the local spin, while an empty circle represents a $|0\rangle$ configuration. We find that configurations with open strings of $|1\rangle$ are not ground states of the star operators on the ends of the strings.

3.2.3 Toric Code Ground State

An intrinsically topologically ordered state that can be easily constructed as a finite-bond-dimension tensor product state is the ground state of the toric code Hamiltonian [20, 72, 58, 82]. This Hamiltonian is conventionally defined on a square lattice with the local spin-$\frac{1}{2}$ degrees of freedom on the edges of the lattice. The terms of the Hamiltonian

$$H_{\mathrm{TC}} = -\sum_{\{+\}} S_+ - \sum_{\{\square\}} P_\square. \tag{3.9}$$

consist of two kinds of operators[3]. The first kinds are the so called *star operators* $S_+ = \sigma^z_{1+}\sigma^z_{2+}\sigma^z_{3+}\sigma^z_{4+}$ which act on the four local spin-$\frac{1}{2}$ Hilbert spaces surrounding a vertex of the square lattice. Further, we have the *plaquette operators* $P_\square = \sigma^x_{1\square}\sigma^x_{2\square}\sigma^x_{3\square}\sigma^x_{4\square}$ that act on the local Hilbert spaces which are located on the edges surrounding a plaquette of the square lattice. We illustrate this in Fig. 3.1a.

We find that all terms in the Hamiltonian commute with each other, which allows us to construct a ground state explicitly [72]. This ground state can be written as the

[3]The sums in this notation run over all vertices and plaquettes of the square lattice.

equal-weight superposition of "closed-loop" product states $|C_i\rangle$

$$|\psi_{\mathrm{TC}}\rangle = \sum_i |C_i\rangle\,. \tag{3.10}$$

A "closed-loop" product state is a product state in z-basis, in which all local, physical spin-configurations $|1\rangle$ are on edges that form closed loops. Such a closed loop is illustrated in Fig. 3.1b, and a more detailed explanation of the construction of this ground state can be found in App. A.

Tensor Product Representation of the Ground State

The "closed-loop" property of the ground state of the toric code Hamiltonian defines a strict, *local* rule for the ground state. While the "closed-loop" property itself is not a local property, it is however equivalent to having an even number of adjacent edges with a configuration $|1\rangle$ at every local vertex of the square lattice, or alternatively, no strings of $|1\rangle$ ending at any vertex.

Such a local rule can oftentimes be used to explicitly construct quantum states as tensor product states by encoding these local rules into the local tensors.

We will now define a set of tensors [82] that encode these local rules, such that upon contraction of the corresponding tensor network, we obtain a finite coefficient of the many-body state vector only for configurations that follow the local rules. We start by defining a rank-three tensor, which we shall associate with every edge and hence with every physical degree of freedom of the square lattice

$$E^{p}{}_{\alpha\beta} = \quad \alpha \rightarrow \bullet \leftarrow \beta \quad (p \downarrow) \quad = \begin{cases} 1 & \text{if } \alpha = \beta = p \\ 0 & \text{otherwise} \end{cases}. \tag{3.11}$$

Here the label $p \in \{0, 1\}$ indexes the basis of the local spin-$\frac{1}{2}$ Hilbert space on the edge, while the indices $\alpha \in \{0, 1\}$ and $\beta \in \{0, 1\}$ label the basis of the virtual Hilbert spaces, which we choose here to be two-dimensional as well. This tensor corresponds to the picture of the presence (local configuration $|1\rangle$) or absence (local configuration $|0\rangle$) of a string on an edge. The information about the configuration of the local spin on this edge is transported via a one-to-one correspondence to the virtual indices. The only non-zero entries of this edge tensor correspond to index configurations where physical and virtual indices take the same value.

To enforce the local rule that no string can end in a vertex in the ground state, we

can define a rank-four tensor associated with every vertex

$$V^{\alpha\beta\gamma\delta} = \quad = \begin{cases} 1 & \text{if } (\alpha+\beta+\gamma+\delta)_{\text{mod } 2} = 0 \\ 0 & \text{otherwise} \end{cases}, \tag{3.12}$$

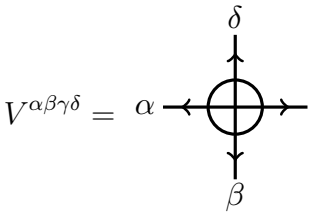

where the indices $\alpha, \beta, \gamma, \delta$ label the basis states of the virtual spaces this operator acts on. As it is only non-zero for configurations of the virtual indices that correspond to an even number of strings on the adjacent edges, this tensor enforces the local rule of the toric code ground state. A tensor trace over all virtual indices of these tensors yields the coefficients for the toric code ground state, because after contraction of the network, only configurations of the physical spins that fulfill the ground state rules are non-zero, and all have the same amplitude

$$|\psi_{\text{TC}}\rangle = \sum_{\{s\}} \text{tTr}\big(\prod_i \prod_j V[i] * E^{s_j}[j]\big)\, |\{s\}\rangle\,. \tag{3.13}$$

Here, the index i runs over all vertices of the lattice, while j indexes all edges, and the contracted virtual indices of the tensors are suppressed.

This construction illustrates that tensor product states can represent topologically ordered states [58, 82]. However, as they are built from easy-to-examine local components, tensor product states allow for insight into the role of symmetry in topologically ordered states as well as the stability of topological order, which we will discuss in the following.

We briefly note that the structure of this tensor network is slightly different from the structure of the generic tensor product state construction presented in Sec. 2.2. However, the tensor network discussed above can be easily rearranged exactly into the generic form of a tensor product state [83].

Virtual Symmetry and Topological Order of the Toric-Code Tensor Network

The tensors defined above, from which we can build the toric code ground state, are invariant under the application of σ^z operators to all their virtual links

simultaneously [20, 84]

$$\begin{aligned} \mathrm{Z}_{\mathrm{virt}}(E) := (\sigma^z \otimes \sigma^z)(E) = E, \\ (\sigma^z)^{\delta}_{\beta}(\sigma^z)^{\gamma}_{\alpha} E^{p}{}_{\gamma\delta} = E^{p}{}_{\alpha\beta} \end{aligned} \tag{3.14}$$

and

$$\begin{aligned} \mathrm{Z}_{\mathrm{virt}}(V) :=& (\sigma^z \otimes \sigma^z \otimes \sigma^z \otimes \sigma^z)(V) = V, \\ (\sigma^z)^{\alpha}_{\alpha'}(\sigma^z)^{\beta}_{\beta'}(\sigma^z)^{\gamma}_{\gamma'}(\sigma^z)^{\delta}_{\delta'} V^{\alpha'\beta'\gamma'\delta'} =& \begin{cases} (-1)^{(\alpha+\beta+\gamma+\delta)_{\mathrm{mod}\ 2}} = 1 & \text{if } (\alpha+\beta+\gamma+\delta)_{\mathrm{mod}\ 2} = 0 \\ 0 & \text{otherwise.} \end{cases} \end{aligned} \tag{3.15}$$

The action of the of the σ^z operators on the two-dimensional virtual spaces is the familiar $\sigma^z |0\rangle = |0\rangle\,, \quad \sigma^z |1\rangle = -|1\rangle$. As this action on the virtual legs of the toric-code tensors squares to the identity, we say that they possess a *virtual* $\mathbb{Z}_2$-symmetry. This virtual symmetry is intimately related to the topological order [19, 20, 84, 85] of the ground state of the toric code Hamiltonian, as we show in the following. As a first step in this direction, we note that, as we can transform every individual tensor in the ground state tensor network — leaving the state invariant — we may also transform all tensors that lie within a certain area, cf. Fig. 3.2a. As $(\sigma^z)^2 = \mathbb{1}$, all σ^z operators that lie within our transformed area A are canceled and the only operators that remain are those on the boundary of A, cf. Fig. 3.2b. Hence, we know that the state is invariant under the application of σ^z on the virtual boundary of any connected area. Note that this is less obvious than the virtual $\mathbb{Z}_2$-symmetry of the individual tensors shown above. This is because in this case, the individual tensors at the boundary of region A do change under the application of the σ^z-operators on the boundary of an area, but the state we obtain upon contraction does not.

Upon application of σ^z onto the virtual boundary of our designated connected region A, we pull the σ^z operators onto the edge tensors they act on. We notice that due to the definition of the edge tensors E, we can pull this operator to the *physical* space [20, 84]

$$(\sigma^z)^{\alpha'}_{\alpha} E^{p}{}_{\alpha'\beta} = (\sigma^z)^{p}_{q} E^{q}_{\alpha\beta}. \tag{3.16}$$

Hence, we find that our toric-code ground state $|\psi_{\mathrm{TC}}\rangle$ is also invariant under the appli-

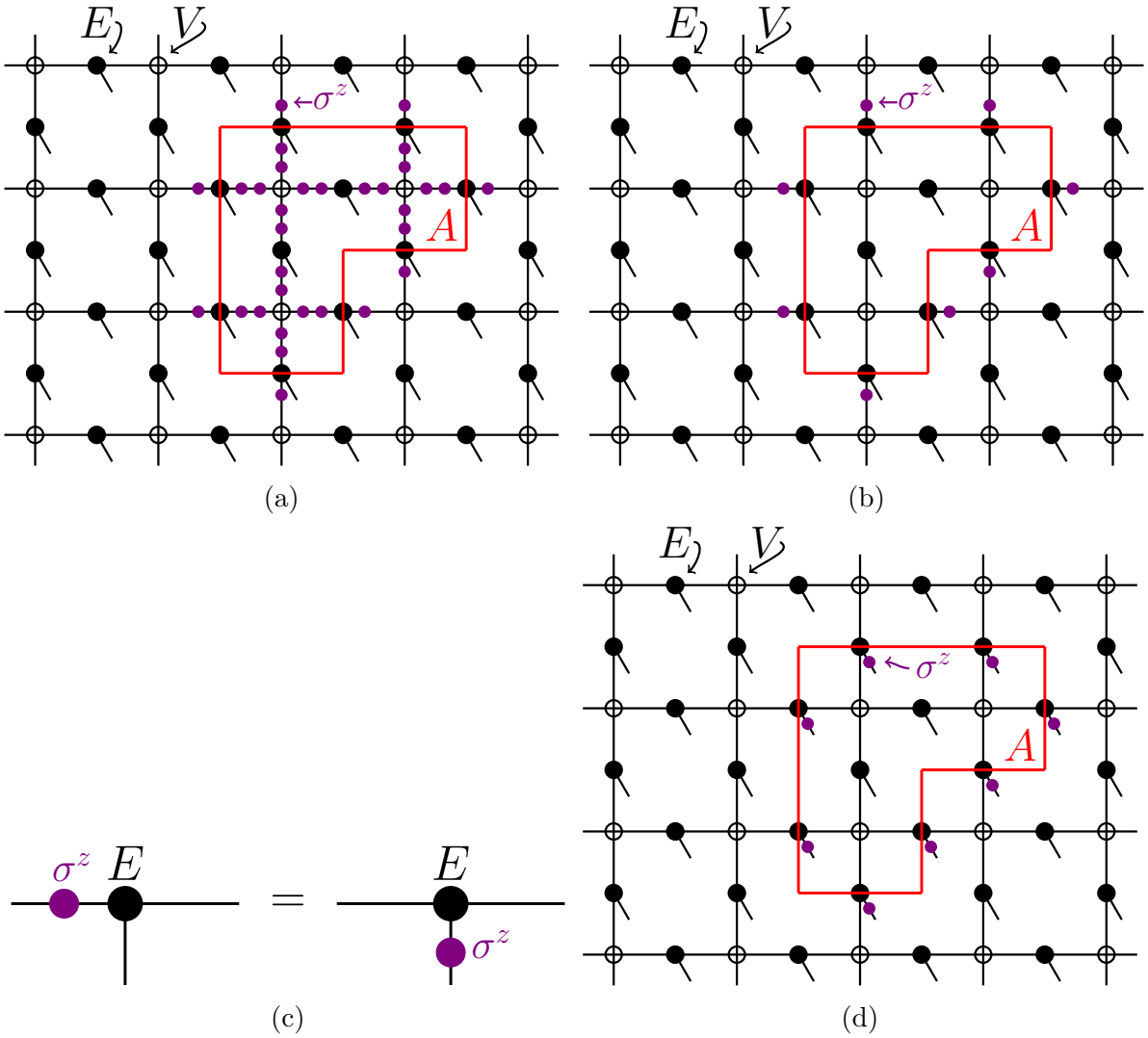

Figure 3.2.: Illustration of the toric code ground state as a tensor product representation. We do not show the arrows on the legs of tensors for better visibility. The filled circles correspond to the edge tensors E, the non-filled circles correspond to the vertex tensors V, while the pink tensors (matrices) represent the σ^z matrices.(a) Virtual symmetries of the tensors are applied to all tensors in the area A. (b) Since the applied matrices square to the identity, we can remove them from the inner indices of area A while a single instance remains on the boundary. (c) Illustration of the property of the edge tensor E, which allows us to pull a σ^z matrix from the virtual to the physical leg. (d) Illustration that, as we can pull the σ^z matrices to the physical index of the edge tensors, we have a relation between the virtual symmetry of the local tensors and the invariance under application of Wegner-Wilson loops.

cation of closed loops of σ^z operators on the physical legs of the tensors

$$\begin{aligned}\mathrm{tTr}\big(\prod_{i,j} V[i] * E^{s_j}[j]\big) &= \mathrm{tTr}\Big(\Big[\prod_{i\in A, j\in A} \mathrm{Z}_{\mathrm{virt}}(V[i]) * \mathrm{Z}_{\mathrm{virt}}(E^{s_j}[j])\Big] \prod_{k\notin A, l\notin A} V[k] * E^{s_l}[l]\Big) \\ &= \mathrm{tTr}\big(\big[\prod_{k\in\partial A} (\sigma^z)^{s_l}_{s_k} E^{s_k}[k]\big] \prod_{i,j\notin\partial A} V[i] * E^{s_j}[j]\big).\end{aligned} \tag{3.17}$$

This is illustrated in Fig. 3.2d. These are examples of Wegner-Wilson loops

$$W_{\mathrm{loop}} = \prod_{i\in\mathrm{loop}} \sigma^z_i. \tag{3.18}$$

These Wegner-Wilson loops are related to one of the hallmarks of topological order, the *topological ground state degeneracy*, meaning the degeneracy of multiple ground states depending on the topology of the manifold on which we define our Hamiltonian.

Take, for example, the Hamiltonian of Eq. (3.9) defined on a torus. It is useful to consider again the construction of the ground state of the toric code, by making sure it is an eigenstate of each mutually commuting, independent operator, namely the plaquette and star operators, cf. App. A. On a plane, these operators supply a number of eigenvalues equal to the dimensionality of the many-body Hilbert space. However, this is no longer true if we consider the system on a torus [72], as on the torus we have two additional relations

$$\begin{aligned}\mathbb{1} &= \prod_{\{\square\}} P_\square \\ \mathbb{1} &= \prod_{\{+\}} S_+,\end{aligned} \tag{3.19}$$

where the product runs over all plaquettes and vertices respectively, and implies that one of the plaquette- and one of the star-operators is no longer independent. Hence, the number of eigenvalues we obtain from star- and plaquette-operators to label the states of the many-body Hilbert space is reduced to $2^{N_e-2} = 2^{N_e}/4$, where N_e refers to the number of edges on our lattice. The dimensionality of our many-body Hilbert space on the torus is, however, still 2^{N_e}. Given the fact that the eigenvalues we are using for labeling are the eigenvalues of mutually commuting terms of the Hamiltonian, we find that the energy spectrum of the Hamiltonian is four-fold degenerate. This includes the ground states.

A set of operators that can be used to give additional quantum numbers to label these degenerate states are the Wegner-Wilson loops we found above[4]. Namely, those which correspond to loops that wind around the non-trivial cycles of the torus. While these operators still commute with the Hamiltonian, they do not correspond to a virtual $\mathbb{Z}_2$-symmetry of our tensor network construction, as they do not define a loop that encloses a well-defined area; hence, their application can change the state.

Let us stress once more, that within the tensor network representation of the ground state of the toric code, we can relate the phenomenology of topological order — specifically the ground state degeneracy — to a property of the *local* tensors of our network, namely their *virtual* symmetry.

To further highlight the importance of this virtual symmetry for the topological order, let us note that the stability of the topological order of our state is destroyed if we slightly break the virtual symmetry [86]. However, the virtual symmetry of the tensor product state by itself is not enough to guarantee that the state is topologically ordered. For that, an additional requirement referred to as $\mathcal{G}$-injectivity is necessary [85]. Nevertheless, it can be useful for numerical simulations targeting topologically ordered states to enforce a virtual symmetry on the local tensor of the tensor product state ansatz, in complete analogy to what we discussed in Sec. 3.1. By just choosing the physical space to be constructed from only degenerate, trivial irreducible representations on which we act only with the identity, Eq. 3.1 enforces a virtual symmetry.

We close this section by noting that the creation of the ground state of the toric code Hamiltonian in this section is an example of a more general type of construction. The conceptual framework for using local rules that lead to global topological order, when constructing the local tensors of the tensor product state, can be generalized to all non-chiral topological orders [85, 82, 87, 88].

3.2.4 Chiral Topological Ordered States

A class of states, for which the treatment using the tensor product state is more intricate, are chiral topological states exemplified by band insulators with a non-trivial Chern number [89]. It took roughly ten years after the tensor product states had been proposed for the first examples of these states to be constructed. This was done independently by Wahl et al. [90] and Dubail and Read [91]. In these works, it was shown that

[4] W_{loop} is built from σ^z operators, so it trivially commutes with the star operators. We defined W_{loop} on closed loops, which implies that the support of W_{loop} and any of the plaquette operators of the toric code share either zero or two sites, which means they commute.

by using Gaussian fermionic tensor product states [92], one can in fact construct such chiral topological states for *free fermions* as tensor product states. However, it was simultaneously pointed out that these tensor product states cannot be ground states of gapped, local Hamiltonians.

To understand this in qualitative terms, let us highlight an argument from the paper by Wahl et al. [90]: Let us assume we had found such a free fermion tensor product state. This should allow us to construct a local, frustration-free parent Hamiltonian for which the tensor product state in question is a ground state [66]. Concretely, this means that all terms h_i in the parent Hamiltonian $H = \sum_i h_i$ have to annihilate our tensor product state. Since the terms in the Hamiltonian are local, and we want a gapped, free fermion Hamiltonian, the terms must be of the form $h_i = b_i^\dagger b_i$, with b_i being a quasi-particle operator acting on a local region. This means, however, that the corresponding Wannier functions are localized, which is in conflict with the presence of a non-zero Chern number [93, 94].

This, however, leaves open a plethora of questions of both analytic and numerical nature. For example, how generalizable are these results for interacting fermions or bosons? This is of critical importance for the use of tensor product states for the study of strongly correlated systems like fractional Hall states. Here, numerical insight is even more important, e.g., in the quantitative understanding of realistic scenarios for their realization in larger, next-generation cold atom experiments [95, 96]. However, this directly leads to an additional practical question for numerical approaches using tensor product states. If we are using a tensor product state ansatz to investigate a local Hamiltonian, for which a ground state candidate could be a chiral topological state with gapped excitations, can we hope to obtain useful results?

These questions have been approached for quasi-parent Hamiltonians recently [97], as well as in our publication [P1], where we study this for the more experimentally relevant bosonic Harper-Hofstadter model. In fact it is demonstrated and discussed that tensor product states can yield useful insights in these scenarios, while also having to deal with subtle, unphysical features in the correlation functions.

CHAPTER 4

Computational techniques for Tensor Product States

The internal structure of the tensor product states is the key to the numerical techniques for practical calculations using these states. In this chapter, we will introduce some of these methods used in numerical computations and derive some of the critical formulas of the tensor product state framework. Specifically, we first discuss the numerical techniques for the contraction of the two-dimensional tensor networks in Sec. 4.1. Building on this, we describe and discuss the approaches to find the optimal ground state approximation within the tensor product state ansatz class in Sec. 4.2. Lastly, in Sec. 4.3 we discuss the techniques for tensor product states that go beyond local observables and discuss correlation functions and entanglement spectra. We mainly focus on techniques for infinite tensor product states in this section and refer to the publication [P5] for some additional explicit discussion of these states on finite lattices.

4.1 Contraction

As we discussed in Sec. 2.2.4, calculations of observables for tensor product states require the contractions of two-dimensional tensor networks. For tensor networks with one-dimensional structure, as they appear in the context of matrix product states, we can reduce their contraction to a succession of matrix multiplications that can be performed efficiently. Due to this lack of one-dimensional structure, contractions of the two-dimensional tensor networks associated with tensor product states are much harder, as already explored in Sec. 2.4. For a tensor product state on a finite lattice, this means, e.g., that such contractions require storing tensors with exponentially many entries in the linear system size. Furthermore, for infinite translation-invariant tensor product states, an exact contraction is thus generically impossible. Due to the difficulty of the contraction, we will, for numerical calculations, make use of the approximation schemes

for the contractions. For contractions in the context of tensor product states on finite lattices with open boundary conditions, the boundary-matrix product state method is commonly used [12, 98]. We introduce this method, as well as related methods for finite lattices, in the publication [P5]. In the context of infinite tensor product states, the approximate contraction of the associated two-dimensional tensor networks is usually performed by either of two general approaches. The first set of approaches can be called scale-transformation methods, which perform coarse-graining procedures on the two-dimensional tensor network like the tensor network renormalization group (TRG) [99, 100, 101, 102] or tensor network renormalization (TNR) [103]. In contrast, the second set of approaches is a family of effective-environment methods, such as a version of the variational uniform matrix product state (VUMPS) algorithm [104, 105] or the corner transfer matrix renormalization group (CTMRG) [106, 107, 108, 109, 110, 111, 112]. The CTMRG algorithm will be introduced in Sec. 4.1.1. A reformulation of the CTMRG algorithm that has a more favorable computational scaling has been the subject of the publication [P4].

4.1.1 Corner Transfer Matrix Renormalization Group

In this thesis, the corner transfer matrix renormalization group (CTMRG) algorithm is the central tool for numerical calculations using infinite tensor product states. While the primary use of this algorithm is the computation of local observables and, by extension, energies of local Hamiltonians, the effective tensors generated for this task are used frequently in calculations of other quantities, such as correlation lengths and entanglement spectra, cf. Sec. 4.3.1 and Sec. 4.3.2. In addition, the CTMRG algorithm allows for the efficient calculation of energy gradients by leveraging its convergence to a fixed point, as we discuss in Sec. 4.2.3. This is critical for the ground state search using infinite tensor product states. In this section, we will describe the CTMRG algorithm as applicable to a single-site unit cell tensor product state ansatz. Applications of the algorithm to larger unit cell ansatzes [109] are straightforward and are discussed, e.g., in [P6].

The idea behind the CTMRG [106, 107, 108] is the use of effective environment tensors that describe the impact of certain parts of the surroundings of a lattice site on the observables (or, equivalently, the reduced density matrix) on that particular site. As is illustrated in Fig. 4.1, we define two essential types of effective environment tensors. The T-tensors describe half-infinite rows and columns of the square lattice of double-layer tensors, cf. Sec. 2.2.4, while the C-tensors describe quadrants of the infinite lattice. These effective environment tensors are defined with a particular bond dimension, re-

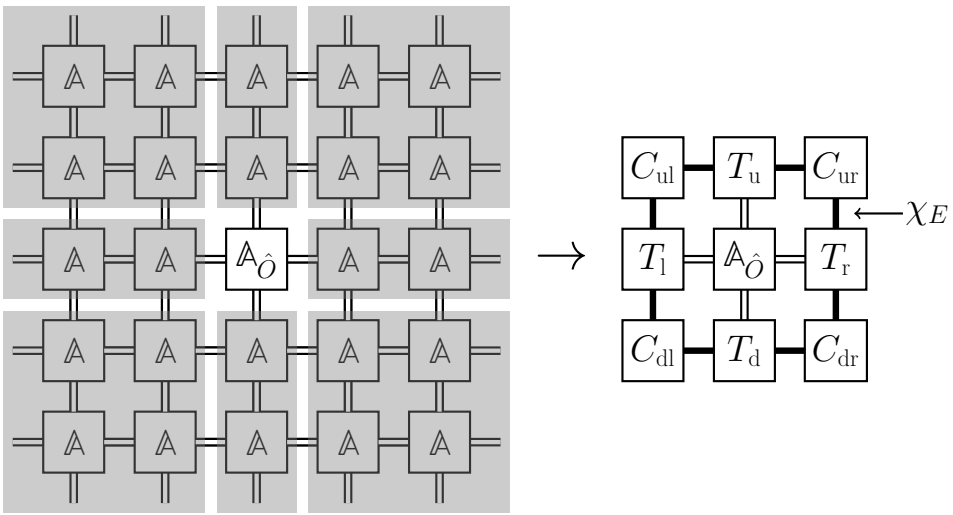

Figure 4.1.: Illustration of the concept of the CTMRG effective environment tensors. For the double-layer tensor network associated with an expectation value of a local observable on the central site, we approximate the network environment of that site using effective environment tensors. The bold lines highlight the virtual indices with bond dimension χ_E.

ferred to as the *environment-bond dimension* χ_E. This is the dimension of the virtual indices, with which the effective environment tensors connect to each other and should be seen as a refinement parameter in numerical calculations. We label the set of all the environment tensors for the local tensor A of the tensor product state as

$$e(A) = \{C_{\mathrm{ul}}, C_{\mathrm{ur}}, C_{\mathrm{dl}}, C_{\mathrm{dr}}, T_{\mathrm{l}}, T_{\mathrm{d}}, T_{\mathrm{r}}, T_{\mathrm{u}}\}, \tag{4.1}$$

where all of the environment tensors depend on A as well. With these tensors, we can then express the expectation value of a local observable as

$$\frac{\langle\psi_{\mathrm{TPS}}|\hat{O}_i|\psi_{\mathrm{TPS}}\rangle}{\langle\psi_{\mathrm{TPS}}|\psi_{\mathrm{TPS}}\rangle} \approx$$

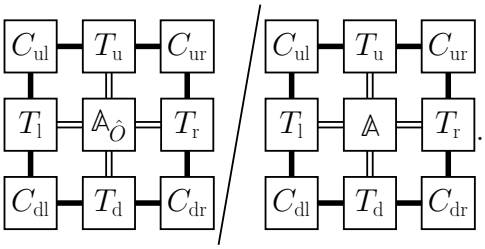

$$\Big/$$

. (4.2)

Observables with support on multiple sites can be computed completely analogously with the use of more effective environment tensors surrounding the support[1].

[1]Note, that for this case the normalization of the state vector used in Eq. (4.2) has to be adjusted to use the same effective environment tensors to cancel out their individual normalizations.

Conceptually, the accurate approximation of local observables using the effective environment tensors at a finite environment bond dimension χ_E, assumes a physical situation in which the reduced density matrix of a local site i only depends on the degrees of freedom in the vicinity of that site i. This is the case for tensor product states of small correlation length. Hence, a representation of the reduced density matrix using small bond dimension environment tensors yields a good approximation. As the correlation length of the state increases, however, so does the environment bond dimension required for an accurate approximation. In the extreme case, for tensor product states with infinite correlation length and algebraically decaying connected correlation functions, the approximation using finite environment bond dimensions actually yields an artificial finite correlation length. In these situations, a scaling analysis will be necessary, cf. Sect. 4.3.1.

The CTMRG algorithm [108, 110, 111] is used to numerically generate the effective environment tensors for a given tensor product state[2]. The algorithm works by iteratively updating the effective environment tensors by absorbing parts of the infinite tensor network into them until convergence is reached. A single CTMRG iteration step c is described by the function

$$c(A, e_i(A)) = e_{i+1}(A), \tag{4.3}$$

and the fixed point condition describes the situation in which the algorithm converges

$$c(A, e^*(A)) = e^*(A). \tag{4.4}$$

Different conditions for the numerical convergence are used in practice, which we discuss below. A single iteration of the CTMRG algorithm in Eq. (4.3) is itself composed of four parts, known as *moves*, one for each direction

$$c = c_{\mathrm{u}} \circ c_{\mathrm{r}} \circ c_{\mathrm{d}} \circ c_{\mathrm{l}}. \tag{4.5}$$

In the following, we discuss a *left move* c_{l}, noting that the other directional moves $c_{\mathrm{d}}, c_{\mathrm{r}}, c_{\mathrm{u}}$ work analogously. During the left move, only the environment tensors describing the

[2]Note that there are several variants for this algorithm. The original algorithm was formulated for local tensors, which are invariant under permutation of indices [106, 107]. This version can be particularly useful if one wants to make use of the lattice symmetries of the problem at hand. Here we present the more general formulation of the algorithm that does not rely on lattice symmetries [108].

lattice environment to the left of site i are modified

$$c_{\mathrm{l}}(e(A)) = \{C'_{\mathrm{ul}}, C_{\mathrm{ur}}, C'_{\mathrm{dl}}, C_{\mathrm{dr}}, T'_{\mathrm{l}}, T_{\mathrm{d}}, T_{\mathrm{r}}, T_{\mathrm{u}}\}. \tag{4.6}$$

The left move c_{l} works by first absorbing a column of the infinite tensor network into the effective environment tensors describing the left part of the infinite lattice

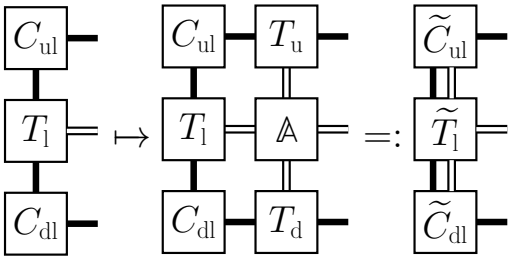

(4.7)

Notice that the column of the infinite tensor network we absorb in the above step is already represented using the effective environment tensors. This first operation results in new environment tensors $\widetilde{C}_{\mathrm{ul}}, \widetilde{T}_{\mathrm{l}}$ and $\widetilde{C}_{\mathrm{dl}}$, where the environment bond dimension has been increased to $\chi_E \cdot \chi_B^2$. As we aim to converge the effective environment tensors at a fixed environment bond dimension χ_E the next step is to use a set of projectors to truncate the bond dimension from $\chi_E \cdot \chi_B^2$ back to χ_E

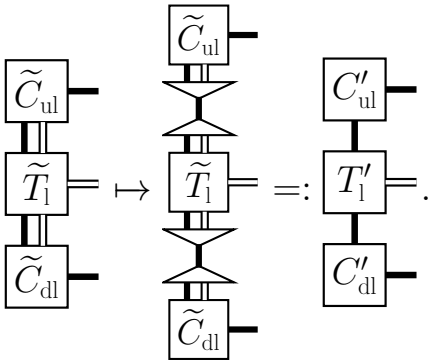

(4.8)

This concludes the left move. We describe how to obtain a useful set of projectors below. After analogous moves towards the bottom, right, and top directions, we have updated all environment tensors and concluded a single CTMRG iteration. Equations (4.7) and (4.8) can be interpreted as a power-method scheme to identify a finite bond dimension approximation of the dominant eigenvector of a column of the tensor network shown in Fig. 4.1. From this perspective, the converged CTMRG environments are a set of tensors that can be used to assemble approximations of the dominant left and right eigenvectors of a column and row of the tensor network simultaneously. Only once this is the case

will the CTMRG algorithm converge.

Defining Accurate Projectors

A part of the CTMRG algorithm critical for its success is using well-chosen projectors in Eq. (4.8). The projectors truncate the virtual spaces on the effective environment tensors to subspaces thereof. Choosing the relevant subspaces for this truncation is critical. To identify these relevant subspaces and construct the projectors accordingly as introduced in [111], we define a matrix M, build as an explicit contraction of two tensors ρ_u and ρ_d over the virtual spaces we aim to truncate. The tensors ρ_u and ρ_d are chosen such that the matrix M represents the parts of our network surrounding the virtual space to be truncated

$M = \rho_\mathrm{d} \cdot \rho_\mathrm{u} =$ 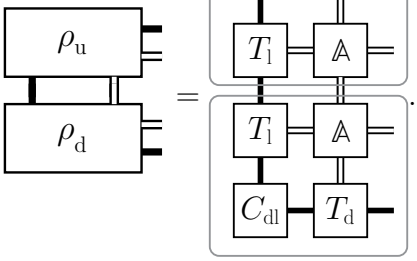

. (4.9)

The insertion of well-chosen projectors to truncate to the relevant subspace should change this matrix M as little as possible

$M =$ 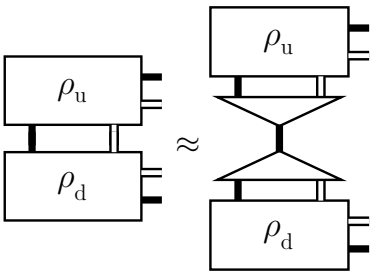

(4.10)

to achieve a good low-rank approximation. To this end, we can perform a singular value decomposition of the matrix $M = USV^\dagger$, which can be used to write the identity on the virtual spaces we want to truncate as

$$\mathbb{1} = \rho_\mathrm{u}\rho_\mathrm{u}^{-1}\rho_\mathrm{d}^{-1}\rho_\mathrm{d} = \rho_\mathrm{u}M^{-1}\rho_\mathrm{d} = \rho_\mathrm{u}VS^{-1}U^\dagger\rho_\mathrm{d}. \tag{4.11}$$

The basis, identified by the singular value decomposition of M, can then be used to truncate the rank of the identity in Eq. (4.11) and thus obtain the projectors[3] that give an optimal low-rank approximation of the matrix M[4]

$$P_{\mathrm{d}} = \quad = \rho_{\mathrm{u}} V \sqrt{\widetilde{S}^{-1}} = \quad ,$$

$$P_{\mathrm{u}} = \quad = \sqrt{\widetilde{S}^{-1}} U^{\dagger} \rho_{\mathrm{d}} = \quad . \tag{4.12}$$

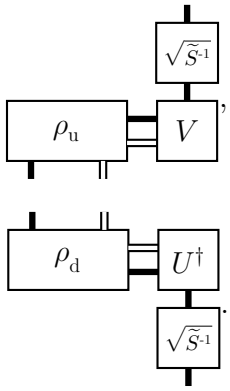

In the equations above, we denote the truncated singular values as $\widetilde{S}$. The number of singular values kept when truncating to $\widetilde{S}$ is the chosen environment bond dimension χ_E[5]. The projectors constructed in this fashion can be used during a left move of a CTMRG iteration. Analogous projectors need to be defined for the down, right, and up moves of the CTMRG iteration. Let us mention that the construction of the projectors we have shown above can be made more accurate by constructing the matrix M from different choices ρ_{u} and ρ_{d} representing even larger parts of the network environment of the virtual space we aim to truncate. A commonly used version of the projectors [111] is obtained by choosing

$$\rho_{\mathrm{d}} \cdot \rho_{\mathrm{u}} = \quad . \tag{4.13}$$

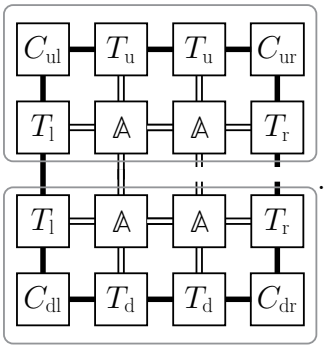

[3] While strictly speaking only the multiplication $P_{\mathrm{u}} \cdot P_{\mathrm{d}}$ is a projector, the individual objects P_{u} and P_{d} are colloquially referred to as projectors as well.

[4] This is optimal, since we obtain a low rank approximation equivalent to the truncated SVD of M: $\rho_{\mathrm{d}}(P_{\mathrm{d}}P_{\mathrm{u}})\rho_{\mathrm{u}} = \rho_{\mathrm{d}}(\rho_{\mathrm{u}} V \widetilde{S}^{-1} U^{\dagger} \rho_{\mathrm{d}})\rho_{\mathrm{u}} = (USV^{\dagger})V\widetilde{S}^{-1}U^{\dagger}(USV^{\dagger}) = U\widetilde{S}V^{\dagger}$.

[5] We note that the tensors P_{u} and P_{d} in Eq. (4.12) truncate from a space of dimension $\chi_E \chi_B^2$ to a space of size χ_E. Hence, for typical values of χ_B we are only keeping a small percentage of the singular values, such that the use of iterative SVD solvers can be helpful in reducing computational time, as is demonstrated in [P6].

While the projectors resulting from Eq.(4.13) are more accurate, their construction is also computationally more expensive. To distinguish between these projectors, we refer to those based on Eq.(4.13) as *full*-projectors, while calling those based on Eq. (4.9) *half*-projectors.

Remarks on the CTMRG Algorithm

A few annotations are needed when using the CTMRG algorithm for numerical tasks in quantum many-body physics. Firstly, we need to establish which requirements should be set in practice for considering the algorithm as converged. Here, we can use several strategies, the least stringent of which is to calculate the value of a local observable after each CTMRG iteration and consider the algorithm to be converged once this local observable has converged to a given accuracy. This can have the downside, however, that not all observables that one might want to calculate, especially non-local ones like, e.g., correlation functions, converge equally fast. Hence, a more common approach is to look for convergence in the effective environment tensors themselves. For example, we can require the singular values of the C-tensors to be converged to some accuracy. Going one more step beyond this, we can even require the environment tensors to converge element-wise [113, 114][P6]. To achieve an element-wise convergence, we need to fix the freedom that is present in the singular value decomposition when constructing the projectors

$$M = USV^\dagger = (U\Gamma)S(\Gamma^\dagger V^\dagger) \tag{4.14}$$

where Γ are diagonal unitaries[6]. For practical purposes this freedom of the SVD can be fixed, by choosing Γ, such that the largest magnitude entry of every singular vector in U is a positive real number[7]. This element-wise convergence is not necessary for the accurate determination of expectation values, but is very useful when calculating gradients, cf. Sect. 4.2.3.

Further, let us mention that the CTMRG algorithm defined here on the square lattice can, however, be applied successfully to problems of many-body physics on other two-dimensional lattices. While extensions of the CTMRG algorithm, which work directly on other lattice geometries have been proposed [115, 116, 117], an alternative procedure is to map the tensor product state ansatz from a non-square lattice onto a square lattice, such that using the square-lattice CTMRG algorithm becomes possible [118, 119]. Alternatively, we can work directly with a square lattice tensor product state ansatz on

[6] They can in principle be block-diagonal if degenerate singular values are present.

[7] If the largest magnitude entry is not unique, we can fix the first one of these degenerate entries of the singular vectors.

a non-square lattice. These approaches are described for several lattices in [P6].

Lastly, we note that the computational complexity of the CTMRG algorithm scales as $\mathcal{O}(\chi_E^3 \chi_B^6)$. This scaling is due to the projectors [111], where the construction of the matrix M in Eq. (4.9) and the subsequent SVD thereof are the dominant contributors. It is the aim of our publication [P4] to reduce the complexity of the CTMRG algorithm without sacrificing its accuracy. To achieve this, we define new environment tensors, treating the two layers of the double-layer tensor network separately.

4.2 Ground State Determination

Identifying the optimal approximation of the ground state of a quantum many-body Hamiltonian using a tensor product state ansatz

$$\min_A \frac{\langle \Psi_{\mathrm{TPS}}(A)| \hat{H} |\Psi_{\mathrm{TPS}}(A)\rangle}{\langle \Psi_{\mathrm{TPS}}(A)|\Psi_{\mathrm{TPS}}(A)\rangle}, \tag{4.15}$$

where A represents the variational parameters contained in the local tensors, is a difficult task that is crucial for the utility of the tensor product state ansatz class. The approaches used for ground state search using tensor product states can be broadly put into two categories. For one, we can use a Trotterized imaginary time evolution [29, 120, 121, 122] to obtain a ground state approximation as we briefly outline in Sec. 4.2.1. The alternative to this procedure is to use gradient-based ground state search [123, 124, 125, 30, 126, 31], which will be the focus of this thesis. We introduce the gradient-based optimization for infinite tensor product states in Sec. 4.2.2 and discuss how to efficiently compute the gradient within the CTMRG framework in Sec. 4.2.3. We further mention how to use the gradient information during the optimization to perform approximate second-order optimization in Sec. 4.2.4 and point to challenges and efficient procedures for this ground state search in Sec. 4.2.5. In the context of tensor product states on finite lattices, we discuss an alternative gradient-based optimization procedure based on the time-dependent variational principle [127, 128, 31] in our publication [P5].

4.2.1 Trotterized Imaginary Time Evolution

Most early approaches to identifying optimal ground state approximations with tensor product states have been based on Trotterized imaginary time evolution [29, 120, 121]. These approaches are based on the fact that every state $|\Psi\rangle$ that has a non-zero overlap with the ground state $|\Psi_0\rangle$ of the system can be transformed into the ground state by

an imaginary time evolution

$$|\Psi_0\rangle = \lim_{\tau\to\infty} \frac{e^{-\tau H}|\Psi\rangle}{||e^{-\tau H}|\Psi\rangle||}. \tag{4.16}$$

In practice, the imaginary time evolution is performed using two approximations. Firstly, the imaginary time evolution operator is approximated using the Suzuki-Trotter decomposition

$$e^{-\tau H} = \left(e^{-\delta\tau H}\right)^n, \quad e^{-\delta\tau H} \approx \prod_{\langle i,j\rangle} U_{i,j} = \prod_{\langle i,j\rangle} e^{-\delta\tau h_{ij}}, \tag{4.17}$$

which we exemplify here for the case of a Hamiltonian with nearest neighbor interactions $H = \sum_{\langle i,j\rangle} h_{ij}$. Using this representation of the imaginary time evolution operator, we apply the local operators $e^{-\delta\tau h_{ij}} \approx \mathbb{1} - \delta\tau h_{ij}$ to the tensor product state one after another[8]. Applying such a local operator will increase the bond dimension corresponding to the edge between site i and j. To keep the tensor product state at a fixed bond dimension, a truncation scheme is used to reduce the bond dimension of the edge between site i and j. This truncation represents the second practical approximation of the imaginary time evolution. It can be done using what is known as a *simple update* [29, 120], where the truncation is performed using a singular value decomposition of only the tensors associated with site i and j. The more computationally expensive but more accurate alternative truncation scheme, is known as the *full update* [121, 122]. It improves the accuracy of the approximate imaginary time evolution by using the CTMRG environment tensors to account for the lattice environment of the bond between site i and j when performing the truncation.

The central problem with the approaches using the Trotterized imaginary time evolution is not the Trotterization of the imaginary time evolution operator [123]. This approximation can be made more accurate by decreasing the imaginary time evolution step $\delta\tau$. The more severe approximation is done when we truncate the bond dimension on a single bond after applying $e^{-\delta\tau h_{ij}} \approx \mathbb{1} - \delta\tau h_{ij}$. In this step, we identify new local tensors for sites i and j, which are chosen to be a good approximation locally. However, this does not imply that these new tensors represent a state that is optimally truncated globally after applying all local operators corresponding to a full imaginary time evolution step. Despite this, these schemes (especially the simple update) are being used due to their comparatively low computational cost, allowing for a large bond dimension in the ansatz. The computational complexity of the simple update algorithm scales as

[8]For small matrices h_{ij}, we can of course also compute the matrix exponential exactly.

$\mathcal{O}(d\chi_B^z)$ with d referring to the local Hilbert space dimension and z to the number of nearest neighbors to each lattice site [129].

4.2.2 Gradient Based Optimization

An alternative to the Trotterized imaginary time evolution for the ground state search is using the energy gradient with respect to the variational parameters in the infinite tensor product state ansatz

$$\nabla E(A) = \frac{\partial}{\partial A} \frac{\langle \Psi_{\mathrm{TPS}}(A)| \hat{H} |\Psi_{\mathrm{TPS}}(A)\rangle}{\langle \Psi_{\mathrm{TPS}}(A)|\Psi_{\mathrm{TPS}}(A)\rangle}. \tag{4.18}$$

This approach holds great promise for accurate ground state determination. To understand this, suppose the gradient with respect to the variational parameters in the infinite tensor product state can be calculated. In that case, we can update the variational parameters of the state in a way that guarantees a global improvement of the ansatz, which is in stark contrast to the update of parameters in the approaches based on Trotterized imaginary time evolution. It is generally found that the gradient-based optimization schemes yield better ground state approximations for a tensor product state ansatz at a given bond dimension, as demonstrated, e.g., in [P6].

However, calculating the energy gradient with respect to the variational parameters of the infinite tensor product state ansatz is a challenging task. This is because the energy is a highly non-linear function of the variational parameters (the entries in the local tensors) in the ansatz[9] due to the periodically repeating unit cell of tensors, cf. Sec. 2.2. Additionally, we cannot evaluate the energy expectation value of a given infinite tensor product state exactly, and approximation schemes, such as the CTMRG, need to be employed, cf. Sec 4.1.1. In the pioneering works [123, 124], the evaluation of the infinite terms that formally appear in the energy gradient was consolidated into a large but finite number of tensor network diagrams within a certain approximate contraction method, e.g., the CTMRG. These works proved the utility of gradient-based optimization schemes by demonstrating that for a tensor product state of a fixed bond dimension, lower energies can be achieved with this method, and more importantly, the properties of challenging, correlated ground states of frustrated magnetic models could be represented correctly. In a later work [125], it was pointed out that the computation

[9] This difficulty might be considered the reason that it took more than ten years after the introduction of the tensor product state ansatz [12] that a gradient-based scheme for these states was first proposed [123]

of the gradient can be performed in an automated fashion, without the need to evaluate large numbers of specific tensor network diagrams with the use of automatic differentiation. Automatic differentiation is already a prominent tool, e.g., in the context of machine learning, and we give an introduction to automatic differentiation in Sec. 2.4 as well as App. A-D of [P6].

4.2.3 The Gradient at the CTMRG Fixed-Point

As mentioned above, the calculation of the energy gradient in the context of infinite tensor product states is fundamentally connected to an approximation scheme for calculating the energy expectation value, as this task cannot be done exactly. For the calculation of the energy expectation value, we can use the effective environment tensors that can be generated from the local tensors of the tensor product state ansatz using the CTMRG algorithm, as described in Sec. 4.1.1. All of these effective environment tensors will thus depend on the variational parameters of the ansatz, and hence have to be taken into account when the gradient is calculated. This, in principle, requires taking the derivative via the chain rule through the entire iterative steps of the CTMRG algorithm [125]. However, it is possible to avoid this because the CTMRG algorithm reaches convergence at a fixed point [125, 113], where every further iteration reproduces the same effective environment tensors

$$e^*(A) = c(A, e^*(A)). \tag{4.19}$$

As mentioned in the remarks on the CTMRG in Sec. 4.1.1 special care has to be taken to fix the freedom inherent to the SVD to arrive at a true fixed point where the effective environment tensors are converged element-wise. The algorithmic steps for the calculation of the energy, once the fixed point is reached, are illustrated as a computational graph in Fig. 4.2. There we denote the function that calculates the energy expectation value from the local tensors A, the Hamiltonan H and the converged effective environment tensors $e^*(A)$ as

$$\langle H \rangle = \mathcal{E}(e^*(A), A, H). \tag{4.20}$$

Using that at the fixed point, the effective environment tensors will be reproduced infinitely often, we can write the energy gradient as

$$\frac{\partial \langle H \rangle}{\partial A} = \frac{\partial \mathcal{E}}{\partial A} + \frac{\partial \mathcal{E}}{\partial e^*} \sum_{n=0}^{\infty} \left(\frac{\partial c}{\partial e^*} \right)^n \frac{\partial c}{\partial A}. \tag{4.21}$$

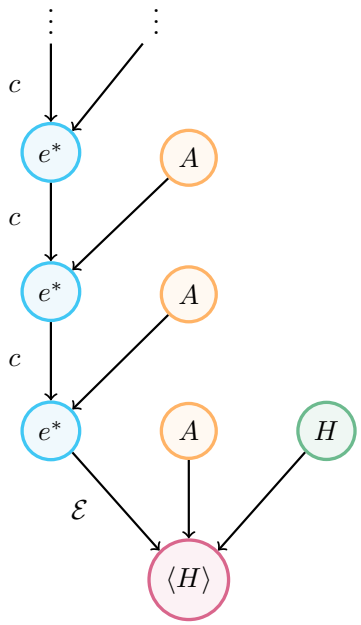

Figure 4.2.: Computational graph of the CTMRG procedure for calculating the energy density at fixed point. Taken from [P6].

This equation formally requires only the calculation of a single Jacobian of the CTMRG iteration function c[10] at the fixed point from which the entire gradient can be created by an infinite sum. In practice, summing up a finite number of the above terms converges the gradient to a given accuracy.

4.2.4 Approximate Second Order Optimization

When optimizing the tensor product state based on the information we obtain from the energy and the gradient, several schemes have been designed to additionally make use of this information gathered in the previous optimization steps. One prominent example of these schemes, the Broyden–Fletcher–Goldfarb–Shanno (BFGS) method, which is used as the optimization workhorse in this thesis, is a version of the quasi-Newton methods. In the following, we will briefly outline the idea for the quasi-Newton methods for optimization, following mostly [133, 134].

In quasi-Newton methods, we construct a local, quadratic model m_k of the energy landscape around a certain set of ansatz-parameters A_k (in the case of a tensor product

[10] A single CTMRG iteration c is a composition of simple tensor network contractions, for which the evaluation of the Jacobian is simple, as well as the computation of singular value decomposition for which the same is also possible [130, 131, 132].

state, the entries in the local tensors) at optimization step k

$$m_k(p) = E_k + \nabla E^T p + \frac{1}{2} p^T B_k p. \tag{4.22}$$

The model is constructed such that it reproduces the energy and the gradient at the ansatz-parameters A_k: $m_k(0) = E_k$, $\nabla m_k(0) = \nabla E_k$. The exact calculation of the Hessian is prohibitively expensive, as it requires us to take the derivative of every one of the possibly large number of components in the gradient. For this reason, we choose for the matrix B_k an appropriate symmetric, positive definite approximation of the Hessian. With these properties, such a model has a minimizer $p_k = -B_k^{-1}\nabla E$, which we use as a search direction to find a new set of parameters $A_{k+1} = A_k + \alpha p_k$ using a line search algorithm to find a suitable number α. Now the approach taken by the quasi-Newton methods is to calculate the energy E_{k+1} and the gradient ∇E_{k+1} at the new parameters A_{k+1} and to choose B_{k+1} from information at the last parameter points A_k. Concretely, we impose that the model m_{k+1} centered around the new parameter points A_{k+1}, reproduce the gradient at the last parameter point $A_k = A_{k+1} - \alpha_k p_k$

$$\nabla m_{k+1}(-\alpha_k p_k) = \nabla E_{k+1} - \alpha_k B_{k+1} p_k \stackrel{!}{=} \nabla E_k, \tag{4.23}$$

or equivalently

$$B_{k+1} \underbrace{(A_{k+1} - A_k)}_{=:s_k} = \underbrace{\nabla E_{k+1} - \nabla E_k}_{=:y_k}. \tag{4.24}$$

From this requirement, we can construct an updated symmetric, positive definite approximation of B_{k+1} if $s_k^T y_k > 0$[11]. However, the requirement in Eq. (4.24), together with enforcing the fact that B_{k+1} should be symmetric and positive definite, does not completely fix the solution B_{k+1}. The different schemes for choosing B_{k+1} define the different flavors of quasi-Newton methods. The most commonly used choice to obtain the update B_{k+1} is the BFGS method. This method additionally requires the inverse of B_{k+1} to be as close as possible to the inverse of B_k [134].

4.2.5 Challenges and Efficient Procedures for Gradient-Based Optimization

In many cases, the optimization using gradient-based schemes is straightforward, in that the norm of the gradient $||\nabla E||$ mainly decreases throughout the optimization iterations. A certain value for the norm of the gradient is then taken as a termination condition for the optimization. Choosing termination conditions for the optimization that require a

[11] This can be ensured by using an appropriate line-search procedure that determines α_k [133]

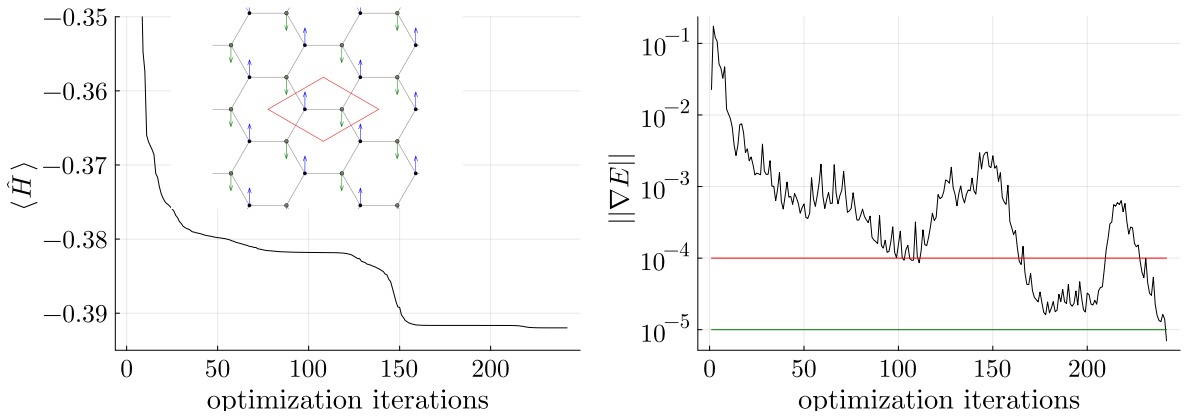

Figure 4.3.: (a) Energy per unit cell of the infinite tensor product states (bond dimension $\chi_B = 4$) during the gradient-based optimization of the Kitaev model on the honeycomb lattice [135]. We find a plateau in the energy around iteration 100, where the states have anti-ferromagnetic order, as is illustrated in the inset. In the final optimized state, no local magnetization is present. (b) Norm of the gradient of the energy during the optimization. We highlight the gradient norms that, if used as convergence criteria, lead to qualitatively different ground state approximations.

smaller gradient norm leads to more accurate, but qualitatively similar approximations in these cases. However, we point out that in some settings, we might find plateaus during the optimization on which the energy seems to have converged and the gradient has become small. An example of such a behavior can occur when optimizing the tensor product states as the ground state of the Kitaev-honeycomb model [135], which is shown in Fig. 4.3. The final state using the convergence condition $||\nabla E|| < 10^{-5}$ yields a vanishing magnetization, as is expected for the model. However, around iteration step 100, we already find a plateau in the energy, cf. Fig. 4.3a, where the gradient norm becomes smaller than $||\nabla E|| < 10^{-4}$, cf. Fig. 4.3b. If we investigate the properties of the states associated with this plateau, we find that they are anti-ferromagnetically ordered, as we illustrate in the inset of Fig. 4.3a. This example demonstrated the necessity for quite stringent convergence criteria as well as the usefulness of additional optimization steps even if the state seems to have converged.

In addition to the challenges intrinsic to the gradient-based optimization discussed above, problems in the optimization can arise when inaccurate approximations are taken in the calculation of the energy expectation value via the CTMRG. This is because such approximations can be exploited during the optimization, yielding suboptimal tensor

product state approximations of the ground state. The accuracy of the energy approximation with the CTMRG at a fixed environment bond dimension χ_E, however, depends on the properties of the tensor product state in question. Concretely, it depends on the correlation length ξ of the state, which we will discuss in more detail in Sec. 4.3.1. The correlation length of the state might change drastically throughout the optimization procedure. It is thus advisable not to fix the environment bond dimension χ_E for the entire optimization procedure but to choose χ_E dynamically depending on the state. This can be done, e.g., by tracking the norm of the discarded singular values in SVD $\epsilon = ||S - \widetilde{S}||$ used to construct the truncation of the environment bond dimension and choosing χ_E dynamically such that the truncation is done with a fixed accuracy, e.g. $\epsilon < 10^{-4}$ [P6].

Further, we highlight that to improve the efficiency of the gradient-based ground state search, we can reuse results from previous optimization steps. Specifically, during the later stages of the optimization, the tensor product state usually changes only slightly in every optimization step. However, the effective environment tensors must be computed for every state during the optimization using the CTMRG algorithm. A way to significantly reduce the number of CTMRG iterations necessary to compute the effective environment tensors is to use the effective environment tensors from the previous optimization step as a starting point [P6].

4.3 Beyond Local Observables

Representing a quantum state as a tensor product state allows us to access information about the state beyond the local observables. For example, correlation functions can be accessed numerically and analysed with extrapolation schemes [136, 137] as we will discuss in Sec. 4.3.1. It is also possible to access the Fourier transform of the correlation function, the static structure factor [124, 138, 139, 140], for which we briefly describe the simplest approach in the App. of [P3]. Similar numerical approaches also allow for the calculation of low-lying excited states and their momentum resolved spectra [113, 138, 139, 140]. Beyond that, the bulk-boundary correspondence for tensor product states [141], whose derivation we discuss in detail in Sec. 4.3.2, allows us to investigate entanglement quantities, such as the entanglement spectrum [142, 143].

4.3.1 Transfer Matrix and Correlation Functions

Obtaining correlation functions and correlation lengths when using infinite tensor product states can be done numerically with the effective tensors generated with the CTMRG algorithm, cf. Sec. 4.1.1. This always involves finite environment bond dimension approximations. A straightforward, efficient way of obtaining these results exactly is not known for tensor product states[12]. We can express the correlation function along a Cartesian direction at some distance for a completely translation-invariant tensor product state as

$$\langle \psi_{\mathrm{TPS}} | \, \hat{O}[\vec{r}]\hat{O}[\vec{r}+k\vec{e}_y] \, | \psi_{\mathrm{TPS}} \rangle =$$

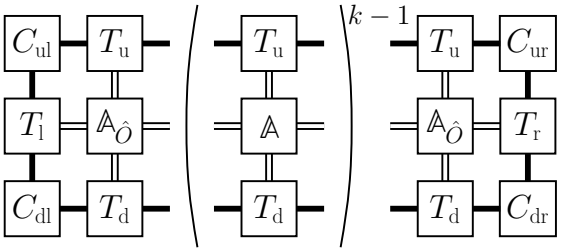

$$= \langle B_{\mathrm{left}} | \, (\mathcal{T}_A)^{k-1} \, | B_{\mathrm{right}} \rangle \, . \tag{4.25}$$

Let us note that in practical calculations, this expression should be properly normalized, similar to Eq. (4.2). Beyond the evaluation of the above formula, we can also analyze the transfer matrix $\mathcal{T}_A$ of the tensor product state. It is defined as a column of double-layer local tensors. For numerical calculations $\mathcal{T}_A$ is expressed using the effective CTMRG environment tensors shown in Eq. (4.25) and therefore inherits the environment bond dimension χ_E as a refinement parameter. If we are interested in the correlation length ξ of our state, which governs the large-distance decay of the connected-correlation functions

$$\langle \hat{O}[\vec{r}]\hat{O}[\vec{r}+k\vec{e}_y] \rangle_c = \langle \hat{O}[\vec{r}]\hat{O}[\vec{r}+k\vec{e}_y] \rangle - \langle \hat{O}[\vec{r}] \rangle \langle \hat{O}[\vec{r}+k\vec{e}_y] \rangle, \tag{4.26}$$

we can perform an eigenvalue decomposition of the transfer matrix

$$\begin{aligned} \langle \hat{O}[\vec{r}]\hat{O}[\vec{r}+k\vec{e}_y] \rangle &= \langle B_{\mathrm{left}} | \left(\sum_i |l_i\rangle \, (\lambda_i)^{l-1} \, \langle r_i| \right) |B_{\mathrm{right}}\rangle \\ &= \langle B_{\mathrm{left}} | l_i \rangle \, (\lambda_1)^{k-1} \sum_i \left(\frac{\lambda_i}{\lambda_1} \right)^{k-1} \langle r_i | B_{\mathrm{right}} \rangle \, . \end{aligned} \tag{4.27}$$

[12] This stands in contrast to the case of translational invariant MPS, where the correlation length can be obtained from the leading gap of the transfer-matrix. Further, the computation of correlation functions only involves tensor networks, which can be contracted exactly and efficiently [15].

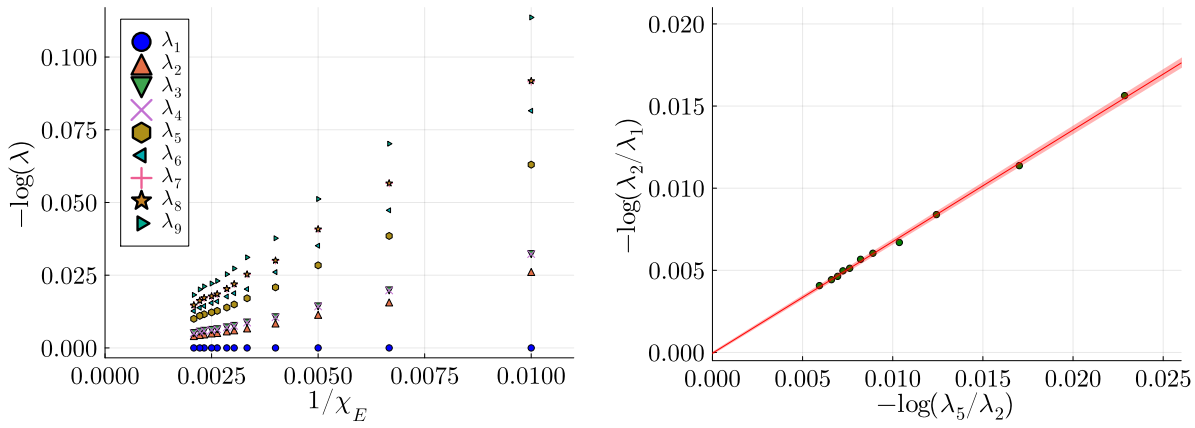

(a) (b)

Figure 4.4.: (a) Largest magnitude eigenvalues of the transfer matrix are shown as a function of the inverse environment bond dimension $1/\chi_E$ for the short-range RVB state on a square lattice. (b) Extrapolation of the inverse correlation length $\frac{1}{\xi} = -\log(\frac{\lambda_2}{\lambda_1})$ against the negative logarithm of a subleading gap [136]. The extrapolation is consistent with an infinite correlation length.

The gap between the leading and first subleading eigenvalues dictates the decay of the connected correlation function at large distances, as the contribution from the leading eigenvalue cancels with the unconnected part. We thus obtain the correlation length $\xi = -\frac{1}{\log(\frac{\lambda_2}{\lambda_1})}$ accurately if bond-dimension χ_E is large enough to approximate the transfer matrix $\mathcal{T}_A$ well. However, for states with very large or even infinite correlation lengths, an approximation at small, finite χ_E will induce an artificial correlation length into the system which depends on the value of χ_E. We illustrate this in Fig. 4.4a, which shows the first eigenvalues of the tensor product state transfer matrix for the short-range RVB state on the square lattice [15], which we discussed in Sect. 3.2.2. We see that at all values of χ_E the correlation length will be finite, while increasing for larger χ_E. In these cases, it may be required to use an extrapolation scheme to extract reliable information [136, 137]. One example of this is to extrapolate the size of the first gap in the transfer matrix-spectrum against subleading gaps, which are expected to vanish as well in a system of infinite correlation length. An example of such a procedure is shown in Fig. 4.4b. We find that the correlation length for the short-range RVB state on the square lattice indeed becomes infinite.

From this we can conclude that while tensor product states can represent states with infinite correlation length and algebraically decaying correlation functions, in numerical calculations this comes at the price of necessitating diverging environment bond-

dimensions[13]. This makes it necessary to use extrapolations.

4.3.2 Bulk-Boundary Correspondence: Entanglement Spectrum and Renyi Entropies

Within the framework of tensor product states, we can construct the reduced density matrix for system bipartitions. This is of interest for the analysis of entanglement quantities such as entanglement entropies (and their topological corrections) or the entanglement spectrum. Remarkably, it is possible to construct the reduced density matrix for a tensor product state in such a form that it becomes an example of a so-called *bulk-boundary correspondence* [141]. Concretely, this means that we can express the reduced density matrix for a region A in terms of operators acting on the virtual boundary of the tensor product state on region A, as we show in the following. That such an expression in terms of boundary operators might be possible follows already from our previous discussion in Sect. 2.3.1, where we discussed the boundary law property of the tensor product states. The central argument to show the boundary law property of these states was that the rank of the reduced density matrix of a region A is limited by the dimension of the virtual space on the boundary of the region A. Deep connections between the spectrum of the reduced density matrix and properties of the physics on the boundary have also been conjectured by Li and Haldane [142, 143]. They noticed that for fractional Hall states, the spectrum of the reduced density matrix is related to the low-lying physical spectrum of the boundary theories for these states.

To construct the bulk-boundary formula for the reduced density matrix, we need to fix the notation and the setting. Here we mainly follow the construction of [141]. We consider a tensor product state on a (finite) cylinder, which we partition into two small cylinders by a cut along the periodic direction of the cylinder. This cut leaves open the virtual indices along the cut, cf. Fig 4.5. Let us call the collection of all physical indices on the left part of the cylinder $\mathbf{S}_L = \{s_{1,1}, ..., s_{1,N_h}, s_{2,1}, ..., s_{2,N_h}, ..., s_{l,1}, ..., s_{l,N_h}\}$ and analogously define $\mathbf{S}_R$ for the collection of all physical indices on the right. The open virtual indices, which connect the two cylinders along the cut, are referred to as Λ. With this collection of indices, we can proceed to define the elements of the tensor networks on the left and right sides of the bipartition[14]. We call these elements $L^{\mathbf{S}_L \Lambda}$ for

[13] The fact that any approximation of the connected correlation function at finite χ_E will yield a finite correlation length is to be expected already from the form of Eq. (4.25). This formula is very similar to an expectation value of an MPS, which always yield a finite correlation length.

[14] Notice the slightly unusual directionality of the legs on the cut, which we choose for later notational convenience.

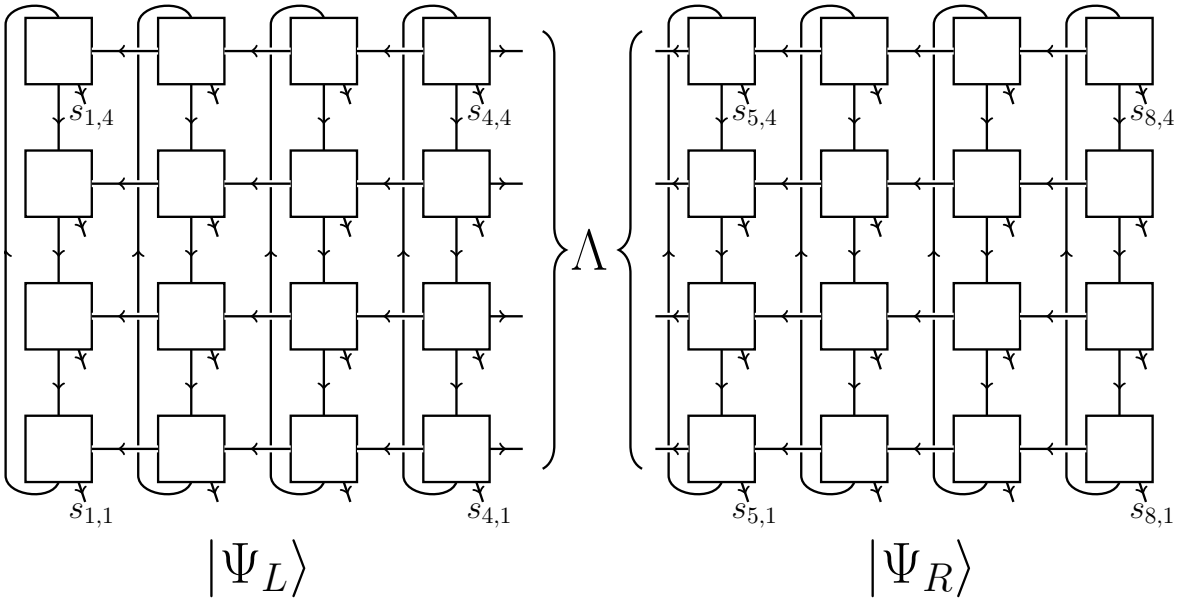

Figure 4.5.: Illustration of a bipartition of a tensor product state on a finite cylinder. $|\psi_L\rangle$ is defined as a state on the physical degrees of freedom of the left part of the cylinder and the virtual degrees of freedom on the cut. The collective virtual degrees of freedom on the cut are labeled by Λ. We define $|\psi_R\rangle$, the state on the right part of the cylinder, completely analogously.

the left-hand side and analogously for the right part $R^{\mathbf{S}_R\Lambda}$. They can be seen as elements of the (multi-leg) vectors $|\psi_L\rangle = \sum_{\mathbf{S}_L\Lambda} L^{\mathbf{S}_L\Lambda} |\mathbf{S}_L\rangle |\Lambda\rangle$ and $|\psi_R\rangle = \sum_{\mathbf{S}_R\Lambda} R^{\mathbf{S}_R\Lambda} |\mathbf{S}_R\rangle |\Lambda\rangle$ that we show in Fig. 4.5. With this notation, we can write the tensor product state vector as

$$\begin{aligned} |\psi\rangle &= \sum_{\Lambda} \langle\Lambda| \langle\Lambda| |\psi_L\rangle |\psi_R\rangle \\ &= \sum_{\mathbf{S}_L\mathbf{S}_R} \sum_{\Lambda} L^{\mathbf{S}_L\Lambda} R^{\mathbf{S}_R\Lambda} |\mathbf{S}_L\mathbf{S}_R\rangle . \end{aligned} \tag{4.28}$$

In case we fix a physical configuration $\mathbf{S}_L$ or $\mathbf{S}_R$, we can also define state vectors purely on the virtual spaces

$$|L^{\mathbf{S}_L}\rangle = \sum_{\Lambda} L^{\mathbf{S}_L\Lambda} |\Lambda\rangle , \qquad |R^{\mathbf{S}_R}\rangle = \sum_{\Lambda} R^{\mathbf{S}_R\Lambda} |\Lambda\rangle . \tag{4.29}$$

We now investigate the reduced density matrix for the left part of the cylinder in this

setting

$$\begin{aligned}\rho_L &= \mathrm{Tr}_R[|\psi\rangle\langle\psi|] \\ &= \sum_{\mathbf{S}_R} \langle \mathbf{S}_R| \sum_{\mathbf{S}_L\widetilde{\mathbf{S}_R}\mathbf{S}'_L\widetilde{\mathbf{S}'_R}} \sum_{\Lambda\Lambda'} L^{\mathbf{S}_L\Lambda} R^{\widetilde{\mathbf{S}_R}\Lambda} |\mathbf{S}_L\widetilde{\mathbf{S}_R}\rangle \langle \mathbf{S}'_L\widetilde{\mathbf{S}'_R}| (L^{\mathbf{S}'_L\Lambda'})^* (R^{\widetilde{\mathbf{S}'_R}\Lambda'})^* |\mathbf{S}_R\rangle \\ &= \sum_{\mathbf{S}_L\mathbf{S}'_L\mathbf{S}_R} \sum_{\Lambda,\Lambda'} L^{\mathbf{S}_L\Lambda} R^{\mathbf{S}_R\Lambda} |\mathbf{S}_L\rangle \langle \mathbf{S}'_L| (L^{\mathbf{S}'_L\Lambda'})^* (R^{\mathbf{S}_R\Lambda'})^*.\end{aligned} \tag{4.30}$$

The first thing to notice from this is that we can rewrite much of this expression in terms of the purely virtual state vectors of Eq. (4.29) and their corresponding density matrices

$$\sigma_L = \sum_{\mathbf{S}_L} |L^{\mathbf{S}_L}\rangle \langle L^{\mathbf{S}_L}|, \qquad \sigma_R = \sum_{\mathbf{S}_R} |R^{\mathbf{S}_R}\rangle \langle R^{\mathbf{S}_R}|. \tag{4.31}$$

This rewriting leads us to the form

$$\begin{aligned}\rho_L &= \sum_{\mathbf{S}_L\mathbf{S}'_L} \sum_{\Lambda\Lambda'} L^{\mathbf{S}_L\Lambda} |\mathbf{S}_L\rangle \langle \mathbf{S}'_L| (L^{\mathbf{S}'_L\Lambda'})^* \langle\Lambda| \sigma_R |\Lambda'\rangle \\ &= \sum_{\mathbf{S}_L\mathbf{S}'_L} |\mathbf{S}_L\rangle \langle (L^{\mathbf{S}_L})^*| \sigma_R |(L^{\mathbf{S}'_L})^*\rangle \langle \mathbf{S}'_L|.\end{aligned} \tag{4.32}$$

At this stage, we already have a form exhibiting some of the properties we set out to find. ρ_L can be seen as a map that first maps from the physical space on the left part of the cylinder to the virtual space on the cut. There, the operator σ_R is applied, which is defined purely on the virtual boundary, and the result is mapped back to the physical space afterward. However the mapping from physical to virtual space $\sum_{\mathbf{S}'_L} |(L^{\mathbf{S}'_L})^*\rangle \langle \mathbf{S}'_L|$ is not yet an isometry as the states $|L^{\mathbf{S}'_L}\rangle$ are not orthonormal. This can be achieved by moving to a different basis

$$|\chi_\Gamma\rangle = \sum_{S_L} \langle\Gamma| \frac{1}{\sqrt{\sigma_L}} |L^{\mathbf{S}_L}\rangle |\mathbf{S}_L\rangle. \tag{4.33}$$

Note that because σ_L is a density matrix and hence positive-semidefinite, we can define a unique square root of this matrix. $|\Gamma\rangle$ labels an orthonormal basis on the range[15] of

[15]The space orthogonal to the kernel of a matrix.

σ_L, while $|\chi_\Gamma\rangle$ is an orthonormal basis on the physical space as well[16]. We find that after we perform this basis change

$$\begin{aligned}\rho_L = \sum_{\mathbf{S}_L\mathbf{S}'_L}\sum_{\Gamma\Gamma'} |\chi_\Gamma\rangle \underbrace{\langle\chi_\Gamma|\mathbf{S}_L\rangle}_{\langle L^{\mathbf{S}_L}|\frac{1}{\sqrt{\sigma_L}}|\Gamma\rangle} \langle(L^{\mathbf{S}_L})^*|\,\sigma_R\,|(L^{\mathbf{S}'_L})^*\rangle\,\langle\mathbf{S}'_L|\chi_{\Gamma'}\rangle\,\langle\chi_{\Gamma'}| \\ = \langle\Gamma^*|\,\big(\frac{1}{\sqrt{\sigma_L}}\big)^{\mathrm{T}}\,|(L^{\mathbf{S}_L})^*\rangle \\ = \sum_{\Gamma\Gamma'} |\chi_\Gamma\rangle\,\langle\Gamma^*|\,\big(\frac{1}{\sqrt{\sigma_L}}\big)^{\mathrm{T}}\sigma_L^{\mathrm{T}}\sigma_R\sigma_L^{\mathrm{T}}\big(\frac{1}{\sqrt{\sigma_L}}\big)^{\mathrm{T}}\,|\Gamma'^*\rangle\,\langle\chi_{\Gamma'}| \\ = \sum_{\Gamma\Gamma'} |\chi_\Gamma\rangle\,\langle\Gamma^*|\,\sqrt{\sigma_L^{\mathrm{T}}}\sigma_R\sqrt{\sigma_L^{\mathrm{T}}}\,|\Gamma'^*\rangle\,\langle\chi_{\Gamma'}|\,,\end{aligned} \tag{4.34}$$

where we have used that $\sum_{\mathbf{S}_L}|(L^{\mathbf{S}_L})^*\rangle\,\langle(L^{\mathbf{S}_L})^*| = \sigma_L^{\mathrm{T}}$. By identifying the isometries $U = \sum_\Gamma |\chi_\Gamma\rangle\,\langle\Gamma^*|$, we finally obtain the desired bulk-boundary form for the reduced density matrix

$$\rho_L = U\sqrt{\sigma_L^{\mathrm{T}}}\sigma_R\sqrt{\sigma_L^{\mathrm{T}}}U^\dagger. \tag{4.35}$$

This form is remarkable for several reasons. Firstly, as the isometries do not change the spectrum of the reduced density matrix[17], and hence we have found a set of operators on the virtual boundary of the tensor product states that share the spectrum of the density matrix. This can be used for numerical purposes, as computing properties of reduced density matrices for large regions A would be challenging otherwise due to the exponential growth of the physical Hilbert space. Secondly, it is interesting from a conceptual point of view, that we can calculate the exact expectation value of any observable in the domain of ρ_L by mapping it to the virtual boundary and subsequently evaluating it with the boundary-operators $\langle O\rangle = \mathrm{Tr}(\rho_L O) = \mathrm{Tr}(\sqrt{\sigma_L^{\mathrm{T}}}\sigma_R\sqrt{\sigma_L^{\mathrm{T}}}(U^\dagger O U))$.

16

$$\begin{aligned}\langle\chi_{\Gamma'}|\chi_\Gamma\rangle &= \sum_{\mathbf{S}_L,\mathbf{S}'_L}\langle\Gamma|\frac{1}{\sqrt{\sigma_L}}|L^{\mathbf{S}'_L}\rangle\,\langle L^{\mathbf{S}_L}|\frac{1}{\sqrt{\sigma_L}}|\Gamma'\rangle\,\langle\mathbf{S}'_L|\mathbf{S}_L\rangle \\ &= \sum_{\mathbf{S}_L}\langle\Gamma|\frac{1}{\sqrt{\sigma_L}}\sigma_L\frac{1}{\sqrt{\sigma_L}}|\Gamma'\rangle = \delta_{\Gamma\Gamma'}.\end{aligned}$$

17 The rank of the reduced density matrix is capped at the dimension of the virtual space.

Entanglement Spectrum

We now discuss the application of this formula for the numerical calculation of the entanglement spectrum for a tensor product state of interest. The entanglement spectrum [142, 143] refers to the spectrum of the entanglement Hamiltonian H_E, which we define via

$$\rho_L = \exp(-H_E), \tag{4.36}$$

such that by taking the negative logarithm of the eigenvalues of ρ_L we can obtain the spectrum of H_E. Using the translation-invariant infinite tensor product states, it is most convenient to treat a system on a finite-circumference cylinder of infinite length. This is because we can easily represent σ_L and σ_R approximately using the effective environment tensors from the CTMRG algorithm discussed in Sect. 4.1.1 in this situation. As the T-tensors resulting from the CTMRG algorithm are an approximation of an infinite strip of local double-layer tensors of the state

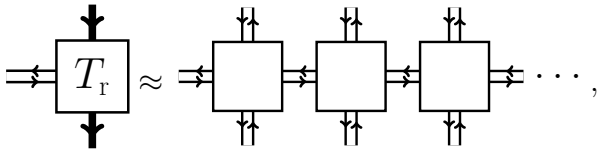

(4.37)

we can approximate

$\sigma_R =$

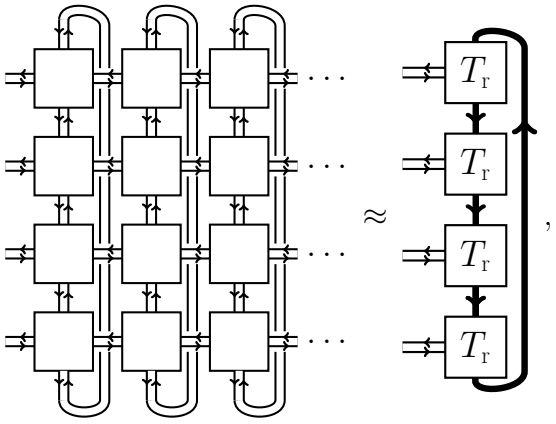

(4.38)

as a matrix product operator (MPO) built from the T-tensors with periodic boundary conditions [97]. For the entanglement spectrum, we are interested in two quantities. Firstly, the logarithm of the eigenvalues of ρ_L and secondly, the momentum eigenvalue that we can associate with the corresponding eigenvector in translationally invariant settings. For these quantities, it is possible to focus on $\sigma_L^{\mathrm{T}}\sigma_R$ instead, which is more

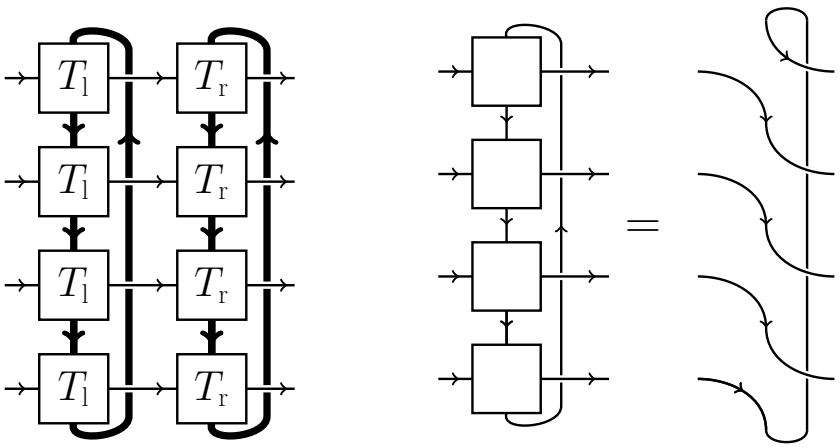

(a) (b)

Figure 4.6.: (a) Illustration of $\sigma_L^\mathrm{T}\sigma_R$ in MPO form. We fold open the virtual indices corresponding to *bra*- and *ket*-layer to perform the multiplication. (b) Translation operator, generating the momenta along the cylinder in MPO form.

convenient since we have numerical access to an approximation of σ_L and σ_R. This is possible as they are related to each other by a similarity transform

$$\sigma_L^\mathrm{T}\sigma_R = \sqrt{\sigma_L^\mathrm{T}}\left(\sqrt{\sigma_L^\mathrm{T}}\sigma_R\sqrt{\sigma_L^\mathrm{T}}\right)\frac{1}{\sqrt{\sigma_L^\mathrm{T}}} \tag{4.39}$$

and hence have identical eigenvalues. Of course, the eigenvectors are not identical; however, they share the same momentum eigenvalue. To see this, let us consider an eigenvector of $\sigma_L^\mathrm{T}\sigma_R$, which we refer to as $|\gamma\rangle$. The corresponding eigenvector of $\sqrt{\sigma_L^\mathrm{T}}\sigma_R\sqrt{\sigma_L^\mathrm{T}}$ that shares the same eigenvalue is $\frac{1}{\sqrt{\sigma_L^\mathrm{T}}}|\gamma\rangle$. Since $\frac{1}{\sqrt{\sigma_L^\mathrm{T}}}$ is translation invariant by construction, it commutes with the translation operator, and we thus obtain the same momentum eigenvalue as for $|\gamma\rangle$. Consequently, whenever we are interested in the properties of the entanglement spectrum for numerical purposes, we consider $\sigma_L^\mathrm{T}\sigma_R$, the MPO form of which we illustrate in Fig. 4.6a. For completeness, let us note that the translation operator, from which we generate the momentum eigenvalue, can also be written in the form of an MPO, which we show in Fig. 4.6b.

With the description of $\sigma_L^\mathrm{T}\sigma_R$ at hand, we can proceed to use iterative eigen-solvers to obtain the largest eigenvalues and eigenvectors of ρ_L, which correspond to the smallest eigenvalues of H_E, which is commonly of interest. Let us mention that the setup on a cylinder of finite circumference leads to discrete values of the momenta of the entanglement spectrum. This can be used as an advantage for cases in which we want to access the counting of edge modes to identify certain states through the entanglement spec-

trum, as we do in publication [P1,P2]. Let us further mention that we can also set up $\sigma_L^{\mathrm{T}}\sigma_R$ directly in the thermodynamic limit by defining it in a translation-invariant manner as an MPO without periodic boundary conditions [144]. Using MPS techniques [104, 145], we can subsequently calculate excited states at fixed momenta for this MPO. This procedure gives us access to the low-lying entanglement spectra at arbitrary momenta due to the infinite size of the system. This comes with the consequence of losing the ability to use counting properties for edge spectra in this case, which rely on a discrete structure of momentum space. Again, we use this technique in the analysis performed in publication [P1].

Rényi Entropies

We can also use the bulk-boundary formula for the reduced density matrix ρ_L to access Rényi entropies.

$$S_\alpha(\rho_L) = \frac{1}{1-\alpha}\log(\mathrm{Tr}(\rho_L^\alpha)). \tag{4.40}$$

We can again use the formula for the reduced density matrix of eq. (4.35) to express Rényi-entropies. Let us consider the second Rényi-entropy for the bipartition of a cylinder

$$\begin{aligned} S_2(\rho_L) &= -\log(\mathrm{Tr}(\rho_L^2)) \\ &= -\log(\mathrm{Tr}(\sigma_L^{\mathrm{T}}\sigma_R\sigma_L^{\mathrm{T}}\sigma_R)). \end{aligned} \tag{4.41}$$

We can numerically evaluate this formula by using the approximation from Eq. (4.38), allowing us to represent the σ-matrices using our CTMRG environment tensors [83]. This allows us to express the trace in the equation for the second-Rényi entropy as

$\mathrm{Tr}(\sigma_L^{\mathrm{T}}\sigma_R\sigma_L^{\mathrm{T}}\sigma_R) =$

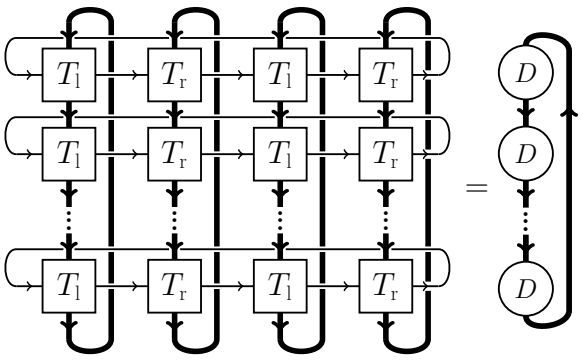

$=$, (4.42)

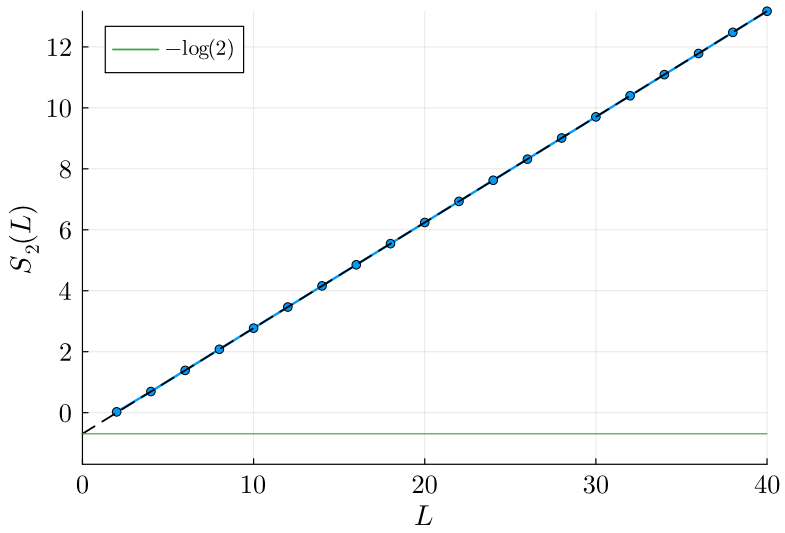

Figure 4.7.: Scaling of the second Rényi entropy for a bipartition on a cylinder, as a function of the cylinder circumference. We can identify the topological entanglement entropy by scaling the cylinder circumference to zero.

where the trace is implemented by connecting virtual indices in the horizontal direction. The second equality in Eq. (4.42) uses an eigendecomposition of the operator

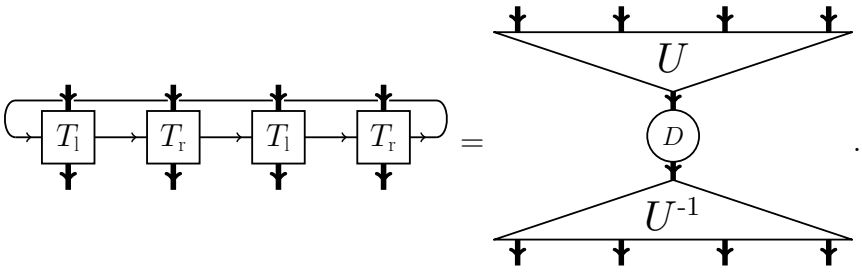

. (4.43)

The form of Eq. (4.42) is convenient to evaluate Eq. (4.41) for situations of large and variable cylinder circumferences L[18] [83], as it only requires us to evaluate powers of a diagonal matrix. Note that at large cylinder circumferences, the trace is dominated by the largest magnitude eigenvalues, such that is sufficient to only consider these.

This construction of the Rényi-entropies can be useful in the calculation of universal topological corrections, referred to as *topological entanglement entropy* [146, 147], to these Rényi-entropies. This topological entanglement entropy γ had been introduced as a universal correction to the non-universal boundary law scaling of the von Neumann entanglement entropy $S(L) \sim \alpha L - \gamma$, but it has been shown to be identical for all Rényi-

[18] In practical calculations, we might have a representation of ρ_L which is not normalized. We can easily account for this by dividing ρ_L by a factor of $\mathrm{Tr}(\rho_L)^2 = \mathrm{Tr}(\sigma_L^\mathrm{T}\sigma_R)^2$ in this eq. (4.41).

entropies for non-chiral states [148]. As an example, we show in Fig. 4.7 the evaluation of the second Rényi entropy for a numerically optimized ground state of the toric code Hamiltonian. Fitting the boundary law scaling to the second Rényi entropy allows us to estimate the topological entanglement entropy[19] [83].

Comment on Numerical Approximations and Refinement

When we employ the above schemes for numerical calculations, it is important to realize that this will involve numerical approximations, which we will briefly discuss here[20]. The central approximation in the evaluation of the entanglement quantities discussed above is the representations of σ_L and σ_R with the use of the CTMRG tensors. Since we use finite bond dimension approximations of these objects, a careful convergence check in the bond dimension used for the approximation is advisable. We further note that an additional approximation can stem from using the T-tensors, calculated using the CTMRG algorithm. This algorithm is performed on a planar geometry, and its resulting tensors T-tensors are then used on a cylindrical geometry.

[19] We note that this procedure can be difficult, as a typically small correction needs to be fitted from linear behaviour at large cylinder circumferences, which can lead to inaccuracies.

[20] Usually in numerical calculations, tensor product states are themselves approximations of ground-states of Hamiltonians. Here we only discuss the approximations for the entanglement quantities of a given tensor product state.

Part II.

RESULTS AND PUBLICATIONS

CHAPTER 5

Fractional quantum Hall states with variational projected entangled-pair states: A study of the bosonic Harper-Hofstadter model

Authors:	**Erik Lennart Weerda**, Matteo Rizzi
Year:	2024
Journal:	Physical Review B (Letter)
Volume / Issue:	109/24
DOI:	10.1103/PhysRevB.109.L241117

5.1 Summary and Context

In this publication, we investigate the Harper-Hofstadter model, describing mobile bosonic particles in an external magnetic field. The model is relevant to current cold atom experiments [149, 150, 151, 152, 153], setting out to realize and study fractional quantum Hall states [8, 95, 96].

The investigation of the model has been performed using infinite projected entangled-pair states, which are alternatively referred to as infinite tensor product states and are the subject of Part I of this thesis. With this numerical approach, we studied the phase diagram of the Harper-Hofstadter model for multiple values of the magnetic flux as a function of the chemical potential. Several regions of the phase diagram realizing fractional Hall states were identified. For these states, we studied the bulk correlation functions, cf. Sec. 4.3.1, and their edge spectrum via the entanglement spectrum [142,

143]. For this, we employed the bulk-boundary correspondence [141] of the tensor product states, which we discuss in Sec. 4.3.2. We find a chiral edge spectrum, which upon discretization of the momenta yields the degeneracy counting according to the partition of integers expected for the Laughlin state [8].

This publication's impact in the context of this dissertation can be viewed as twofold. Firstly, it establishes that with the help of variational optimization, infinite tensor product states can be used to study chiral topological states of matter in realistic models. This task had proven to be prohibitively difficult using conventional optimization schemes using Trotterized imaginary time evolution. In addition, due to no-go theorems [91, 90] in related situations, the applicability of the tensor product states was in question, cf. Sec. 3.2.4, and only specially constructed quasi-parent Hamiltonians [154, 97] of such chiral topological states had been studied using the tensor product states. Secondly, as the tensor product states provide a unique perspective from the thermodynamic limit, the results from this publication shed light on the stability of the fractional Hall states when finite-size effects are removed. This is relevant for the prospects of realizing such states in larger, next-generation cold atom experiments. Consequently, the publication contributes a demonstration of the scope of applicability of the tensor product states for chiral topological states and new insights into the phase diagram of the Harper-Hofstadter model in the thermodynamic limit.

5.2 Authors Contribution

E. L. Weerda carried out the research for this project with supervision from M. Rizzi. He performed all calculations, analysed the results, and wrote the manuscript with feedback from M. Rizzi.

CHAPTER 6

Triangular lattice models of the Kalmeyer-Laughlin spin liquid from coupled wires

Authors:	Tingyu Gao, Niklas Tausendpfund, **Erik Lennart Weerda**, Matteo Rizzi and David F. Mross
Year:	2025
Journal:	Arxiv Preprint
Volume / Issue:	arXiv:2502.13223
DOI:	10.48550/arXiv.2502.13223

6.1 Summary and Context

In this preprint, we construct a local spin model, such that it hosts a Kalmayer-Laughlin chiral spin liquid [155] as its ground state. Local models of this kind are a crucial first step towards the realization of such phases.

The construction of the local models works by coupling one-dimensional spin-chains in the gapless phase, such that left- and right-moving modes on adjacent chains gap out and isolated directional modes remain on the boundary. This construction yields a spin model on a triangular lattice, which we subsequently study for a set of parameters that have not been fine-tuned. We perform numerical analysis of the resulting model on various quasi-one-dimensional geometries (thin cylinders) using matrix product state methods [104, 156]. These investigations reveal properties such as, e.g., spin pumping upon flux insertion through the cylinder and entanglement spectrum signatures that hint at the presence of the desired chiral spin liquid. In addition, we use the infinite tensor product

states, cf. Part I of this thesis, to investigate the model in the thermodynamic limit of a truly two-dimensional setting. We find a state with vanishing local magnetization as the ground state of the ansatz used. We employ the bulk boundary correspondence of the tensor product states, discussed in Sec. 4.3.2, to investigate the boundary spectrum of the states via the entanglement spectrum [142, 143]. We can identify the counting of the degeneracy of the momentum modes according to the partition of integers, expected for a Kalmayer-Laughlin chiral spin liquid.

In the context of this thesis, this preprint presents an investigation of exotic quantum matter using the infinite tensor product states. The lattice model at hand required careful ground state search using variational optimization and advanced analysis using the entanglement spectrum.

6.2 Authors Contribution

E. L. Weerda carried out the numerical analysis of the lattice model in the two-dimensional setting using the infinite tensor product states. He further contributed to the discussion about the rest of the numerical analysis. He also wrote the section of the manuscript describing the two-dimensional analysis of the model using tensor product states. He was involved in discussions on the clarity of the writing of the remaining sections of the manuscript.

6.3 Odds and Ends

In addition to what is reported in the preprint above, we have since performed additional calculations on this model. In this section, we detail the results of these investigations.

First, we have optimized the infinite tensor product state using an additional ansatz. It is identical to the one we illustrate in Fig. 14 of the preprint; however, we drop the relation between the local tensors A and B, which is shown on the right of Fig. 14. Using this, less restrained ansatz, we have identified an additional low-energy phase of the model. This additional phase has finite local magnetizations that are anti-ferromagnetically aligned between tensors A and B, and the magnetizations lie in the XY-plane. We refer to this phase as the XY-phase. We can compare the energies of this XY-phase and the desired chiral spin liquid in Fig. 6.1a.

Let us comment on these numerical results, focusing first on the results for the XY-

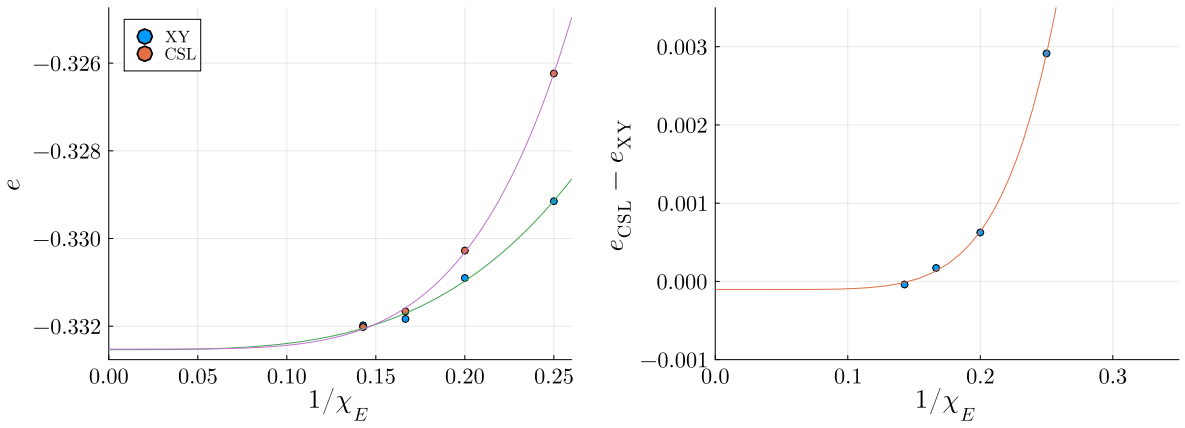

(a) (b)

Figure 6.1.: (a) Energy density for the chiral spin liquid and the XY-phase for different bond dimensions. The solid lines correspond to a fit of $f(\chi_B) = c_0 + c_1(\frac{1}{\chi_B})^{c_2}$ to the data and should be treated as a guide to the eye. (b) Difference in the energy density of the chiral spin liquid and the XY-phase. We show again a fit of the previous form as a guide to the eye.

phase. These numerical results were obtained using gradient-based optimization using the full projectors. We first optimized up to a gradient of $||\nabla E|| < 10^{-4}$ using environment bond dimensions $\chi_E = (80, 120, 140, 196)$ for the optimization of the local bond dimensions $\chi_B = (4, 5, 6, 7)$ and evaluated the energy using environment bond dimensions $\chi_E = (120, 150, 200, 230)$. After the gradient threshold above was reached, we continued with the optimization until terminating the optimization at states with corresponding gradient norm $||\nabla E|| = (4.28 \times 10^{-5}, 5.32 \times 10^{-5}, 8.28 \times 10^{-5}, 1.33 \times 10^{-4})$.

Next, we give some details on the numerical results for the chiral spin liquid phase. The gradient-based numerical optimization of states in this phase is particularly challenging due to the unphysical tails in the correlations that are, e.g., described in our publication [P1]. This means that a very large number (~ 200) of CTMRG iterations are necessary to converge the CTMRG environments, which leads to a substantial computational time necessary for every optimization step ($\sim 24h$ at $\chi_B = 7$). We again performed the optimization, as we did for the XY-phase, using full projectors. We have used environment bond dimensions $\chi_E = (120, 150, 160, 142)$ during the optimization for bond dimensions $\chi_B = (4, 5, 6, 7)$. The reason we choose a smaller environment bond dimension for $\chi_B = 7$ is to avoid unnecessarily time-consuming optimization steps. However, to be sure of the energy values, we choose the environment bond dimensions $\chi_E = (150, 180, 220, 230)$ to evaluate the energy expectation values of the last states

of the optimization. For bond dimension $\chi_B = 4$ and $\chi_B = 5$, we have reached the threashold of $||\nabla E|| < 10^{-4}$, while for $\chi_B = 6$ and $\chi_B = 7$ we have not reached this threashold, suggesting that these states are less well converged than their counterparts in the XY-phase. We have then continued with the optimization until terminating with states of gradient norms $||\nabla E|| = (3.58 \times 10^{-5}, 4.82 \times 10^{-5}, 1.27 \times 10^{-4}, 3.97 \times 10^{-4})$.

From these results, we find a very close competition between the energies of the chiral spin liquid phase and the XY phase. Due to this extremely close competition and the fact that the energy values of both the chiral spin liquid for $\chi_B = 6$ and $\chi_B = 7$ are likely to change in the 4'th or 5'th significant digit upon further optimization, we can not definitively conclude that either of the two phases is the ground state of the model. However, let us note that it can be argued that the general trend of a decreasing energy difference with increasing bond dimension suggests that the chiral spin liquid could be the ground state of the model if one removes the constraints of finite bond dimension from the ansatz. The difference as a function of bond dimension is shown in Fig. 6.1b.

Therefore, further optimization using a more efficient algorithm, like the split-CTMRG described in publication [P4], will be performed in the future to obtain more conclusive results. Additionally, we mention that a more careful choice of model parameters could help achieve a larger gap in the energy density of the competing phases.

The data shown and the corresponding optimized tensors can be found in [157].

CHAPTER 7

Bathing in a sea of candidate quantum spin liquids: From the gapless ruby to the gapped maple-leaf lattice

Authors:	Philipp Schmoll*, Jan Naumann*, **Erik Lennart Weerda**, Jens Eisert, Yasir Iqbal
Year:	2025
Journal:	Arxiv Preprint
Volume / Issue:	arXiv:2407.07145
DOI:	10.48550/arXiv.2407.07145

*Both first authors have contributed equally.

7.1 Summary and Context

In this publication, we studied a spin-$\frac{1}{2}$ Heisenberg antiferromagnet on the generalized maple-leaf lattice. By varying the Heisenberg couplings J_g on one of the symmetry inequivalent links of the maple-leaf lattice from zero towards one and beyond, we obtain a parameterized interpolation of the isotropic Heisenberg antiferromagnet from the Ruby ($J_g = 0$) to the maple-leaf lattice ($J_g = 1$). This model of frustrated magnetism has attracted particular interest, as several materials exhibit the maple-leaf lattice structure [158, 159, 160, 161, 162], and theoretical investigations have suggested the possibility of this model hosting a quantum spin liquid as the ground state [163].

This model was studied using the tensor product states introduced in Part I of this thesis. Specifically, a spiral tensor product state ansatz [164] was generalized to this non-Bravais lattice and employed in the numerical calculations. Using this approach, we calculated the ground state energies and average local magnetizations, which were used as a magnetic order parameter. The extrapolation of these quantities, in particular the magnetic order parameter, showed an extensive non-magnetic parameter regime of J_g for the model extending from the Ruby to the maple-leaf point and beyond. For parameter values of $J_g > 1.2$, a magnetically ordered phase and a dimer phase were identified. We studied the stability of the non-magnetic regime to an additional external magnetic field. The presence of a stable plateau at zero magnetization was observed at the maple-leaf point, whereas on the ruby lattice, the external magnetic field immediately leads to a finite magnetization. Furthermore, static structure factors at the Ruby lattice and maple-leaf point were studied. In light of these results, the possibility of different quantum spin liquid results was discussed.

In the context of this thesis, this study represents the application of the infinite tensor product state framework to a highly challenging model of frustrated magnetism. The study offers a complementary perspective from tensor networks in the thermodynamic limit to alternative methods applied to this scenario, like density-matrix renormalization group and neural quantum states [165], pseudo-fermion functional renormalization group [163], and coupled cluster methods [166]. As such, this study contributes to the numerical insights into this highly complex scenario of frustrated magnetism.

7.2 Authors Contribution

E. L. Weerda was involved in generalizing the spiral ansatz used in the publication to non-Bravais lattices and contributed to the computational approach of the structure factor. He proposed computational strategies to achieve smooth convergence across the parameters studied in the publication. He was involved in the discussions of the results.

CHAPTER 8

Variationally optimizing infinite projected entangled-pair states at large bond dimensions: A split corner transfer matrix renormalization group approach

Authors:	Jan Naumann*, **Erik Lennart Weerda***, Jens Eisert, Matteo Rizzi, Philipp Schmoll
Year:	2025
Journal:	Physical Review B
Volume / Issue:	111 / 23
DOI:	10.1103/PhysRevB.111.235116

*Both first authors have contributed equally.

8.1 Summary and Context

The central method used in this thesis is the class of quantum states called the projected entangled pair states, which are alternatively referred to as tensor product states, cf. Part I.

In this work, we propose an alternative method for the contraction of infinite tensor product states. The proposed scheme modifies the well-established corner transfer matrix renormalization group (CTMRG) algorithm [106, 107, 108, 109, 110, 111, 112], which we discuss in Sec. 4.1.1. Our novel approach addresses a key issue in the pursuit of

highly accurate numerical calculations using infinite tensor product states, namely, the unfavorable scaling of the computational cost as a function of bond dimension. The conventional CTMRG algorithm scales as $\mathcal{O}(\chi_B^6 \chi_E^3)$, leading to an overall scaling of $\mathcal{O}(\chi_B^{12})$ under the conventional assumption $\chi_E \sim \chi_B^2$. This scaling eventually prohibits the use of unconstained tensor product states with bond dimension $\chi_B > 8$ for variational optimization, as the computational time required becomes impractical. This presents a limiting factor on the amount of entanglement that can be encoded in variationally optimized tensor product states and hence limits the accuracy that can be achieved with this ansatz class for challenging physical situations. To address this issue, we propose the split-CTMRG algorithm. It reduces the computational scaling of the CTMRG algorithm by defining environment tensors for *bra-* and *ket-* layers of the double layer contraction separately. This reduces the rank of the environment tensors, and consequently leads to a more favorable computational scaling $\mathcal{O}(\chi_B^{10})$, which can be further reduced to $\mathcal{O}(\chi_B^9)$ with additional approximations. We numerically analysed our split CTMRG method, finding that we can preserve the accuracy of the CTMRG algorithm. This is achieved with carefully chosen schemes for the truncation of the environment bond dimension in the split CTMRG algorithm.

Hence, this publication presents a methodological advance for the tensor product states, the central approach used in this thesis. It promises to push the limits of accurate variational ground state investigations using the tensor product states.

8.2 Authors Contribution

E. L. Weerda was one of the two authors who developed the split-CTMRG algorithm. Additionally, he analysed the scaling advantage and devised the benchmarks to assess the accuracy and efficiency of the split-CTMRG algorithm in practice. Further, he wrote the majority of the manuscript.

CHAPTER 9

Efficient optimization and conceptual barriers in variational finite Projected Entangled-Pair States

Authors:	Daniel Alcalde Puente*, **Erik Lennart Weerda***, Konrad Schröder, Matteo Rizzi
Year:	2025
Journal:	Physical Review B
Volume / Issue:	111/19
DOI:	10.1103/PhysRevB.111.195120

*Both first authors have contributed equally.
†This publication has been choosen as an *Editors' Suggestion*.

9.1 Summary and Context

In this publication, we investigate conceptual and methodological aspects of projected entangled-pair states, alternatively referred to as tensor product states, on finite lattices. We discuss the unique advantages and explore several challenging applications of this method.

After the first proposal of the tensor product states [12], the most used flavor of this class of quantum states were the translationally invariant infinite tensor product states [29], for which a plethora of methods were developed, cf. Part I of this thesis, and the scope of applications of this method has steadily grown. In contrast to this, the application of tensor product states to finite lattices has been significantly less explored due to various numerical challenges. However, a sampling-based framework for the tensor

product states on finite lattices has recently shown significant progress towards greater utility of this approach [30, 31, 32, 33]. To add to this progress, in this work we propose the use of a more efficient formulation of the time-dependent variational principle (TDVP) [127, 167, 168, 169, 31] for ground state search in the sampling context. This formulation has been used in the neural quantum state community under the name of *minimum-step stochastic-reconfguration* [170]. Further, we investigate the role of the difficulty of the contraction of samples of finite tensor product states, identifying an entanglement phase transition for random tensor product states and proposing a predictive quantity for the sample contracability of physically relevant tensor product states. In addition to the conceptual results, in this publication, we show the power of this approach for tackling state-of-the-art problems in many-body physics from chiral spin liquids [154] to long-range interacting Rydberg atom arrays [171, 172]. An open-source implementation of the finite tensor product state techniques used in these investigations is provided alongside this publication.

In the context of this thesis, this publication thus presents a methodological contribution to the sampling-based framework for finite tensor product states, complementing advances made in the context of infinite tensor product states. Further, this publication points out the great utility of this finite tensor product state framework for the investigation of states of matter accessible in cold atom experiments, in particular those with long-range interacting Rydberg atom arrays, which is now actively pursued further.

9.2 Authors Contribution

E. L. Weerda initialized the project, motivated by the use of the finite tensor product states for investigations of long-range interacting Rydberg arrays. He contributed to the conceptual development of the computational strategies and the design of the code structure. He was one of the two major contributors to the analysis of the contractibility of both random and physically motivated tensor product states. He was the driving force in the choice of applications and the analysis of the results. Further, he wrote the majority of the manuscript.

CHAPTER 10

Josephson Junction Arrays on the Dice Lattice at Frustration $f = \frac{1}{3}$

10.1 Introduction

Josephson junction arrays (JJAs) have long been an interesting experimental platform for many-body physics [173]. Recent technological advances have made electrically tunable Josephson Junction arrays possible, in which Josephson- and charging energies can be manipulated within a single sample [174, 175, 176, 177, 178], driving renewed interest towards this platform.

In this chapter, we present some of the results of an ongoing study of the physics of these JJAs on a dice lattice geometry. The dice lattice is illustrated in Fig. 10.1a. In addition to this geometry for the JJAs, we consider the presence of a perpendicular magnetic field. We describe this situation using the following model

$$H = -E_J \sum_{\langle i,j \rangle} \cos(\underbrace{\phi_j - \phi_i - A_{ij}}_{\theta_{ij}}) + \frac{1}{2} \sum_i E_C n_i^2. \tag{10.1}$$

The first term describes the Josephson energy, resulting from the gauge-invariant phase difference (GIPD) θ_{ij} between two adjacent superconducting islands. The GIPD is a sum of the phase difference $\phi_j - \phi_i$ on superconducting islands of the JJA, and the integral over the vector potential $A_{ij} = \frac{2\pi}{\Phi_0} \int_{\vec{r_i}}^{\vec{r_j}} \vec{A}(r) d\vec{r}$, where $\Phi_0 = \frac{h}{2e}$ is the flux quantum.

The second term in the Hamiltonian describes the charging energy of the JJAs. Here, we work with the simplest approximation using a purely local repulsive interaction between the charge carriers (Cooper-pairs) on the individual superconducting islands.

We will investigate this model for a magnetic flux through every rhombus of the dice

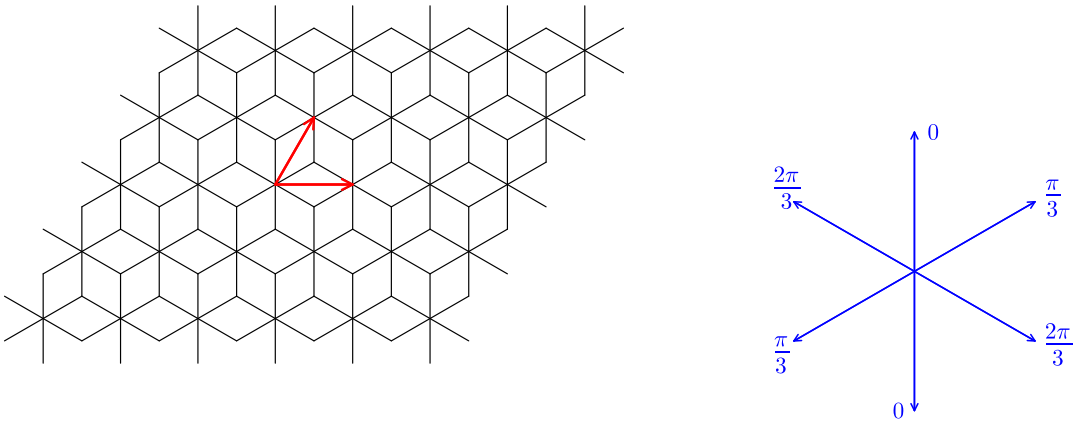

(a) (b)

Figure 10.1.: (a) Illustration of the dice lattice. The unit cell vectors are shown in red. Within every unit cell, we have one site with 6 nearest neighbors (called a *hub*) and two sites with 3 nearest neighbors (called *rims*). (b) Illustration of the gauge choice used in this study to achieve frustration $f = \frac{1}{3}$. The arrows indicate the directionality associated with the gauge integrals for the edges that border every hub. This gauge choice leads to a minimal magnetic unit cell, that is identical to the unit cell without any frustration.

lattice that is precisely one-third of the flux quantum Φ_0. We label this fraction of the flux quantum as the frustration parameter f, which can be expressed as the directed sum over a rhombus of the lattice

$$f = \frac{1}{2\pi} \sum_{\text{rhombus}} A_{ij}. \tag{10.2}$$

The particular gauge choice for the values of A_{ij} which we will use in these investigations and that achieves $f = \frac{1}{3}$, is illustrated in Fig. 10.1b. The dice lattice has attracted substantial interest in the past for the case of frustration $f = \frac{1}{2}$. At this frustration, it hosts completely flat bands for a tight-binding model [179, 180]. This motivated a number of studies on the interaction-dominated phases in related models [181, 182].

The model in Eq. (10.1) was previously analysed in the classical case of $E_C = 0$ (where it is just a frustrated XY-model) by Korshunov [183] for frustration $f = \frac{1}{3}$, and we will describe some of his results in the following. In this context, we say we have a *vortex* in a plaquette of the lattice if the spin configuration rotates by 2π around a plaquette, such that $\sum_{\text{plaquette}} \theta_{ij} = 2\pi(1 - f)$. First, we expect the ground states of

the model to have a vortex density of one vortex per every three rhombi of the dice lattice. Of the states with this vortex density, we can identify the ground states as those vortex configurations in which the rhombi with vortices do not share any edges of the lattice. We give an illustration of examples of such vortex configurations in Fig. 10.5. These vortex configurations are the ground states of the model, as this allows us to choose $\theta_{ij} = \frac{\pi}{3}$ for the edges around the vortices – minimizing the energy on these bonds subject to the vortex restriction. All other terms in the Hamiltonian can be minimized by simply choosing $\theta_{ij} = 0$. In these ground-state vortex configurations, every hexagon of the dice lattice, which is made up of three rhombi, contains exactly one vertex.

These insights about the ground states can be used to derive a few simple consequences [183]. First of all, we can calculate the ground state energy explicitly: As we can account for all edges of the lattice by considering those adjacent to the three fold-connected *rims* of the lattice, and because every *rim* will be adjacent to one vortex, we obtain an energy contribution per *rim* of $e_{\text{rim}} = (2\cos(\frac{\pi}{3}) + \cos(0))E_J = 2E_J$, which leads to a ground state energy per site of $e = e_{\text{UC}}/N_{\text{UC}} = 4E_J/3$, as we have two rims and three sites per unit cell.

Additionally, this explicit construction allows us to relate the different ground states of this model to those of the triangular lattice antiferromagnetic Ising model (TLAIM) [183]. To see this, consider only the 6-fold connected *hubs* of the dice lattice, which form a triangular lattice. We can associate anti-parallel Ising spins to every connection between the *hubs* on this triangular lattice that does not cross a vortex, and parallel Ising spins to those that do[1]. Indeed, we find that by this mapping, the vortex configurations of the ground state are mapped to configurations of the Ising spins on the triangular lattice in which two bonds per triangle are anti-parallel and one is parallel[2]. Thus, the ground states of our model at $E_C = 0$ can be associated with the ground state configurations of this Ising model. This is particularly interesting as the residual, zero temperature entropy of this Ising model is known to be $s_{\text{TLAIM}} \approx 0.323$ [184][3].

Korshunov further analyzed (by another mapping to a solid-on-solid model) that due to the entropic effect of this extensive number of ground state configurations, the free energies of the fluctuations about different ground state configurations are not large enough to lead to the selection of a single vortex pattern at finite temperature due to *order by disorder* [185]. Instead, he predicted the system to stay disordered. However, at the same time, he conjectured that the system would display a finite helicity modulus at low temperatures, which would be destroyed due to the dissociation of half-vortices [183,

[1]It can be helpful to consider Fig. 10.5 again to verify this mapping.
[2]Recall that we have exactly one vortex per hexagon in the ground state configurations.
[3]Note that we have set $k_{\text{B}} = 1$ throughout this chapter.

186] at finite temperature. These half vortices appear as excitations of the ground state configurations and can be located, e.g., at positions of three adjacent rhombi forming a hexagon without any vortex.

Let us note that this is different from the behavior found in unfrustrated XY models. In the unfrustrated case, the important excitations are integer vortices that are confined at low temperature. Their deconfinement is associated with the Berezinskii–Kosterlitz–Thouless (BKT) transition, which destroys the algebraic decay of the phase correlations (quasi-long-range order) and the associated finite helicity modulus.

In JJAs, these transitions from a quasi-long-range ordered state to a disordered state at high temperatures describe the transition from a superconducting to a normal state. In the conventional case, the confinement of integer vortices is associated with $2e$-superconductivity. If, however, we are in a situation where no $2e$-superconductivity is present, e.g., because it is destroyed by domain walls between half vortices, but the half-vortices are confined to pairs such that a finite helicity modulus develops anyway [186], we can refer to this as a $4e$-superconducting state. Such $4e$-superconducting states have long been of interest in several different contexts, from the cuprates to superconducting wire networks [187, 188, 189, 190].

10.2 Thermodynamic Investigation

We begin our discussion by numerically investigating the thermodynamic properties of the model of the Josephson junction arrays, cf. Eq. (10.1), at vanishing charging energy $E_C = 0$. To this end, we will approximate the partition function of the model

$$Z = \sum_j \exp\left(-\beta E_j\right) = \int \mathcal{D}\phi \exp\left(-\beta H(\{\phi\})\right), \tag{10.3}$$

$$\int \mathcal{D}\phi = \prod_i \int_{-\pi}^{\pi} \frac{d\phi_i}{2\pi}, \tag{10.4}$$

as a two-dimensional tensor network. We describe how to construct the tensor network representation of the partition function [191, 192, 193] and mention the computational tools used here in App. B.

We start by computing the free energy density, as a logarithm of the partition function $f = F/N = -\frac{1}{\beta N}\ln(Z)$, which we show in Fig. 10.2a. We find a monotonic decrease of the free energy density towards lower temperatures, without any hints of discontinuous points.

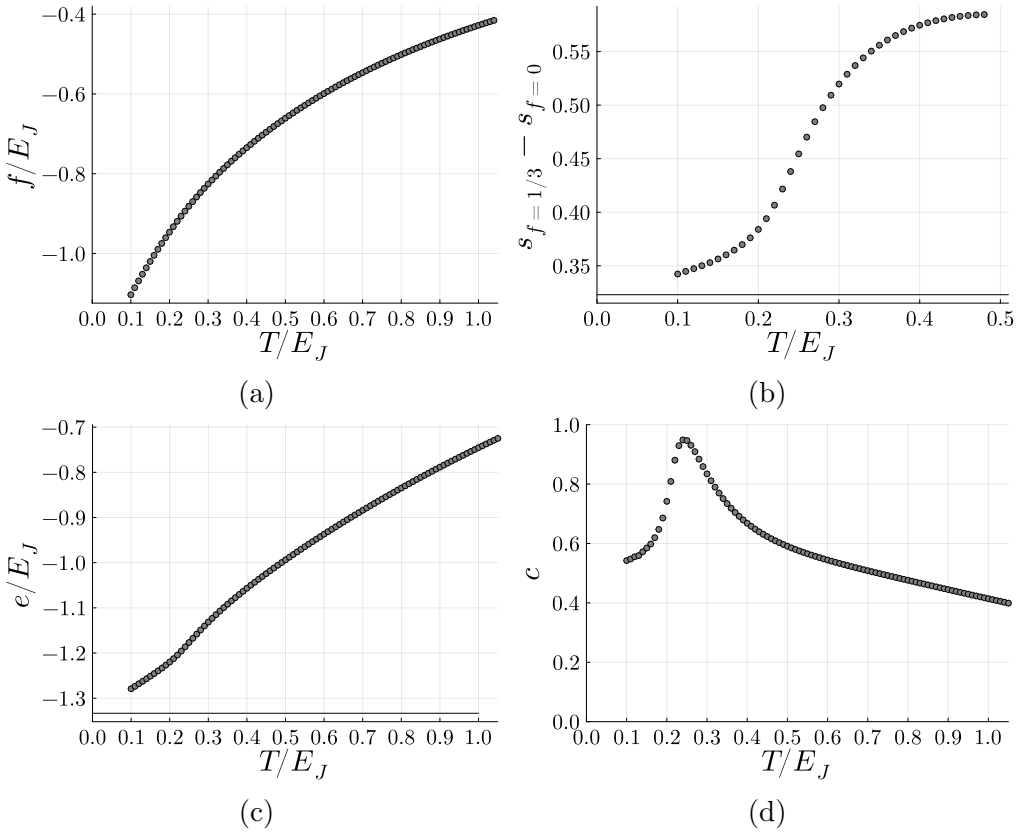

Figure 10.2.: (a) Free energy density as a function of temperature. We find a smooth behaviour without signs of discontinuities. (b) Difference of the entropy density at frustration $f = \frac{1}{3}$ and $f = 0$. We find that this difference tends towards the value of $s_{\mathrm{TLAIM}} \approx 0.323$ at low temperatures. (c) Energy density as a function of temperature. Again, we find a smooth behaviour tending towards the exactly known value at $T = 0$. (d) Specific heat per site as a function of temperature. We find a bump at $T/E_J \sim 0.24$.

The derivative of the free energy density can be used to represent the entropy density

$$s = -\frac{\partial f}{\partial T}. \tag{10.5}$$

Here we are interested in particular in the entropy due to the many degenerate ground state configurations identified by Korshunov [183]. However, in addition to the discrete nature of the different ground-state vortex configurations, the model contains entropy contributions from the continuous nature of the phase variables. We conjecture that at zero temperature, the entropy density at frustration $f = \frac{1}{3}$ is the sum of the contribution from the continous variables and an additional entropy due to the extensive ground state vortex configurations. The contribution due to the continuous variables should be

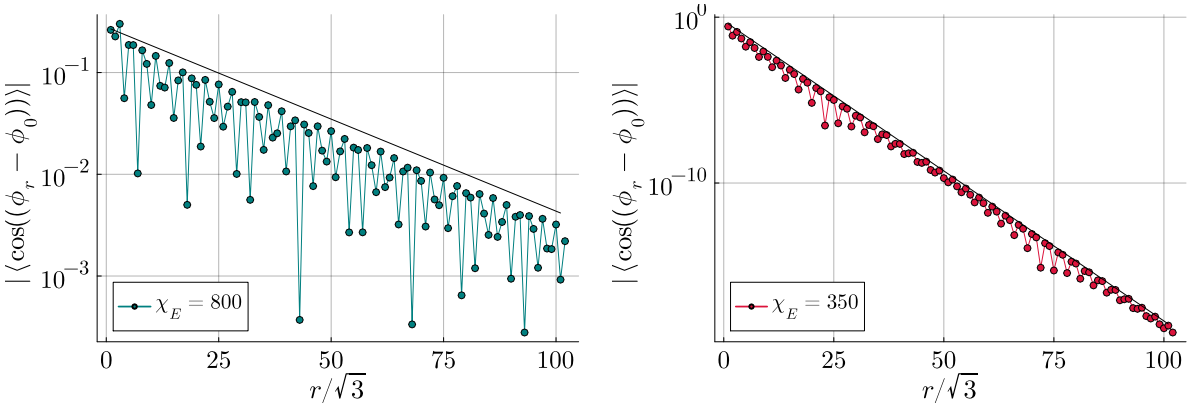

(a) (b)

Figure 10.3.: Correlation function $C(r)$ as a function of distance at $T = 0.17$ (a) and $T = 0.3$ (b). The correlation function is evaluated along the horizontal direction, cf. Fig. 10.1a, on the hubs of the dice lattice. We find exponential decay at both temperatures.

identical to the entropy at $f = 0$ where no additional discrete contribution to the entropy exists. As we discussed in the introduction, these ground state vortex configurations can be identified with the ground states of the triangular lattice antiferromagnetic Ising model [183]. We thus expect the following form of the entropy

$$s_{f=1/3}(T = 0) = s_{\mathrm{TLAIM}}(T = 0) + s_{f=0}(T = 0). \tag{10.6}$$

The data shown in Fig. 10.2b is consistent with this expectation, which can be seen as an example of the complex interplay of discrete and continuous effective variables of frustrated XY-models at low temperatures.

The expectation value of the energy density can be accessed as a function of temperature by taking derivatives of the logarithm of the partition function

$$e = E/N = \frac{1}{NZ}\sum_j E_j e^{-\beta E_j} = -\frac{1}{N}\frac{\partial}{\partial\beta}\ln(Z(\beta)). \tag{10.7}$$

We show the energy density as a function of temperature in Fig. 10.2c, which moves towards the exactly known value $e_0 = -4E_J/3$ at zero temperature [183]. While the numerical values appear to suggest a smooth function for the energy density, it is noticeable that the slope changes slightly around $T/E_J \sim 0.24$.

Such a change of slope should lead to a clearly visible feature in the specific heat per

site

$$c = \frac{\partial e}{\partial T}, \tag{10.8}$$

which we show in Fig. 10.2d. Indeed, we find a bump in the specific heat at around $T/E_J \sim 0.24$. Such a bump in the context of XY-models in two dimensions can signal the presence of a BKT transition. The bump in the specific heat occurs slightly above the critical temperature T_{BKT}, where most of the vortices unbind. In this temperature range above T_{BKT} a large change in the energy of the system occurs as a function of temperature, due to the vortex unbinding [194].

The hallmark of the BKT transition is that, while no spontaneous symmetry breaking can occur at the critical point due to the Mermin-Wagner theorem [195], correlation functions decay algebraically at temperatures below the transition, signalling so-called *quasi-long-range order* [194]. To investigate this, we compute the correlation functions[4]

$$C(r) = \langle \cos(\phi_r - \phi_0) \rangle \tag{10.9}$$

of our model for temperatures above and below the bump in the specific heat. In Fig. 10.3, we show the correlation functions for $T/E_J = 0.17$ and $T/E_J = 0.3$. Both of these functions show an exponential decay as a function of distance, indicating a non-conventional behaviour.

We can, however, identify an algebraic decay when we investigate the correlation functions of two times the phase difference as a function of distance

$$C_2(r) = \langle \cos(2(\phi_r - \phi_0)) \rangle. \tag{10.10}$$

In Fig. 10.4, we show the decay of $C_2(r)$ again both for for $T/E_J = 0.17$ and $T/E_J = 0.3$. We find that while $C_2(r)$ still decays exponentially at $T/E_J = 0.3$ it decays algebraically at $T/E_J = 0.17$. This can be concluded from the data shown in Fig. 10.4a by noting that the increase of the relevant approximation parameter χ_E — the environment bond dimension — leads to algebraic behaviour on larger scales.

Let us stress the fact that an algebraic decay of $C_2(r)$ below a BKT-transition is by itself not special, and would indeed be present in a model without a magnetic field at $f = 0$ as well. What is special is that at the same temperature, the simple correlation function $C(r)$ decays exponentially as a function of distance. Let us further note that

[4] We note that in the numerical computation we performed, the disconnected part of the correlation functions vanishes by construction. Hence, the above correlation functions are equal to the connected correlation functions.

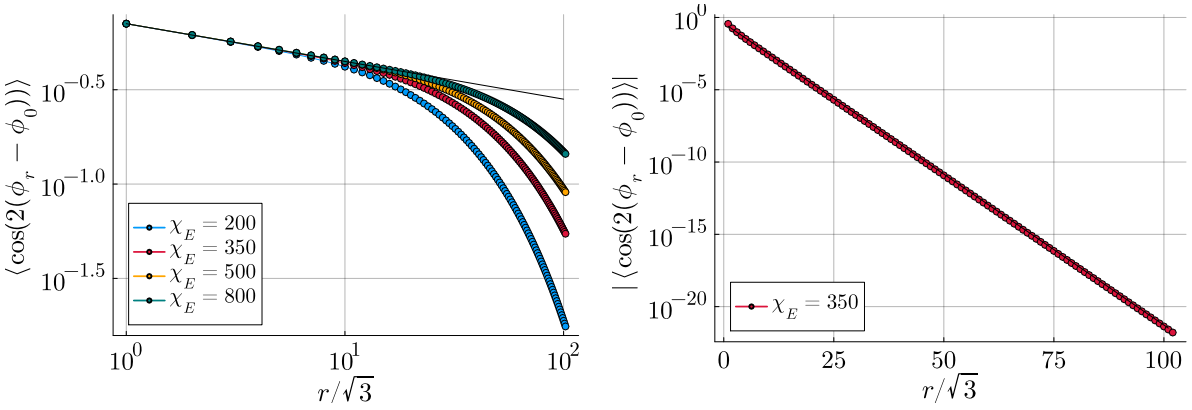

Figure 10.4.: Correlation function $C_2(r)$ as a function of distance at $T = 0.17$ (a) and $T = 0.3$ (b). The correlation function is evaluated along the horizontal direction, cf. Fig. 10.1a, on the hubs of the dice lattice. We find exponential decay at $T = 0.3$, while at $T = 0.17$ we find an algebraic decay. We identify the algebraic decay by increasing the environment bond dimension, which increases the distance on which the decay remains algebraic.

the algebraic decay of $C_2(r)$ is consistent with the conclusion of Korshunov that at low temperatures, a finite helicity modulus will develop. These results thus show that the quasi-long-range phase coherence of a $2e$-superconductor, namely $C(r)$, is not present in the state, while the $4e$-phase coherence is.

Lastly, we mention that the results obtained here suggest a critical temperature of $0.17 < T_{\mathrm{BKT}} < 0.24$, which is consistent with the finding of Fazio and Cataudella [196] of $T_{\mathrm{BKT}} \sim 0.2$ using Monte-Carlo techniques. A precise determination of the critical temperature requires an extensive scaling analysis, cf. [191], and is left for future work on this project.

10.3 Influence of Finite E_C

After numerically studying the behaviour of the model for the JJAs, cf. Eq. (10.1), at vanishing E_C but at finite temperature T, we now turn to an investigation of the behaviour of the model at zero temperature but finite charging energy.

While the model at $E_C = 0$ can be considered as a purely classical model, cf. Sec. 10.2, in the presence of a finite charging energy, this is no longer the case. For the quantum mechanical treatment, we represent the model in the *charge basis*, in which the operator

$\hat{n}_i$ takes on the diagonal form

$$\hat{n}_i = \begin{pmatrix} \ddots & & & & & & & \\ & -2 & & & & & & \\ & & -1 & & & & & \\ & & & 0 & & & & \\ & & & & 1 & & & \\ & & & & & -2 & & \\ & & & & & & \ddots & \end{pmatrix}. \tag{10.11}$$

This operator counts the number of charges on a superconducting island relative to a mean value.

From the first Josephson relation, we can derive that in the charge basis, the exponential of the phase operator takes the form

$$e^{i\hat{\phi}_i} = \begin{pmatrix} \ddots & & & & & & & \\ & 0 & 1 & & & & & \\ & & 0 & 1 & & & & \\ & & & 0 & 1 & & & \\ & & & & 0 & 1 & & \\ & & & & & 0 & & \\ & & & & & & \ddots & \end{pmatrix}, \tag{10.12}$$

from which we can construct the first term of the Hamiltonian as

$$\cos(\hat{\phi}_k - \hat{\phi}_j - A_{jk}) = \frac{1}{2}(e^{iA_{jk}} e^{i\hat{\phi}_k} e^{-i\hat{\phi}_j} + e^{-iA_{jk}} e^{i\hat{\phi}_j} e^{-i\hat{\phi}_k}). \tag{10.13}$$

This gives us the commutators as $[\hat{n}_i, e^{i\hat{\phi}_i}] = -e^{i\hat{\phi}_i}$, and somewhat non-rigorously[5] allows us to identify the number and phases as canonically conjugate variables $[\hat{n}_i, \hat{\phi}_j] = i\delta_{ij}$.

We will investigate this situation using the tensor product states, which we introduced in Part I of this thesis. We use a square lattice tensor product state ansatz for the quantum state, as illustrated in Fig. 10.6. The unit cell is chosen to be of size 3×6. This unit cell size, in the choice of gauge shown in Fig. 10.1b, allows for periodic phase configurations that realize both the *stripe*- as well as the *honeycomb*- vortex pattern

[5]Ignoring that $\hat{\phi}$ is not well defined as ϕ is only defined modulo 2π. Hence, rigorously, we can only define periodic functions of $\hat{\phi}$.

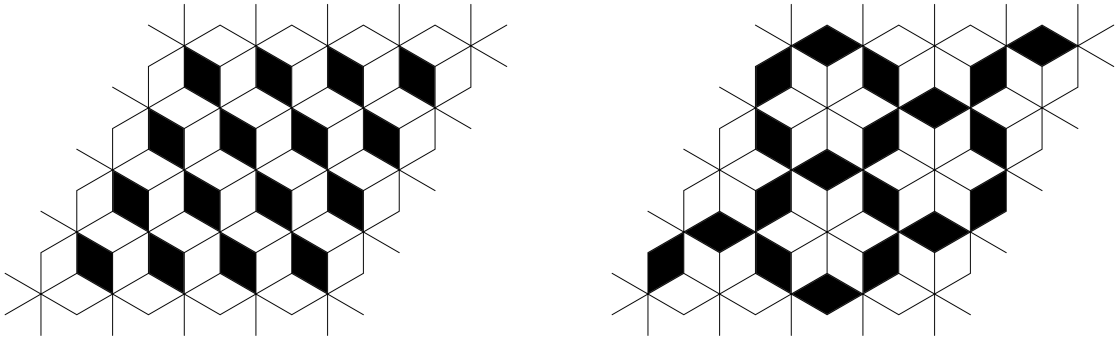

(a) (b)

Figure 10.5.: Illustration of the two different periodic vortex configurations which we focus on in this section. The presence of a vortex is illustrated with a black rhombus, while the white rhombi do not contain a vortex. a) Shows the *stripe*-vortex pattern, while b) illustrates the *honeycomb*-vortex pattern.

that were identified as periodic ground state vortex-configurations at $E_C = 0$ [183] and are illustrated in Fig. 10.5. Whenever we are performing numerical computations, we will need to truncate to finite-dimensional local Hilbert spaces in the charge basis. This truncation needs to be chosen differently as a function of E_C, to truncate only local charge configurations that are qualitatively irrelevant for the ground states.

10.3.1 Small E_C

From the form of the operators $\hat{n}_i$, it is clear that the presence of a finite charging energy will energetically disfavor local charge configurations that differ from the mean charge occupation per site. Hence, for larger E_C the ground state of the model for the JJAs will include a smaller number of local charge fluctuations. At the same time, from the non-rigorous commutation relation $[\hat{n}_i, \hat{\phi}_j] = i\delta_{ij}$ is becomes clear that this suppression of local charge fluctuation will lead to phase fluctuations about the classical phase value ϕ_i on every site.

We expect that this effect will lift the degeneracy of the multitude of classical ground states at $E_C = 0$ [183] and select those classical states with the most favorable energy landscape around the classical state, due to the phase fluctuations.

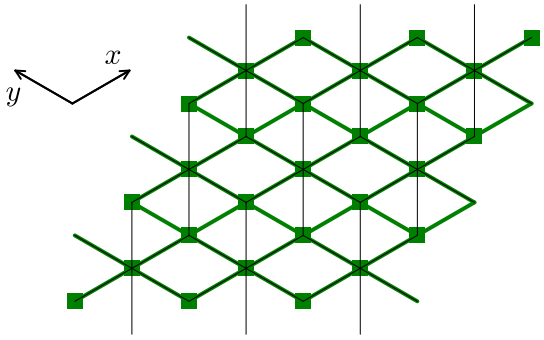

Figure 10.6.: Illustration of the square lattice TPS ansatz used on the dice lattice. While the underlying dice lattice is shown in back, the TPS tensors are shown in green. We only highlight the connectivity of the virtual bonds and suppress the leg corresponding to the local Hilbert space on every site. Notice that due to the different connectivity of hubs and rims on the dice lattice, some interactions between neighbors on the dice lattice become next-nearest neighbor interactions for the square lattice ansatz.

Zero-Point Energy

The lifting of the ground-state degeneracy at small E_C can be studied by considering the zero-point energy due to the quantum fluctuations required by the commutation relation $[\hat{n}_i, \hat{\phi}_j] = i\delta_{ij}$.

By expanding the phase operators $\hat{\phi} = \phi_0 + \hat{\varphi}$ about the classical minima at $E_C = 0$, we obtain to quadratic order

$$H \approx E_0 - \frac{E_J}{2} \sum_{\langle i,j \rangle} \cos(\theta_{ij}^0)(\hat{\varphi}_j - \hat{\varphi}_i)^2 + \frac{E_C}{2} \sum_i \hat{n}_i^2, \tag{10.14}$$

where we denote the classical ground state value of the GIPD as θ_{ij}^0. We recall from the introduction of this chapter that this value θ_{ij}^0 is either $\frac{\pi}{3}$ if the edge in question is adjacent to a vortex, and zero otherwise [183]. The sum of the resulting linear terms in the expansion vanishes[6] as is expected for an expansion about a classical ground state. Fourier transforming the variables on each sublattice results in the form

$$H \approx E_0 - \frac{E_J}{2} \sum_{k,\alpha,\beta} \hat{\varphi}_{-k,\alpha} D(k)_{\alpha\beta} \hat{\varphi}_{k,\beta} + \frac{E_C}{2} \sum_{k,\alpha} \hat{n}_{-k,\alpha} \hat{n}_{k,\alpha}, \tag{10.15}$$

[6]For every vortex adjacent to a site, we get two non-zero contributions to linear order for that site. These two linear contributions are $\sin(\frac{\pi}{3})$ and $\sin(-\frac{\pi}{3}) = -\sin(\frac{\pi}{3})$ as the GIPD around the vortex are $\frac{\pi}{3}$ with a fixed directionality.

with α and β being sublattice indices. By diagonalizing the matrix $D(k)$, which is already diagonal in k, in the sublattice space we obtain

$$H \approx E_0 - \frac{E_J}{2} \sum_{k,b} \hat{\varphi}_{-k,b} \Gamma(k)_{bb} \hat{\varphi}_{k,b} + \frac{E_C}{2} \sum_{k,b} \hat{n}_{-k,b} \hat{n}_{k,b}, \tag{10.16}$$

with b now labeling the bands of the energy dispersion. This can be recast into a form of decoupled harmonic oscillators by introducing

$$\hat{X}^1_{k,b} = \frac{\hat{\varphi}_{k,b} + \hat{\varphi}_{-k,b}}{\sqrt{2}}, \quad \hat{X}^2_{k,b} = \frac{\hat{\varphi}_{k,b} - \hat{\varphi}_{-k,b}}{i\sqrt{2}}, \quad \hat{P}^1_{k,b} = \frac{\hat{n}_{k,b} + \hat{n}_{-k,b}}{\sqrt{2}}, \quad \hat{P}^2_{k,b} = \frac{\hat{n}_{k,b} - \hat{n}_{-k,b}}{i\sqrt{2}} \tag{10.17}$$

such that after identifying

$$m = \frac{2}{E_C}, \quad \omega^2_{k,b} = \frac{-E_J E_C \Gamma(k)_{bb}}{4} \tag{10.18}$$

we obtain

$$H \approx E_0 + \sum_{k,b,\sigma} \frac{1}{2m} (\hat{P}^\sigma_{k,b})^2 + \frac{1}{2} m \omega^2_{k,b} (\hat{X}^\sigma_{k,b})^2. \tag{10.19}$$

We can define ladder operators for every k, b, σ:

$$\hat{a}_{k,b,\sigma} = \sqrt{\frac{m\omega_{k,b}}{2}} \hat{X}^\sigma_{k,b} + i \sqrt{\frac{1}{2m\omega_{k,b}}} \hat{P}^\sigma_{k,b}, \tag{10.20}$$

$$\hat{a}^\dagger_{k,b,\sigma} = \sqrt{\frac{m\omega_{k,b}}{2}} \hat{X}^\sigma_{k,b} - i \sqrt{\frac{1}{2m\omega_{k,b}}} \hat{P}^\sigma_{k,b}, \tag{10.21}$$

to get the desired form

$$H \approx E_0 + \underbrace{\sum_{k,b,\sigma} \omega_{k,b} (\hat{a}^\dagger_{k,b,\sigma} \hat{a}_{k,b,\sigma} + \frac{1}{2})}_{=:\delta E}. \tag{10.22}$$

By moving to an integral over the Brillouin zone and accounting for the size and number of sites per unit cell, we can evaluate the zero-point energy correction per site as

$$\frac{\delta E}{N} = \frac{\delta E}{A} \frac{V_{\mathrm{UC}}}{N_{\mathrm{UC}}} = \sum_{b,\sigma} \frac{1}{(2\pi)^2} \int_{\mathrm{BZ}} d^2k \, \frac{\sqrt{-E_C E_J \Gamma_{bb}(k)}}{4}. \tag{10.23}$$

For the case of the *stripe ordered* vortex pattern, we can define a small unit cell size,

identical to the one shown in Fig. 10.1a with the unit cell vectors $\vec{a}_1 = \begin{pmatrix} \sqrt{3} \\ 0 \end{pmatrix}$ and $\vec{a}_2 = \begin{pmatrix} \sqrt{3}/2 \\ 3/2 \end{pmatrix}$. This allows us to find the three bands of the dispersion, and the following expressions:

$$\Gamma(k)_{11} = -2 \tag{10.24}$$

$$\Gamma(k)_{22} = -3 + \sqrt{(1 + 2\tau(k)\tau^*(k)} \tag{10.25}$$

$$\Gamma(k)_{33} = -3 - \sqrt{(1 + 2\tau(k)\tau^*(k)} \tag{10.26}$$

with

$$\tau(k) = \frac{1}{2}(e^{ik_y} + e^{i(\frac{\sqrt{3}}{2}k_x - \frac{1}{2}ky)}) + e^{-i(\frac{\sqrt{3}}{2}k_x + \frac{1}{2}ky)}. \tag{10.27}$$

By performing the integral over the Brillouin zone we hence obtain a energy per site for the *stripe ordered* vortex pattern

$$e_{\text{striped}} = e_0 + \frac{1.77878}{2}\sqrt{E_C E_J}, \tag{10.28}$$

which we show in addition to the expectation values obtained with the tensor product states in Fig. 10.7a.

We find a consistent behaviour at small E_C/E_J, with the energies from the tensor product states being slightly lower. This is to be expected, as these states do not presuppose a classical ground state. The tensor product state simulations have been performed with a local Hilbert space dimension $d = 37$ and using bond dimension[7] $\chi_E = 3$.

We can also perform the same analysis for the *honeycomb*-vortex pattern. This results in

$$e_{\text{honeycomb}} = e_0 + \frac{1.77445}{2}\sqrt{E_C E_J}, \tag{10.29}$$

which leads us to conclude that the *honeycomb*-vortex pattern is slightly preferred energetically by the zero-point quantum fluctuations.

Using the tensor product states, we can target different quantum states that share the phase configurations of different periodic classical ground states[8]. These are either the

[7] This small bond dimension can be justified by noting that at small E_C/E_J, the system is very little entangled as it will be in the form of a classical ground state, dressed with small quantum fluctuations.

[8] We can choose different seeds for the optimization to find the different classical ground states. Alternatively, we can apply local phase-rotations $R_j(\theta) = e^{i\theta\hat{n}_j}$ to switch between states of different local phase configurations.

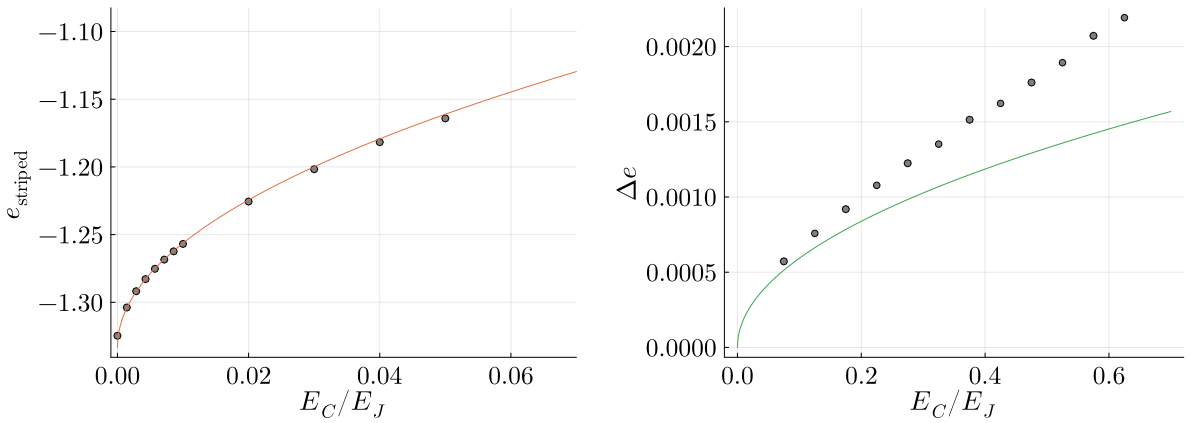

Figure 10.7.: (a) We show the energy density of the model for the JJAs based on the zero-point energy analysis (orange line) for the *stripe* ordered vortex configuration. In addition, we show energy values obtained for this configuration from the tensor product states. We find a good agreement between the tensor product states and the zero-point energy results at small E_C/E_J. (b) Energy difference Δe between periodic ground states corresponding to the honeycomb- and striped vortex patterns. We show both the result from the comparison of the zero-point energies (green line), expected to be accurate at small E_C/E_J, as well as the results from the TPS (grey dots). We find that with increasing E_C/E_J, the honeycomb pattern becomes more energetically favored. The TPS calculations were done with local Hilbert space dimension $d = 19$ and bond dimension $\chi_B = 4$.

phase configurations corresponding to the *striped* or *honeycomb* vortex configuration. This allows us to compare their energies at larger values of E_C/E_J, where the results from the zero-point energy calculations might no longer be accurate. The result is shown in Fig. 10.7b. Indeed, we also find a small energy splitting between the classical configurations, which increases as a function of E_C. The periodic quantum states, with the lowest energy in this comparison, again correspond to the *honeycomb* vortex pattern, also in the range of larger values of E_C/E_J. From this, we conclude that at small E_C/E_J the honeycomb vortex lattice is a ground state candidate. More importantly, we find that the scale of the energy splitting between the different ground states is quite small $\Delta e/E_J \sim 10^{-3} E_C/E_J$.

10.3.2 Large E_C

If we continue to increase the value of E_C, we expect to find a critical value of E_C^{crit}/E_J at which we enter a Mott phase of the charge carriers, in which the phase configuration

becomes completely disordered. To estimate this critical charging energy, we again employ the tensor product states. As an order parameter for the Mott transition, we define the average expectation value of the operator $e^{i\hat{\phi}_i}$ throughout the unit cell, and similarly define the average variance throughout the unit cell as

$$\langle e^{i\hat{\phi}}\rangle_{\mathrm{UC}} = \frac{1}{n_{\mathrm{UC}}} \sum_{i\in\text{unit cell}} |\langle e^{i\hat{\phi}_i}\rangle|, \quad \langle \Delta n\rangle_{\mathrm{UC}} = \frac{1}{n_{\mathrm{UC}}} \sum_{i\in\text{unit cell}} \sqrt{\langle n_i^2\rangle - \langle n_i\rangle^2}. \tag{10.30}$$

We show these quantities as a function of E_C/E_J in Fig. 10.8. We find a kink in the average variance at roughly the same value of E_C/E_J at which $\langle e^{i\hat{\phi}}\rangle_{\mathrm{UC}}$ vanishes. We hence estimate a critical charging energy for the Mott transition $E_C^{\mathrm{crit}}/E_J = 2.57 \pm 0.02$.

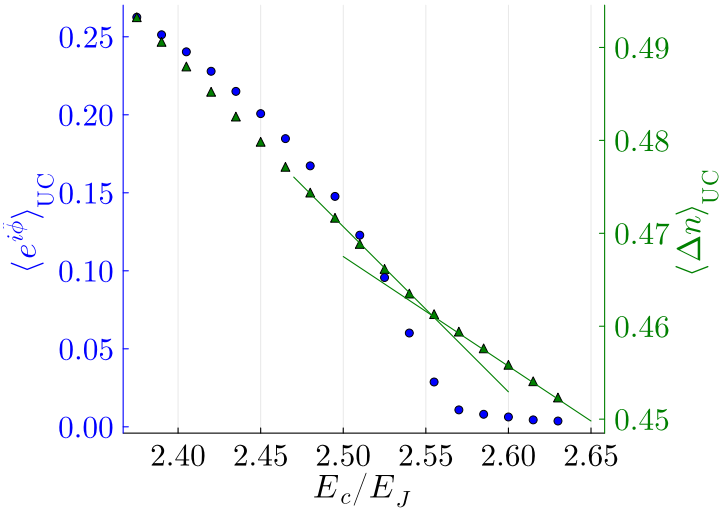

Figure 10.8.: Average variance and order parameter throughout the unit cell. We find that $\langle e^{i\hat{\phi}}\rangle_{\mathrm{UC}}$ vanishes at the same point that $\langle \Delta n\rangle_{\mathrm{UC}}$ has a kink, indicating a transition to a Mott phase. The solid lines serve as a guide to the eye. The computations were performed using bond dimension $\chi_B = 4$ and local Hilbert space dimension $d = 9$.

10.3.3 A Discussion on the Possible Phase Diagram

We conclude this chapter with a summary and a few conjectural remarks about the nature of the phase diagram. At $E_C = 0$ and finite temperature, we have verified the phase structure proposed by Korshunov. We identified a quasi-long-range ordered phase characterized by an algebraic decay of $C_2(r)$ and exponential decay of $C(r)$ below the BKT-transition, indicating a $4e$-superconductor.

At $T = 0$ we have found that quantum phase-fluctuations induced by finite E_C favor the periodic *honeycomb*-pattern over the *striped*-pattern of vortices. However, with a

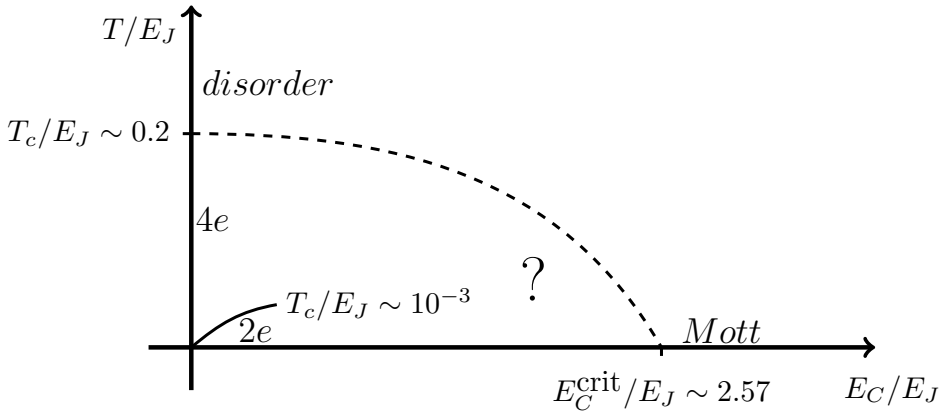

Figure 10.9.: Illustration of the conjectured phase structure.

very small difference in energy. We further identified the critical value E_C^{crit}/E_J at which the system enters a Mott phase.

Temperature-induced phase fluctuations do not lead to any vortex-ordering at $E_C = 0$ and finite temperature due to entropic protection of the degenerate ground states [183]. However, at $T = 0$ and finite E_C the lack of such entropic protection leads us to conclude that most likely an ordered vortex lattice will emerge with a $2e$-superconducting phase.

However, the stability of this vortex lattice state to finite temperature at small E_C is not completely clear. The entropic contribution of the many disordered ground states at $E_C = 0$ and $T = 0$ can be associated with the residual zero-temperature entropy of the triangular lattice anti-ferromagnetic Ising model s^0_{TLAIM} [183]. Hence, at finite temperature, due to this entropy contribution of the many-disordered ground states, we could expect to reenter the $4e$-superconducting phase and the vortex lattice to be destroyed around $T_c = \frac{\Delta e(E_C)}{s_{TLIM}}$. At this temperature, the entropic contribution dominates the energy-splitting $\Delta E(E_C)$, cf. Fig. 10.7b, due to finite E_C.

It should be noted that this critical temperature T_c at finite E_C might even be lower than the above estimate. This is because the vortex lattice could be destroyed by domain walls, whose energy penalties could be overcome at lower finite temperatures by their entropic contributions to the free energy.

From these results, we can conjecture that the $4e$-superconducting phase is stable at finite values of E_C/E_J, excluding at the very lowest temperature where a vortex lattice state might emerge.

To close, let us comment on the physical relevance of the sketched phase diagram. First, the influence of small values of E_C/E_J is important to study in general as a

possible perturbation that might be present in an experimental realization of JJAs that aim to study the case of $E_C = 0$. As such, it is helpful to understand the impact of a small finite charging energy on the phase structure. Additionally, with the emergence of the electrically tunable JJAs [174, 175, 176, 177, 178], the phase diagram at finite E_C/E_J can be studied in a single sample, which motivates the theoretical study of the phase diagram in this case.

Data

The data shown in this chapter is available in [197].

CHAPTER 11

An introduction to infinite projected entangled-pair state methods for variational ground state simulations using automatic differentiation

Authors: Jan Naumann*, **Erik Lennart Weerda***,
Matteo Rizzi, Jens Eisert, Philipp Schmoll

Year: 2024

Journal: SciPost Phyics Lecture Notes

Number: 86

DOI: 10.21468/SciPostPhysLectNotes.86

*Both first authors have contributed equally.

11.1 Summary and Context

In this publication, we present a practically minded introduction to variational optimization of infinite projected entangled pair states, alternatively referred to as infinite tensor product states, using automatic differentiation (AD).

To this end, we review the basic notions of infinite tensor product states, cf. part I of this thesis, and introduce the corner transfer renormalization group algorithm (CTMRG), cf. Sect. 4.1.1. We give an extensive introduction to AD, a tool from the machine learning community that we use to obtain the energy gradient in the context of infinite tensor product states [125]. We point out how to achieve a modified (element-wise) convergence of the CTMRG in practice, to be able to make use of the fixed-point of the CTMRG to

calculate the energy gradient efficiently [113]. In addition to this, we provide a set of useful practical suggestions to increase the stability and efficiency of the variational optimization of infinite tensor product states in this framework. Finally, we point out how to use the presented framework for infinite tensor product states on various non-square lattices and provide benchmark results for the comparison to other methods. An open-source implementation of the discussed concepts is provided alongside the publication.

In the context of this thesis, this publication should be seen as a contribution to the emerging framework of using AD in the context of ground state calculations with tensor product states. By focusing on practical aspects and methods to achieve a stable and efficient ground state search scheme, this publication adds a useful complement to the existing literature. The practical hints to make use of the fixed-point properties of the CTMRG for this purpose present an additional practical contribution. By comparing and discussing various benchmarks on several lattices, we also help to assess the power of the approach in several situations.

11.2 Authors Contribution

E. L. Weerda was one of the two major contributors to the practical insights presented in this publication and produced approximately half of the benchmarking results. He wrote a major part of the manuscript, in particular the sections concerning automatic differentiation and its efficient application for infinite TPS.

CHAPTER 12

Discussion

To conclude this thesis, we now discuss the content presented and the results obtained in a larger context. A major field of research in the study of condensed matter systems is concerned with the investigation of phenomena occurring when the systems' degrees of freedom are confined to two dimensions. Such two-dimensional settings are being studied both in the context of real materials and cold atom experiments for their promise of fascinating physical phenomena [198, 199, 200, 201].

The role of quantitative, numerical investigations is important in such situations, for example, to identify promising experimental parameters for the realization of particular phases of matter and to characterize their features and experimental signatures. Further, the effect of additional unwanted contributions to the Hamiltonians describing real experiments that go beyond idealized theoretical models can be studied numerically to assess their impact. In the context of cold atom experiments, the ability to perform faithful numerical calculations is crucial to create so-called "digital twins" of particular cold atom setups, which is useful for the calibration and benchmarking of these experiments.

The considerations above have motivated the development of a number of numerical approaches for these tasks, among which the tensor network states have proven particularly versatile and effective [15, 16, 17]. However, the techniques for the application of tensor networks in the two-dimensional setting are still in a stage of continuous development.

The results obtained in the context of this thesis can be categorized as methodological contributions towards the improvement of the toolkit of tensor networks in two dimensions, as well as applications thereof to a set of different physical scenarios.

To contribute to this effort of improving the methodological techniques, we have pre-

sented several results that were developed in the context of this thesis. We have proposed the split-CTMRG algorithm, cf. Chap. 8, which enables more efficient numerical calculations by reducing the dominant computational scaling involved in ground state calculations using the infinite tensor product states, cf. Sec. 2.2.1.

We hope that this algorithm, together with the practical schemes highlighted in Chap. 11 will contribute to the utility of the infinite tensor product states in particularly challenging physical situations where large bond-dimensions are necessary to understand the low-energy behaviour. This is particularly important to understand the phase structure in the thermodynamic limit in the presence of many competing phases. As examples of such situations, where a precise understanding of the phase structure can be important, we mention doped Hubbard models or models relevant for materials that might host spin-liquids as ground states [199, 202, 203].

Bridging the gap between method development and application was the goal of our investigations using the tensor product states on finite lattices, cf. Chap. 9. Here, we aimed to improve the efficiency of the optimization used for the tensor product states and to clarify the role of the difficulty of the contractions in the sampling framework for these states on finite lattices. However, we also demonstrated the particular utility of the tensor product states on finite lattices to serve, e.g., as "digital twins" for Rydberg atom array experiments.

In a complementary effort to the methodological developments, we have also applied the toolkit of the tensor product states to several challenging situations like spin systems in Chap. 6 and Chap. 7, models of Josephson junction arrays in Chap. 10, and a model of mobile bosonic particles on a lattice subject to a magnetic field in Chap. 5. Here, we would especially like to highlight that the infinite tensor product state method applied gives an important perspective from the thermodynamic limit in two dimensions. As such, it allows us to minimize the impact of finite size effects on the phase structure of the studied models. This is of particular interest, e.g., to understand to what degree exotic phases like the fractional quantum Hall states, which have now been observed in cold-atom experiments, are stabilized by the small finite size of the current experiments [95, 96]. It is important to study this question to understand if we can hope to identify and study these states also in the larger-scale future experiments. The investigation carried out to answer this question in Chap. 5 approached this question for the first time using the infinite tensor product states. The utilization of the state-of-the-art optimization techniques allowed for the treatment of these chiral topological phases using

the infinite tensor product state, cf. Sec. 3.2.4, thus offering the desired perspective from the thermodynamic limit.

In conclusion, we hope that the presented methodological and applied results of this thesis can be seen as helpful contributions towards the general tensor network program discussed in the introduction, cf. Chap. 1, and hence enable a deeper understanding of two-dimensional quantum matter using tensor networks.

Part III.

Appendix

APPENDIX A

The Toric Code Tensor Product State

A.1 Construction of the Ground State

The crucial feature of the Hamiltonian [72]

$$H_{\mathrm{TC}} = -\sum_{\{+\}} S_+ - \sum_{\{\square\}} P_\square, \tag{A.1}$$

is that all its terms are mutually commuting. This is obvious for the star- and plaquette-operators among themselves and remains true for commutators of star and plaquette operators because they can only have a shared support of either zero or two local Hilbert spaces, such that they commute, since $\sigma^x\sigma^z = -\sigma^z\sigma^x$. This wealth of operators commuting with the Hamiltonian (as they commute with all its terms individually) significantly aids in the explicit construction of the many-body ground state [72] of this Hamiltonian, because it mandates that such a many-body ground state be also the ground state of every term individually.

Starting with a star operator $S_+ = \sigma^z_{1+}\sigma^z_{2+}\sigma^z_{3+}\sigma^z_{4+}$, we notice that this operator has eigenvalues ± 1. The eigenstates corresponding to the eigenvalue $+1$ are product states in the z-basis, that have an even number (0,2,4) of local $|1\rangle$ configurations on the support of S_+. The eigenstates corresponding to the eigenvalues -1 are the product states with odd numbers (1,3). It follows that the ground states of the star operator terms in the toric code Hamiltonian are quite degenerate. Every product state in the z-basis that fulfills the "even-number" rule for the four spins on the surrounding edges of every vertex is a ground state of all star operators. A feature of these many degenerate ground states of the star operators is that we find edges on which we have a local configuration $|1\rangle$ will always form paths of closed loops due to the "even number" rule. Any open

path, as illustrated in Fig. 3.1b, will immediately break this rule, and such a state is hence no longer a ground state of the star operators.

Now it remains to choose the linear combination from these many ground states such that they also represent eigenstates of the plaquette operators. We can achieve this by taking an equal weight superposition of all allowed "closed-loop" product states $|C_i\rangle$

$$|\psi_{\mathrm{TC}}\rangle = \sum_i |C_i\rangle\,, \tag{A.2}$$

where i labels all the "closed-loop"-configurations. To verify that this is in fact an eigenstate of the plaquette operators, we simply note that every plaquette operator maps one configuration that fulfills the "closed-loop" rule to a different one, as it changes the value of either zero or two spins on the support of any star-operator. Hence, if we take the equal-weight superposition of all such configurations, we have in fact

$$P_\square \sum_i |C_i\rangle = \sum_i |C_i\rangle \qquad \forall \quad \square, \tag{A.3}$$

such that we have identified a ground state of H_{TC}.

APPENDIX B

Partition function of XY-models a a tensor network

In this appendix, we aim to illustrate the representation of the partition function of an XY-model as a two-dimensional tensor network. Here we outline a particular version of the construction of the partition function based on the works [192, 193], which aimed to improve the original formulation [191]. Note that representations of the partition function using tensor networks have been explored in the context of discrete variables [204, 205] but also have been pushed towards Heisenberg models [206, 207].

Once such a representation of the partition function is achieved, we can use many of the techniques for contraction, calculation of local observables and correlation functions, that have been introduced in Chap. 4 also in this classical context, by simply replacing the double layer tensors used in the context of quantum states by the single layer tensors resulting from the following procedure.

We start with the definition of the partition function of an XY-model on an arbitrary two-dimensional lattice

$$Z = \sum_i \exp\left(-\beta E_i\right) = \int \mathcal{D}\phi \exp\left(-\beta H(\{\phi\})\right), \tag{B.1}$$

$$\int \mathcal{D}\phi = \prod_i \int_{-\pi}^{\pi} \frac{d\phi_i}{2\pi}, \tag{B.2}$$

where we integrate over the classical variables located on the vertices of the lattice. We consider a Hamiltonian

$$H(\{\phi\}) = -J \sum_{\langle i,j \rangle} \cos\left(\phi_j - \phi_i - A_{ij}\right), \tag{B.3}$$

with $A_{ij} := \frac{2\pi}{\Phi_0} \int_i^j \vec{A} d\vec{s}$ as the integral over the vector potential $\vec{A}$ along the path from

vertex i to vertex j. With this definition, the argument of the cosine becomes gauge invariant with the transformations $\vec{A}' = \vec{A} + \frac{\Phi_0}{2\pi}\vec{\nabla}\chi(r)$ and $\phi(r)' = \phi(r) + \chi(r)$.

For the construction [192, 193] we describe here, we will reorder the Hamiltonian by organizing it as a sum over plaquettes of the lattice which we label by p

$$H(\{\phi\}) = \frac{-J}{2} \sum_{p \in \text{plaquettes}} \sum_{\langle i,j \rangle \in e(p)} \cos\left(\phi_j - \phi_i - A_{ij}\right), \tag{B.4}$$

and where $e(p)$ is the tuple of edges bordering the plaquete p. The factor $\frac{1}{2}$ comes from the fact that every edge belongs to two plaquettes. Thus, altogether we write

$$Z = \prod_i \int_{-\pi}^{\pi} \frac{d\phi_i}{2\pi} \prod_p \underbrace{\exp\left(\frac{\beta J}{2} \sum_{\langle i,j \rangle \in e(p)} \cos\left(\phi_j - \phi_i - A_{ij}\right)\right)}_{=:W_p}. \tag{B.5}$$

Consider the Boltzmann factors W_p associated with one plaquette p. Our goal is now to build up the partition function from objects defined for every plaquette. It can be useful to think of the object W_p as a tensor with four continuous indices as scetched in Fig. B.1. We can express W_p as

$$\begin{aligned} W_p(\phi_1, \phi_2, \phi_3, \phi_4) &= \exp\left(\frac{\beta J}{2} \sum_{\langle i,j \rangle \in e(p)} \cos\left(\phi_j - \phi_i - A_{ij}\right)\right) \\ &= \exp\Big(\frac{\beta J}{2} \big[\cos\left(\phi_2 - \phi_1 - A_{12}\right) + \cos\left(\phi_3 - \phi_2 - A_{23}\right) \\ &\quad + \cos\left(\phi_4 - \phi_3 - A_{34}\right) + \cos\left(\phi_1 - \phi_4 - A_{41}\right)\big]\Big). \end{aligned} \tag{B.6}$$

We will now use the identity

$$\exp\left(x \cos\left(\phi_k - \phi_l\right)\right) = \sum_{n=-\infty}^{\infty} I_n(x) \exp\left(in(\phi_k - \phi_l)\right) \tag{B.7}$$

to rewrite

$$\begin{aligned} W_p(\phi_1, \phi_2, \phi_3, \phi_4) = \sum_{n_1,n_2,n_3,n_4=-\infty}^{\infty} & I_{n_1}\left(\frac{\beta J}{2}\right) I_{n_2}\left(\frac{\beta J}{2}\right) I_{n_3}\left(\frac{\beta J}{2}\right) I_{n_3}\left(\frac{\beta J}{2}\right) \times \\ & e^{-i\left[n_1(\phi_1-\phi_2)+n_2(\phi_2-\phi_3)+n_3(\phi_3-\phi_4)+n_4(\phi_4-\phi_1)\right]} \times \\ & e^{-i\left(n_1 A_{12}+n_2 A_{23}+n_3 A_{34}+n_4 A_{41}\right)}. \end{aligned} \tag{B.8}$$

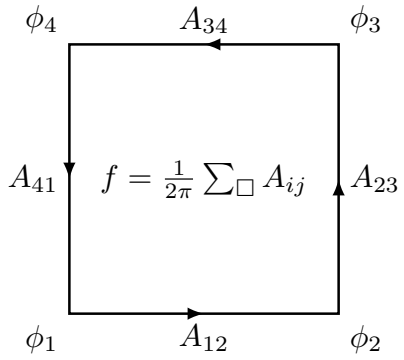

Figure B.1.: Illustration of the plaquette tensor W_p with four continuous indices $\phi_1, \phi_2, \phi_3, \phi_4$.

To obtain a tensor network of objects with discrete indices, it is useful to calculate the Fourier transform of the product of Boltzmann factors W_p, which is, as the variables ϕ are compact, now a tensor with discrete indices amenable to truncation

$$\begin{aligned} P_{m_1 m_2 m_3 m_4} :=& \prod_{i=1}^{4} \int \frac{d\phi_i}{2\pi} W_p(\phi_1, \phi_2, \phi_3, \phi_4) e^{-i(m_1\phi_1 + m_2\phi_2 + m_3\phi_3 + m_4\phi_4)} \\ =& \sum_{n_1,n_2,n_3,n_4} I_{n_1} I_{n_2} I_{n_3} I_{n_4} e^{-i\left(n_1 A_{12} + n_2 A_{23} + n_3 A_{34} + n_4 A_{41}\right)} \times \\ & \prod_{i=1}^{4} \int \frac{d\phi_i}{2\pi} e^{i\left[\phi_1(-n_1+n_4-m_1) + \phi_2(-n_2+n_1-m_2) + \phi_3(-n_3+n_2-m_3) + \phi_4(-n_4+n_3-m_4)\right]}, \end{aligned} \tag{B.9}$$

which, after performing the integrals $\int d\phi/(2\pi) e^{i\phi n} = \delta_{n,0}$ one by one leads to

$$\begin{aligned} P_{m_1 m_2 m_3 m_4} =& \sum_{n_4=-\infty}^{\infty} I_{n_4-m_1} I_{n_4-m_1-m_2} I_{n_4-m_1-m_2-m_3} I_{n_4} \times \\ & e^{i\left((m_1-n_4)A_{12} + (m_1+m_2-n_4)A_{23} + (m_1+m_2+m_3-n_4)A_{34} - n_4 A_{41}\right)} \delta_{m_1+m_2+m_3+m_4,0}. \end{aligned} \tag{B.10}$$

We find that the structure of P_{m_1,m_2,m_3,m_4} is such that we obtain only non-zero entries in the tensor if the Fourier variables (or $U(1)$-charges) m_1, m_2, m_3, m_4 are conserved on the level of the plaquette. However, no restriction has been made for the transport of $U(1)$ charges in the loop of the plaquette; rather, all of these contributions are summed here (sum over n_4). This fact stands in contrast to the conservation of $U(1)$-charge at

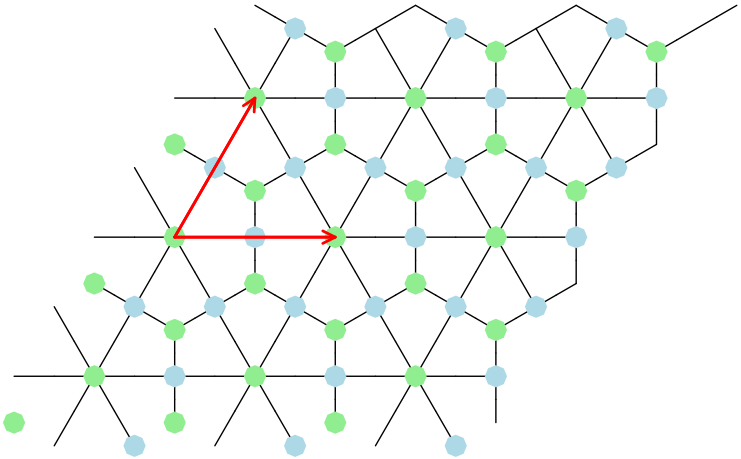

Figure B.2.: Illustration tensor-network structure of the partition function of the dice lattice. We obtain a vertex-plaquette lattice, where the vertices (green) are δ-tensors, while the plaquette tensors (blue) have the form, shown in Eq. B.10. We included the unit-cell vectors of the dice lattice (red) for clarity.

each vertex of the lattice in the conventional construction [191] of the partition function.

To use the discrete plaquette tensors P to rewrite the partition function in Eq. B.5, we need to account for the fact that multiple plaquettes of the lattice will contain the same variable ϕ_i if these plaquettes are adjacent to the same vertex i of the lattice. We illustrate this by considering one of the integrals of the partition function over the variable ϕ and assume that three plaquettes are bordering this vertex

$$\int \frac{d\phi}{2\pi} W_1(\{\phi\}_1, \phi) W_2(\{\phi\}_2, \phi) W_3(\{\phi\}_3, \phi) = \int \frac{d\phi}{2\pi} \prod_{i=1}^{3} \int d\phi_1 \delta(\phi - \phi_i) \times \\ W_1(\{\phi\}_1, \phi_1) W_2(\{\phi\}_2, \phi_2) W_3(\{\phi\}_3, \phi_3)$$

where we denote with $\{\phi\}_i$ all variables of W_i that we are not integrating over in the

above equation. Now we can use the identities

$$\delta(\phi-\phi_j)=\frac{1}{2\pi}\sum_{m\in\mathsf{Z}}e^{-im(\phi-\phi_j)}=\frac{1}{2\pi}\sum_{m\in\mathsf{Z}}U_m^\dagger(\phi)U_m(\phi_j),\qquad\text{with}\qquad U_m(\phi_j)=e^{-im\phi_j},$$
$$\delta_{n,m}=\int\frac{d\phi}{2\pi}U_m(\phi)U_n^\dagger(\phi) \tag{B.11}$$

to rewrite the above equation

$$\int\frac{d\phi}{2\pi}W_1(\{\phi\}_1,\phi)W_2(\{\phi\}_2,\phi)W_3(\{\phi\}_3,\phi)=\frac{1}{(2\pi)^3}\sum_{m_1,m_2,m_3\in\mathsf{Z}}\delta_{m_1+m_2+m_3,0}\prod_{i=1}^{3}\widetilde{P}_i(\{\phi\}_i,m_i), \tag{B.12}$$

where we use the tilde in $\widetilde{P}_i(\{\phi\}_i,m_i)$ to stress that here we have only Fourier transformed one of the continuous indices of the plaquette Boltzmann tensor. From this form we see that the integral over the continuous, periodic variable ϕ can be rewritten as a contraction of the discrete indices of $\widetilde{P}_i$ and a three-leg tensor $\delta_{m1+m2+m3,0}$ that ensures the conservation of $U(1)$-charges at the vertex.

By repeating this procedure for all integrals over the variables at the vertices of the lattice, the partition function of Eq B.5 becomes

$$Z\sim\mathrm{tTr}\left[\prod_i\delta[i]\prod_p P[p]\right], \tag{B.13}$$

again with i labeling the vertices of the lattice and p labeling the plaquettes. As every tensor in this tensor network conserves the $U(1)$-charges, the entire tensor network is invariant. We explicitly exploit this fact in the calculations to reduce memory load and improve efficiency, as discussed in Sec. 3.1.

We notice that the tensor-trace above involves δ-tensors on the vertices as well as plaquette tensors P in the plaquettes of the lattice in question. Hence, the structure formed by the tensors is what we will call the *vertex-plaquete lattice*. For the dice lattice, a drawing of this vertex-plaquete lattice is shown in Fig. B.2.

As an example to see how to obtain the free energy from the tensor network representation of the partition function using the CTMRG algorithm introduced in Sec. 4.1 see e.g. [206].

B.1 Reductio ad Quadratum

In order to contract this tensor network on the vertex-plaquette lattice with the contraction algorithms described in Chap. 4, we need to map it to the square lattice.

One way of achieving this involves first decomposing the six-leg δ-tensors, corresponding to the hub-vertices of the dice lattice as

$$\delta_{n_1+n_2+n_3+n_4+n_5+n_6,0} = \sum_{k,l=-2n_{\max}}^{2n_{\max}} \delta_{n_5+n_6,k}\delta_{n_1+n_4,-k+l}\delta_{n_2+n_3,-l}, \tag{B.14}$$

where $n_{\max}$ labels the truncated value we use in our tensor network. Using this decomposition we transform the tensor network from the original one, shown in Fig. B.3a to that shown in Fig. B.3b, where the six-leg tensor was replaced by two three leg tensors and a four leg tensors, which we illustrate in a darker green.

The next step of our mapping to the square lattice involves splitting two of the three plaquette tensors in the unit cell with a decomposition (e.g., a SVD) into two tensors. This operation takes us from Fig. B.3b to Fig. B.3c, where we show the tensors resulting from the decomposition in a darker blue.

At this point, we can group the tensors, which we illustrate in Fig. B.3d to get a resulting square lattice tensor network with a unit cell of size 2×3.

B.2 Details regarding the Numerical Results

For the numerical simulations shown in Fig. 10.2, we have chosen a local bond dimension of 41 for the local plaquette tensor P of the tensor network for the partition function. This corresponds to restricting the discrete indices in the plaquette tensor, cf. Eq. B.10, to $m \in \{-20, \ldots, 0, \ldots, 20\}$.
We perform the contraction of the tensor network for the partition function approximately using the CTMRG algorithm discussed in Chap.4. For that, we have to choose a finite environment bond dimension χ_E. In the results shown in Fig. 10.2 we use $\chi_E = 251$. To assess the degree of convergence in this environment bond dimension, we present the relative difference to the free energy calculated at $\chi_E = 201$ in Fig. B.4a. We find a relative difference on the order of $\Delta f/E_J \approx 10^{-5}$.

In order to investigate the convergence of our calculation in the cutoff of the local plaquette tensor P, we have repeated the calculation again with a cutoff corresponding to $m \in \{-15, \ldots, 0, \ldots, 15\}$ with a fixed environment bond dimension of $\chi_E = 251$. We

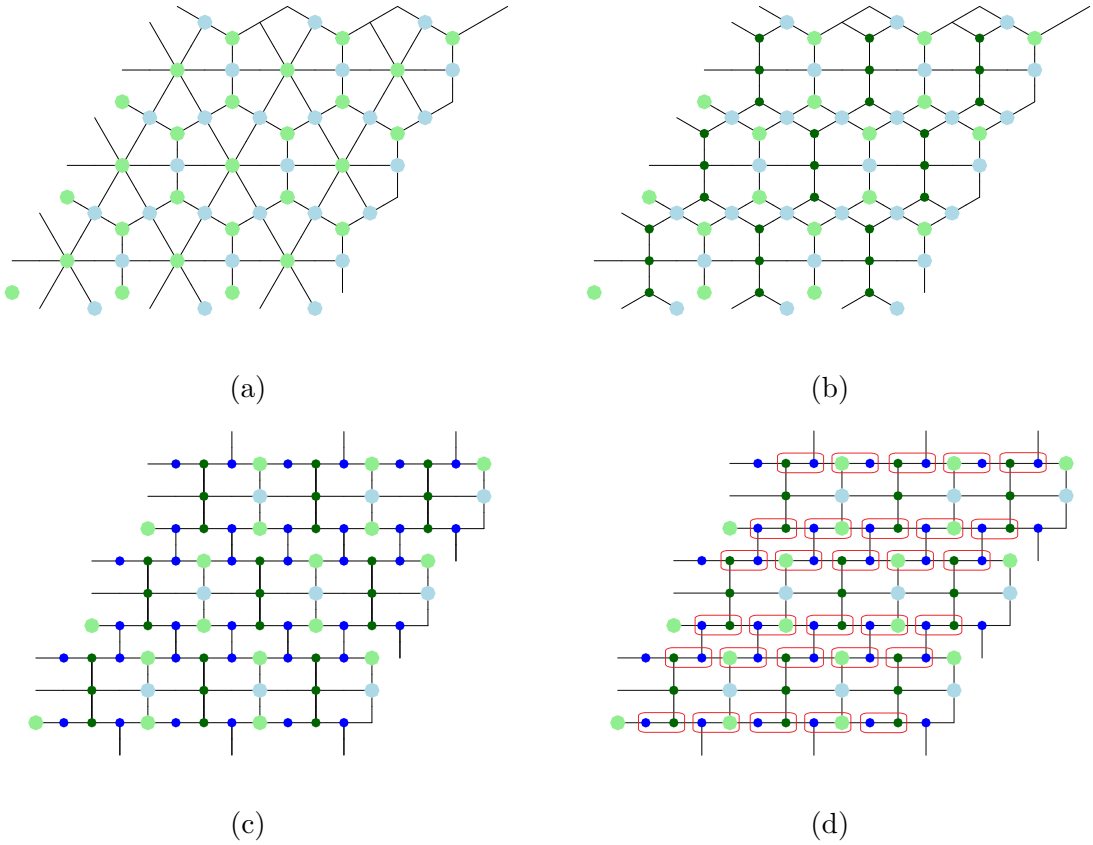

Figure B.3.: Here we show intermediate steps of the mapping from the plaquette-vertex lattice of the partition function to a square lattice geometry. Once we have the network in a square lattice form, we can apply the numerical techniques described in Chap. 4.

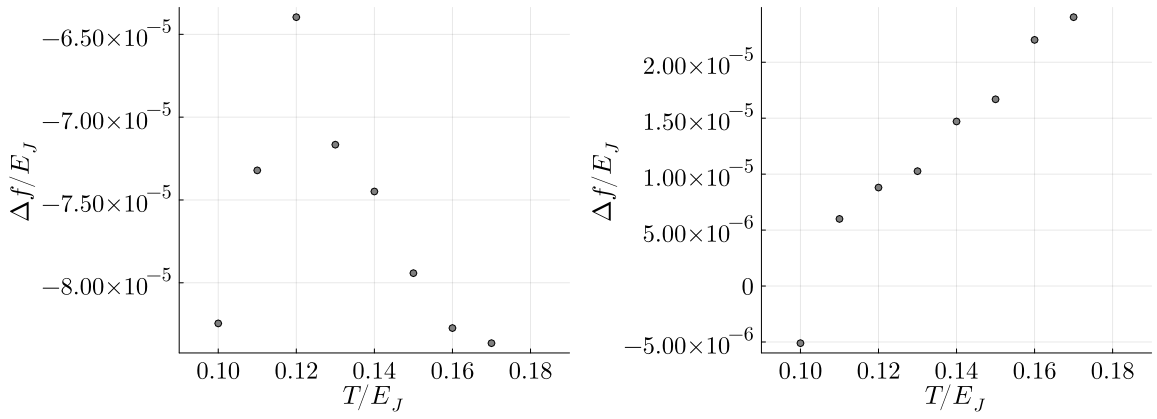

(a) (b)

Figure B.4.: a) Relative difference of the free energy density from the partition function for environment bond-dimension $\chi_E = 251$ and $\chi_E = 201$. A bond dimension of 41 was used for the local plaquette tensors P. b) Relative difference of the free-energy density from a partition function with plaquette tensors of local bond dimension 41, as compared to those with local bond dimension 31. An environment bond dimension of $\chi_E = 251$ was used.

show the relative difference in the free energy obtained for the two choices of cutoffs in Fig. B.4b. We find a relative difference on the order of $\Delta f/E_J \approx 10^{-5}$.

Let us note that we only show results for temperatures above $T/E_J = 0.1$. This is because we have experienced a sudden and drastic change in the convergence behaviour of the CTMRG algorithm at lower temperatures. We could imagine that this is related to the complexity phase transition for contracting two-dimensional tensor networks, as was observed in [208] and was investigated in the context of finite TPS also in publication [P5].

Bibliography

[1] Philip W Anderson. "More Is Different: Broken symmetry and the nature of the hierarchical structure of science." In: *Science* 177.4047 (1972), pp. 393–396.

[2] M. H. Anderson et al. "Observation of Bose-Einstein Condensation in a Dilute Atomic Vapor". In: *Science* 269.5221 (1995), pp. 198–201. DOI: 10.1126/science.269.5221.198. eprint: https://www.science.org/doi/pdf/10.1126/science.269.5221.198. URL: https://www.science.org/doi/abs/10.1126/science.269.5221.198.

[3] Pyotr Kapitza. "Viscosity of liquid helium below the λ-point". In: *Nature* 141.3558 (1938), pp. 74–74.

[4] Kamerlingh Onnes. "The resistance of pure mercury at helium temperatures". In: *Commun. Phys. Lab. Univ. Leiden, b* 120 (1911).

[5] Xiao-Gang Wen. "Topological orders in rigid states". In: *International Journal of Modern Physics B* 4.02 (1990), pp. 239–271.

[6] J. Bardeen, L. N. Cooper, and J. R. Schrieffer. "Microscopic Theory of Superconductivity". In: *Phys. Rev.* 106 (1 Apr. 1957), pp. 162–164. DOI: 10.1103/PhysRev.106.162. URL: https://link.aps.org/doi/10.1103/PhysRev.106.162.

[7] J. Bardeen, L. N. Cooper, and J. R. Schrieffer. "Theory of Superconductivity". In: *Phys. Rev.* 108 (5 Dec. 1957), pp. 1175–1204. DOI: 10.1103/PhysRev.108.1175. URL: https://link.aps.org/doi/10.1103/PhysRev.108.1175.

[8] R. B. Laughlin. "Anomalous Quantum Hall Effect: An Incompressible Quantum Fluid with Fractionally Charged Excitations". In: *Phys. Rev. Lett.* 50 (18 May 1983), pp. 1395–1398. DOI: 10.1103/PhysRevLett.50.1395. URL: https://link.aps.org/doi/10.1103/PhysRevLett.50.1395.

[9] Steven R. White. “Density matrix formulation for quantum renormalization groups”. In: *Phys. Rev. Lett.* 69 (19 Nov. 1992), pp. 2863–2866. DOI: 10.1103/PhysRevLett.69.2863. URL: https://link.aps.org/doi/10.1103/PhysRevLett.69.2863.

[10] J. Eisert, M. Cramer, and M. B. Plenio. “Colloquium: Area laws for the entanglement entropy”. In: *Rev. Mod. Phys.* 82 (1 Feb. 2010), pp. 277–306. DOI: 10.1103/RevModPhys.82.277. URL: https://link.aps.org/doi/10.1103/RevModPhys.82.277.

[11] Mark Fannes, Bruno Nachtergaele, and Reinhard F Werner. “Finitely correlated states on quantum spin chains”. In: *Communications in mathematical physics* 144 (1992), pp. 443–490.

[12] F. Verstraete and J. I. Cirac. *Renormalization algorithms for Quantum-Many Body Systems in two and higher dimensions*. 2004. arXiv: cond-mat/0407066 [cond-mat.str-el]. URL: https://arxiv.org/abs/cond-mat/0407066.

[13] G. Vidal. “Class of Quantum Many-Body States That Can Be Efficiently Simulated”. In: *Phys. Rev. Lett.* 101 (11 Sept. 2008), p. 110501. DOI: 10.1103/PhysRevLett.101.110501. URL: https://link.aps.org/doi/10.1103/PhysRevLett.101.110501.

[14] Y-Y Shi, L-M Duan, and Guifre Vidal. “Classical simulation of quantum many-body systems with a tree tensor network”. In: *Physical Review A—Atomic, Molecular, and Optical Physics* 74.2 (2006), p. 022320.

[15] Román Orús. “A practical introduction to tensor networks: Matrix product states and projected entangled pair states”. In: *Annals of Physics* 349 (2014), pp. 117–158. ISSN: 0003-4916. DOI: https://doi.org/10.1016/j.aop.2014.06.013. URL: https://www.sciencedirect.com/science/article/pii/S0003491614001596.

[16] Pietro Silvi et al. “The Tensor Networks Anthology: Simulation techniques for many-body quantum lattice systems”. In: *SciPost Phys. Lect. Notes* (2019), p. 8. DOI: 10.21468/SciPostPhysLectNotes.8. URL: https://scipost.org/10.21468/SciPostPhysLectNotes.8.

[17] Benedikt Bruognolo et al. “A beginner’s guide to non-abelian iPEPS for correlated fermions”. In: *SciPost Phys. Lect. Notes* (2021), p. 25. DOI: 10.21468/SciPostPhysLectNotes.25. URL: https://scipost.org/10.21468/SciPostPhysLectNotes.25.

[18] Jacob C Bridgeman and Christopher T Chubb. "Hand-waving and interpretive dance: an introductory course on tensor networks". In: *Journal of Physics A: Mathematical and Theoretical* 50.22 (May 2017), p. 223001. DOI: 10.1088/1751-8121/aa6dc3. URL: https://dx.doi.org/10.1088/1751-8121/aa6dc3.

[19] J. Ignacio Cirac et al. "Matrix product states and projected entangled pair states: Concepts, symmetries, theorems". In: *Rev. Mod. Phys.* 93 (4 Dec. 2021), p. 045003. DOI: 10.1103/RevModPhys.93.045003. URL: https://link.aps.org/doi/10.1103/RevModPhys.93.045003.

[20] Bei Zeng et al. *Quantum information meets quantum matter*. Springer, 2019.

[21] Lam Chi-Chung, P Sadayappan, and Rephael Wenger. "On optimizing a class of multi-dimensional loops with reduction for parallel execution". In: *Parallel Processing Letters* 7.02 (1997), pp. 157–168.

[22] L. MIRSKY. "SYMMETRIC GAUGE FUNCTIONS AND UNITARILY INVARIANT NORMS". In: *The Quarterly Journal of Mathematics* 11.1 (Jan. 1960), pp. 50–59. ISSN: 0033-5606. DOI: 10.1093/qmath/11.1.50. eprint: https://academic.oup.com/qjmath/article-pdf/11/1/50/7295335/11-1-50.pdf. URL: https://doi.org/10.1093/qmath/11.1.50.

[23] Zheng-Cheng Gu, Frank Verstraete, and Xiao-Gang Wen. "Grassmann tensor network states and its renormalization for strongly correlated fermionic and bosonic states". In: *arXiv preprint arXiv:1004.2563* (2010).

[24] Christina V Kraus et al. "Fermionic projected entangled pair states". In: *Physical Review A—Atomic, Molecular, and Optical Physics* 81.5 (2010), p. 052338.

[25] Philippe Corboz et al. "Simulation of interacting fermions with entanglement renormalization". In: *Physical Review A—Atomic, Molecular, and Optical Physics* 81.1 (2010), p. 010303.

[26] Nick Bultinck et al. "Fermionic matrix product states and one-dimensional topological phases". In: *Physical Review B* 95.7 (2017), p. 075108.

[27] Nick Bultinck et al. "Fermionic projected entangled-pair states and topological phases". In: *Journal of Physics A: Mathematical and Theoretical* 51.2 (2017), p. 025202.

[28] Quinten Mortier et al. "Fermionic tensor network methods". In: *SciPost Phys.* 18 (2025), p. 012. DOI: 10.21468/SciPostPhys.18.1.012. URL: https://scipost.org/10.21468/SciPostPhys.18.1.012.

[29] J. Jordan et al. “Classical Simulation of Infinite-Size Quantum Lattice Systems in Two Spatial Dimensions”. In: *Phys. Rev. Lett.* 101 (25 Dec. 2008), p. 250602. DOI: 10.1103/PhysRevLett.101.250602. URL: https://link.aps.org/doi/10.1103/PhysRevLett.101.250602.

[30] Wen-Yuan Liu et al. “Gradient optimization of finite projected entangled pair states”. In: *Phys. Rev. B* 95 (19 May 2017), p. 195154. DOI: 10.1103/PhysRevB.95.195154. URL: https://link.aps.org/doi/10.1103/PhysRevB.95.195154.

[31] Tom Vieijra et al. “Direct sampling of projected entangled-pair states”. In: *Phys. Rev. B* 104 (23 Dec. 2021), p. 235141. DOI: 10.1103/PhysRevB.104.235141. URL: https://link.aps.org/doi/10.1103/PhysRevB.104.235141.

[32] Ling Wang, Iztok Pižorn, and Frank Verstraete. “Monte Carlo simulation with tensor network states”. In: *Physical Review B—Condensed Matter and Materials Physics* 83.13 (2011), p. 134421.

[33] Wen-Yuan Liu et al. “Accurate simulation for finite projected entangled pair states in two dimensions”. In: *Physical Review B* 103.23 (2021), p. 235155.

[34] Michael P Zaletel and Frank Pollmann. “Isometric tensor network states in two dimensions”. In: *Physical review letters* 124.3 (2020), p. 037201.

[35] Xie-Hang Yu et al. “Dual-Isometric Projected Entangled Pair States”. In: *Phys. Rev. Lett.* 133 (19 Nov. 2024), p. 190401. DOI: 10.1103/PhysRevLett.133.190401. URL: https://link.aps.org/doi/10.1103/PhysRevLett.133.190401.

[36] F. Verstraete, D. Porras, and J. I. Cirac. “Density Matrix Renormalization Group and Periodic Boundary Conditions: A Quantum Information Perspective”. In: *Phys. Rev. Lett.* 93 (22 Nov. 2004), p. 227205. DOI: 10.1103/PhysRevLett.93.227205. URL: https://link.aps.org/doi/10.1103/PhysRevLett.93.227205.

[37] Nicolas Laflorencie. “Quantum entanglement in condensed matter systems”. In: *Physics Reports* 646 (2016). Quantum entanglement in condensed matter systems, pp. 1–59. ISSN: 0370-1573. DOI: https://doi.org/10.1016/j.physrep.2016.06.008. URL: https://www.sciencedirect.com/science/article/pii/S0370157316301582.

[38] Steven M Girvin and Kun Yang. *Modern condensed matter physics*. Cambridge University Press, 2019.

[39] Don N Page. “Average entropy of a subsystem”. In: *Physical review letters* 71.9 (1993), p. 1291.

[40] Siddhartha Sen. "Average entropy of a quantum subsystem". In: *Physical review letters* 77.1 (1996), p. 1.

[41] Valerie Coffman, Joydip Kundu, and William K. Wootters. "Distributed entanglement". In: *Phys. Rev. A* 61 (5 Apr. 2000), p. 052306. DOI: 10.1103/PhysRevA.61.052306. URL: https://link.aps.org/doi/10.1103/PhysRevA.61.052306.

[42] Tobias J. Osborne and Frank Verstraete. "General Monogamy Inequality for Bipartite Qubit Entanglement". In: *Phys. Rev. Lett.* 96 (22 June 2006), p. 220503. DOI: 10.1103/PhysRevLett.96.220503. URL: https://link.aps.org/doi/10.1103/PhysRevLett.96.220503.

[43] Matthew B Hastings and Tohru Koma. "Spectral gap and exponential decay of correlations". In: *Communications in mathematical physics* 265 (2006), pp. 781–804.

[44] M B Hastings. "An area law for one-dimensional quantum systems". In: *Journal of Statistical Mechanics: Theory and Experiment* 2007.08 (Aug. 2007), P08024. DOI: 10.1088/1742-5468/2007/08/P08024. URL: https://dx.doi.org/10.1088/1742-5468/2007/08/P08024.

[45] M. B. Hastings. "Entropy and entanglement in quantum ground states". In: *Phys. Rev. B* 76 (3 July 2007), p. 035114. DOI: 10.1103/PhysRevB.76.035114. URL: https://link.aps.org/doi/10.1103/PhysRevB.76.035114.

[46] Yimin Ge and Jens Eisert. "Area laws and efficient descriptions of quantum many-body states". In: *New Journal of Physics* 18.8 (Aug. 2016), p. 083026. DOI: 10.1088/1367-2630/18/8/083026. URL: https://dx.doi.org/10.1088/1367-2630/18/8/083026.

[47] Junping Shao et al. "Entanglement Entropy of the $\nu = 1/2$ Composite Fermion Non-Fermi Liquid State". In: *Phys. Rev. Lett.* 114 (20 May 2015), p. 206402. DOI: 10.1103/PhysRevLett.114.206402. URL: https://link.aps.org/doi/10.1103/PhysRevLett.114.206402.

[48] Brian Swingle and T. Senthil. "Universal crossovers between entanglement entropy and thermal entropy". In: *Phys. Rev. B* 87 (4 Jan. 2013), p. 045123. DOI: 10.1103/PhysRevB.87.045123. URL: https://link.aps.org/doi/10.1103/PhysRevB.87.045123.

[49] Michael M. Wolf. "Violation of the Entropic Area Law for Fermions". In: *Phys. Rev. Lett.* 96 (1 Jan. 2006), p. 010404. DOI: 10.1103/PhysRevLett.96.010404. URL: https://link.aps.org/doi/10.1103/PhysRevLett.96.010404.

[50] Dimitri Gioev and Israel Klich. "Entanglement Entropy of Fermions in Any Dimension and the Widom Conjecture". In: *Phys. Rev. Lett.* 96 (10 Mar. 2006), p. 100503. DOI: 10.1103/PhysRevLett.96.100503. URL: https://link.aps.org/doi/10.1103/PhysRevLett.96.100503.

[51] Wenxin Ding, Alexander Seidel, and Kun Yang. "Entanglement Entropy of Fermi Liquids via Multidimensional Bosonization". In: *Phys. Rev. X* 2 (1 Mar. 2012), p. 011012. DOI: 10.1103/PhysRevX.2.011012. URL: https://link.aps.org/doi/10.1103/PhysRevX.2.011012.

[52] L. Pastur and V. Slavin. "Area Law Scaling for the Entropy of Disordered Quasifree Fermions". In: *Phys. Rev. Lett.* 113 (15 Oct. 2014), p. 150404. DOI: 10.1103/PhysRevLett.113.150404. URL: https://link.aps.org/doi/10.1103/PhysRevLett.113.150404.

[53] Andrew C. Potter. *Boundary-law scaling of entanglement entropy in diffusive metals*. 2014. arXiv: 1408.1094 [cond-mat.str-el]. URL: https://arxiv.org/abs/1408.1094.

[54] Hsin-Hua Lai, Kun Yang, and N. E. Bonesteel. "Violation of the Entanglement Area Law in Bosonic Systems with Bose Surfaces: Possible Application to Bose Metals". In: *Phys. Rev. Lett.* 111 (21 Nov. 2013), p. 210402. DOI: 10.1103/PhysRevLett.111.210402. URL: https://link.aps.org/doi/10.1103/PhysRevLett.111.210402.

[55] Max A Metlitski and Tarun Grover. "Entanglement entropy of systems with spontaneously broken continuous symmetry". In: *arXiv preprint arXiv:1112.5166* (2011).

[56] P.W. Anderson. "Resonating valence bonds: A new kind of insulator?" In: *Materials Research Bulletin* 8.2 (1973), pp. 153–160. ISSN: 0025-5408. DOI: https://doi.org/10.1016/0025-5408(73)90167-0. URL: https://www.sciencedirect.com/science/article/pii/0025540873901670.

[57] P. W. Anderson. "The Resonating Valence Bond State in La2CuO4 and Superconductivity". In: *Science* 235.4793 (1987), pp. 1196–1198. DOI: 10.1126/science.235.4793.1196. eprint: https://www.science.org/doi/pdf/10.1126/science.235.4793.1196. URL: https://www.science.org/doi/abs/10.1126/science.235.4793.1196.

[58] F. Verstraete et al. “Criticality, the Area Law, and the Computational Power of Projected Entangled Pair States”. In: *Phys. Rev. Lett.* 96 (22 June 2006), p. 220601. DOI: 10.1103/PhysRevLett.96.220601. URL: https://link.aps.org/doi/10.1103/PhysRevLett.96.220601.

[59] Ying Tang, Anders W. Sandvik, and Christopher L. Henley. “Properties of resonating-valence-bond spin liquids and critical dimer models”. In: *Phys. Rev. B* 84 (17 Nov. 2011), p. 174427. DOI: 10.1103/PhysRevB.84.174427. URL: https://link.aps.org/doi/10.1103/PhysRevB.84.174427.

[60] M. Cramer et al. “Entanglement-area law for general bosonic harmonic lattice systems”. In: *Phys. Rev. A* 73 (1 Jan. 2006), p. 012309. DOI: 10.1103/PhysRevA.73.012309. URL: https://link.aps.org/doi/10.1103/PhysRevA.73.012309.

[61] Quinten Mortier et al. “Tensor Networks Can Resolve Fermi Surfaces”. In: *Phys. Rev. Lett.* 129 (20 Nov. 2022), p. 206401. DOI: 10.1103/PhysRevLett.129.206401. URL: https://link.aps.org/doi/10.1103/PhysRevLett.129.206401.

[62] F. Verstraete and J. I. Cirac. “Matrix product states represent ground states faithfully”. In: *Phys. Rev. B* 73 (9 Mar. 2006), p. 094423. DOI: 10.1103/PhysRevB.73.094423. URL: https://link.aps.org/doi/10.1103/PhysRevB.73.094423.

[63] Adrián Franco-Rubio and J. Ignacio Cirac. “Gaussian matrix product states cannot efficiently describe critical systems”. In: *Phys. Rev. B* 106 (23 Dec. 2022), p. 235136. DOI: 10.1103/PhysRevB.106.235136. URL: https://link.aps.org/doi/10.1103/PhysRevB.106.235136.

[64] Norbert Schuch et al. “Computational Complexity of Projected Entangled Pair States”. In: *Phys. Rev. Lett.* 98 (14 Apr. 2007), p. 140506. DOI: 10.1103/PhysRevLett.98.140506. URL: https://link.aps.org/doi/10.1103/PhysRevLett.98.140506.

[65] David Perez-Garcia et al. “Matrix Product State Representations”. In: *Quantum Information & Computation* 7 (July 2007), pp. 401–430. DOI: 10.26421/QIC7.5-6-1.

[66] D Perez-Garcia et al. “PEPS as unique ground states of local Hamiltonians”. In: *Quantum Information and Computation* 8.6&7 (2008), pp. 650–663. DOI: https://doi.org/10.26421/QIC8.6-7-6.

[67] G. Scarpa et al. “Projected Entangled Pair States: Fundamental Analytical and Numerical Limitations”. In: *Phys. Rev. Lett.* 125 (21 Nov. 2020), p. 210504. DOI: 10.1103/PhysRevLett.125.210504. URL: https://link.aps.org/doi/10.1103/PhysRevLett.125.210504.

[68] D Pérez-García et al. “Characterizing symmetries in a projected entangled pair state”. In: *New Journal of Physics* 12.2 (Feb. 2010), p. 025010. DOI: 10.1088/1367-2630/12/2/025010. URL: https://dx.doi.org/10.1088/1367-2630/12/2/025010.

[69] Andras Molnar et al. “A generalization of the injectivity condition for projected entangled pair states”. In: *Journal of Mathematical Physics* 59.2 (2018).

[70] Xie Chen, Zheng-Cheng Gu, and Xiao-Gang Wen. “Complete classification of one-dimensional gapped quantum phases in interacting spin systems”. In: *Phys. Rev. B* 84 (23 Dec. 2011), p. 235128. DOI: 10.1103/PhysRevB.84.235128. URL: https://link.aps.org/doi/10.1103/PhysRevB.84.235128.

[71] Norbert Schuch, David Pérez-García, and Ignacio Cirac. “Classifying quantum phases using matrix product states and projected entangled pair states”. In: *Phys. Rev. B* 84 (16 Oct. 2011), p. 165139. DOI: 10.1103/PhysRevB.84.165139. URL: https://link.aps.org/doi/10.1103/PhysRevB.84.165139.

[72] A.Yu. Kitaev. “Fault-tolerant quantum computation by anyons”. In: *Annals of Physics* 303.1 (2003), pp. 2–30. ISSN: 0003-4916. DOI: https://doi.org/10.1016/S0003-4916(02)00018-0. URL: https://www.sciencedirect.com/science/article/pii/S0003491602000180.

[73] Ian P McCulloch. “From density-matrix renormalization group to matrix product states”. In: *Journal of Statistical Mechanics: Theory and Experiment* 2007.10 (Oct. 2007), P10014. DOI: 10.1088/1742-5468/2007/10/P10014. URL: https://dx.doi.org/10.1088/1742-5468/2007/10/P10014.

[74] Sukhwinder Singh, Robert N. C. Pfeifer, and Guifré Vidal. “Tensor network decompositions in the presence of a global symmetry”. In: *Phys. Rev. A* 82 (5 Nov. 2010), p. 050301. DOI: 10.1103/PhysRevA.82.050301. URL: https://link.aps.org/doi/10.1103/PhysRevA.82.050301.

[75] Sukhwinder Singh, Robert N. C. Pfeifer, and Guifre Vidal. “Tensor network states and algorithms in the presence of a global U(1) symmetry”. In: *Phys. Rev. B* 83 (11 Mar. 2011), p. 115125. DOI: 10.1103/PhysRevB.83.115125. URL: https://link.aps.org/doi/10.1103/PhysRevB.83.115125.

[76] Andreas Weichselbaum. "Non-abelian symmetries in tensor networks: A quantum symmetry space approach". In: *Annals of Physics* 327.12 (2012), pp. 2972–3047. ISSN: 0003-4916. DOI: https://doi.org/10.1016/j.aop.2012.07.009. URL: https://www.sciencedirect.com/science/article/pii/S0003491612001121.

[77] David A Huse and Veit Elser. "Simple variational wave functions for two-dimensional heisenberg spin-1/2 antiferromagnets". In: *Physical review letters* 60.24 (1988), p. 2531.

[78] Steven R White and AL Chernyshev. "Neél order in square and triangular lattice Heisenberg models". In: *Physical review letters* 99.12 (2007), p. 127004.

[79] Leon Balents. "Spin liquids in frustrated magnets". In: *nature* 464.7286 (2010), pp. 199–208.

[80] Norbert Schuch et al. "Resonating valence bond states in the PEPS formalism". In: *Phys. Rev. B* 86 (11 Sept. 2012), p. 115108. DOI: 10.1103/PhysRevB.86.115108. URL: https://link.aps.org/doi/10.1103/PhysRevB.86.115108.

[81] Zhenyu Zhou, Julia Wildeboer, and Alexander Seidel. "Ground-state uniqueness of the twelve-site RVB spin-liquid parent Hamiltonian on the kagome lattice". In: *Phys. Rev. B* 89 (3 Jan. 2014), p. 035123. DOI: 10.1103/PhysRevB.89.035123. URL: https://link.aps.org/doi/10.1103/PhysRevB.89.035123.

[82] Zheng-Cheng Gu et al. "Tensor-product representations for string-net condensed states". In: *Phys. Rev. B* 79 (8 Feb. 2009), p. 085118. DOI: 10.1103/PhysRevB.79.085118. URL: https://link.aps.org/doi/10.1103/PhysRevB.79.085118.

[83] S. P. G. Crone and P. Corboz. "Detecting a Z_2 topologically ordered phase from unbiased infinite projected entangled-pair state simulations". In: *Phys. Rev. B* 101 (11 Mar. 2020), p. 115143. DOI: 10.1103/PhysRevB.101.115143. URL: https://link.aps.org/doi/10.1103/PhysRevB.101.115143.

[84] Brian Swingle and Xiao-Gang Wen. "Topological properties of tensor network states from their local gauge and local symmetry structures". In: *arXiv preprint arXiv:1001.4517* (2010).

[85] Norbert Schuch, Ignacio Cirac, and David Pérez-García. "PEPS as ground states: Degeneracy and topology". In: *Annals of Physics* 325.10 (2010), pp. 2153–2192. ISSN: 0003-4916. DOI: https://doi.org/10.1016/j.aop.2010.05.008. URL: https://www.sciencedirect.com/science/article/pii/S0003491610000990.

[86] Xie Chen et al. “Tensor product representation of a topological ordered phase: Necessary symmetry conditions”. In: *Phys. Rev. B* 82 (16 Oct. 2010), p. 165119. DOI: 10.1103/PhysRevB.82.165119. URL: https://link.aps.org/doi/10.1103/PhysRevB.82.165119.

[87] Oliver Buerschaper, Miguel Aguado, and Guifré Vidal. “Explicit tensor network representation for the ground states of string-net models”. In: *Phys. Rev. B* 79 (8 Feb. 2009), p. 085119. DOI: 10.1103/PhysRevB.79.085119. URL: https://link.aps.org/doi/10.1103/PhysRevB.79.085119.

[88] N. Bultinck et al. “Anyons and matrix product operator algebras”. In: *Annals of Physics* 378 (2017), pp. 183–233. ISSN: 0003-4916. DOI: https://doi.org/10.1016/j.aop.2017.01.004. URL: https://www.sciencedirect.com/science/article/pii/S0003491617300040.

[89] M. Z. Hasan and C. L. Kane. “Colloquium: Topological insulators”. In: *Rev. Mod. Phys.* 82 (4 Nov. 2010), pp. 3045–3067. DOI: 10.1103/RevModPhys.82.3045. URL: https://link.aps.org/doi/10.1103/RevModPhys.82.3045.

[90] T. B. Wahl et al. “Projected Entangled-Pair States Can Describe Chiral Topological States”. In: *Phys. Rev. Lett.* 111 (23 Dec. 2013), p. 236805. DOI: 10.1103/PhysRevLett.111.236805. URL: https://link.aps.org/doi/10.1103/PhysRevLett.111.236805.

[91] J. Dubail and N. Read. “Tensor network trial states for chiral topological phases in two dimensions and a no-go theorem in any dimension”. In: *Phys. Rev. B* 92 (20 Nov. 2015), p. 205307. DOI: 10.1103/PhysRevB.92.205307. URL: https://link.aps.org/doi/10.1103/PhysRevB.92.205307.

[92] Christina V Kraus et al. “Fermionic projected entangled pair states”. In: *Physical Review A—Atomic, Molecular, and Optical Physics* 81.5 (2010), p. 052338.

[93] Nicola Marzari et al. “Maximally localized Wannier functions: Theory and applications”. In: *Reviews of Modern Physics* 84.4 (2012), pp. 1419–1475.

[94] Christian Brouder et al. “Exponential localization of Wannier functions in insulators”. In: *Physical review letters* 98.4 (2007), p. 046402.

[95] Julian Léonard et al. “Realization of a fractional quantum Hall state with ultracold atoms”. In: *Nature* (2023), pp. 1–5.

[96] Philipp Lunt et al. “Realization of a Laughlin State of Two Rapidly Rotating Fermions”. In: *Phys. Rev. Lett.* 133 (25 Dec. 2024), p. 253401. DOI: 10.1103/PhysRevLett.133.253401. URL: https://link.aps.org/doi/10.1103/PhysRevLett.133.253401.

[97] Juraj Hasik et al. “Simulating Chiral Spin Liquids with Projected Entangled-Pair States”. In: *Phys. Rev. Lett.* 129 (17 Oct. 2022), p. 177201. DOI: 10.1103/PhysRevLett.129.177201. URL: https://link.aps.org/doi/10.1103/PhysRevLett.129.177201.

[98] Michael Lubasch, J Ignacio Cirac, and Mari-Carmen Banuls. “Unifying projected entangled pair state contractions”. In: *New Journal of Physics* 16.3 (2014), p. 033014.

[99] Michael Levin and Cody P Nave. “Tensor renormalization group approach to two-dimensional classical lattice models”. In: *Physical review letters* 99.12 (2007), p. 120601.

[100] Zhi-Yuan Xie et al. “Second renormalization of tensor-network states”. In: *Physical review letters* 103.16 (2009), p. 160601.

[101] Hui-Hai Zhao et al. “Renormalization of tensor-network states”. In: *Physical Review B—Condensed Matter and Materials Physics* 81.17 (2010), p. 174411.

[102] Zhi-Yuan Xie et al. “Coarse-graining renormalization by higher-order singular value decomposition”. In: *Physical Review B—Condensed Matter and Materials Physics* 86.4 (2012), p. 045139.

[103] Glen Evenbly and Guifre Vidal. “Tensor network renormalization”. In: *Physical review letters* 115.18 (2015), p. 180405.

[104] V. Zauner-Stauber et al. “Variational optimization algorithms for uniform matrix product states”. In: *Phys. Rev. B* 97 (4 Jan. 2018), p. 045145. DOI: 10.1103/PhysRevB.97.045145. URL: https://link.aps.org/doi/10.1103/PhysRevB.97.045145.

[105] Alexander Nietner et al. “Efficient variational contraction of two-dimensional tensor networks with a non-trivial unit cell”. In: *Quantum* 4 (2020), p. 328.

[106] Tomotoshi Nishino and Kouichi Okunishi. “Corner transfer matrix renormalization group method”. In: *Journal of the Physical Society of Japan* 65.4 (1996), pp. 891–894.

[107] Tomotoshi Nishino and Kouichi Okunishi. "Corner transfer matrix algorithm for classical renormalization group". In: *Journal of the Physical Society of Japan* 66.10 (1997), pp. 3040–3047.

[108] Román Orús and Guifré Vidal. "Simulation of two-dimensional quantum systems on an infinite lattice revisited: Corner transfer matrix for tensor contraction". In: *Physical Review B—Condensed Matter and Materials Physics* 80.9 (2009), p. 094403.

[109] Philippe Corboz, Jacob Jordan, and Guifré Vidal. "Simulation of fermionic lattice models in two dimensions with projected entangled-pair states: Next-nearest neighbor Hamiltonians". In: *Physical Review B—Condensed Matter and Materials Physics* 82.24 (2010), p. 245119.

[110] Philippe Corboz et al. "Stripes in the two-dimensional t-J model with infinite projected entangled-pair states". In: *Phys. Rev. B* 84 (4 July 2011), p. 041108. DOI: 10.1103/PhysRevB.84.041108. URL: https://link.aps.org/doi/10.1103/PhysRevB.84.041108.

[111] Philippe Corboz, T Maurice Rice, and Matthias Troyer. "Competing states in the t-J model: Uniform d-wave state versus stripe state". In: *Physical review letters* 113.4 (2014), p. 046402.

[112] MT Fishman et al. "Faster methods for contracting infinite two-dimensional tensor networks". In: *Physical Review B* 98.23 (2018), p. 235148.

[113] Boris Ponsioen, Fakher F Assaad, and Philippe Corboz. "Automatic differentiation applied to excitations with projected entangled pair states". In: *SciPost Physics* 12.1 (2022), p. 006.

[114] Anna Francuz, Norbert Schuch, and Bram Vanhecke. "Stable and efficient differentiation of tensor network algorithms". In: *Phys. Rev. Res.* 7 (1 Mar. 2025), p. 013237. DOI: 10.1103/PhysRevResearch.7.013237. URL: https://link.aps.org/doi/10.1103/PhysRevResearch.7.013237.

[115] IV Lukin and AG Sotnikov. "Variational optimization of tensor-network states with the honeycomb-lattice corner transfer matrix". In: *Physical Review B* 107.5 (2023), p. 054424.

[116] Samuel Nyckees et al. "Critical line of the triangular Ising antiferromagnet in a field from a C 3-symmetric corner transfer matrix algorithm". In: *Physical Review E* 108.6 (2023), p. 064132.

[117] IV Lukin and AG Sotnikov. "Corner transfer matrix renormalization group approach in the zoo of Archimedean lattices". In: *Physical Review E* 109.4 (2024), p. 045305.

[118] Zhi-Yuan Xie et al. "Tensor renormalization of quantum many-body systems using projected entangled simplex states". In: *Physical Review X* 4.1 (2014), p. 011025.

[119] Philipp Schmoll et al. "Fine grained tensor network methods". In: *Physical review letters* 124.20 (2020), p. 200603.

[120] H. C. Jiang, Z. Y. Weng, and T. Xiang. "Accurate Determination of Tensor Network State of Quantum Lattice Models in Two Dimensions". In: *Phys. Rev. Lett.* 101 (9 Aug. 2008), p. 090603. DOI: 10.1103/PhysRevLett.101.090603. URL: https://link.aps.org/doi/10.1103/PhysRevLett.101.090603.

[121] Philippe Corboz et al. "Simulation of strongly correlated fermions in two spatial dimensions with fermionic projected entangled-pair states". In: *Phys. Rev. B* 81 (16 Apr. 2010), p. 165104. DOI: 10.1103/PhysRevB.81.165104. URL: https://link.aps.org/doi/10.1103/PhysRevB.81.165104.

[122] Ho N. Phien et al. "Infinite projected entangled pair states algorithm improved: Fast full update and gauge fixing". In: *Phys. Rev. B* 92 (3 July 2015), p. 035142. DOI: 10.1103/PhysRevB.92.035142. URL: https://link.aps.org/doi/10.1103/PhysRevB.92.035142.

[123] Philippe Corboz. "Variational optimization with infinite projected entangled-pair states". In: *Phys. Rev. B* 94 (3 July 2016), p. 035133. DOI: 10.1103/PhysRevB.94.035133. URL: https://link.aps.org/doi/10.1103/PhysRevB.94.035133.

[124] Laurens Vanderstraeten et al. "Gradient methods for variational optimization of projected entangled-pair states". In: *Phys. Rev. B* 94 (15 Oct. 2016), p. 155123. DOI: 10.1103/PhysRevB.94.155123. URL: https://link.aps.org/doi/10.1103/PhysRevB.94.155123.

[125] Hai-Jun Liao et al. "Differentiable Programming Tensor Networks". In: *Phys. Rev. X* 9 (3 Sept. 2019), p. 031041. DOI: 10.1103/PhysRevX.9.031041. URL: https://link.aps.org/doi/10.1103/PhysRevX.9.031041.

[126] M. Scheb and R. M. Noack. "Finite projected entangled pair states for the Hubbard model". In: *Phys. Rev. B* 107 (16 Apr. 2023), p. 165112. DOI: 10.1103/PhysRevB.107.165112. URL: https://link.aps.org/doi/10.1103/PhysRevB.107.165112.

[127] Jutho Haegeman et al. “Time-Dependent Variational Principle for Quantum Lattices”. In: *Phys. Rev. Lett.* 107 (7 Aug. 2011), p. 070601. DOI: 10.1103/PhysRevLett.107.070601. URL: https://link.aps.org/doi/10.1103/PhysRevLett.107.070601.

[128] Laurens Vanderstraeten, Jutho Haegeman, and Frank Verstraete. “Tangent-space methods for uniform matrix product states”. In: *SciPost Phys. Lect. Notes* (2019), p. 7. DOI: 10.21468/SciPostPhysLectNotes.7. URL: https://scipost.org/10.21468/SciPostPhysLectNotes.7.

[129] Saeed S. Jahromi and Román Orús. “Universal tensor-network algorithm for any infinite lattice”. In: *Phys. Rev. B* 99 (19 May 2019), p. 195105. DOI: 10.1103/PhysRevB.99.195105. URL: https://link.aps.org/doi/10.1103/PhysRevB.99.195105.

[130] Zhou-Quan Wan and Shi-Xin Zhang. *Automatic Differentiation for Complex Valued SVD*. 2019. arXiv: 1909.02659 [math.NA]. URL: https://arxiv.org/abs/1909.02659.

[131] Frederik Wilde et al. *Scalably learning quantum many-body Hamiltonians from dynamical data*. 2022. arXiv: 2209.14328 [quant-ph]. URL: https://arxiv.org/abs/2209.14328.

[132] Anna Francuz, Norbert Schuch, and Bram Vanhecke. *Stable and efficient differentiation of tensor network algorithms*. 2023. arXiv: 2311.11894 [quant-ph]. URL: https://arxiv.org/abs/2311.11894.

[133] Jorge Nocedal and Stephen J. Wright. “Line Search Methods”. In: *Numerical Optimization*. New York, NY: Springer New York, 2006, pp. 30–65. ISBN: 978-0-387-40065-5.

[134] Jorge Nocedal and Stephen J. Wright. “Quasi Newton Methods”. In: *Numerical Optimization*. New York, NY: Springer New York, 2006, pp. 135–163. ISBN: 978-0-387-40065-5.

[135] Alexei Kitaev. “Anyons in an exactly solved model and beyond”. In: *Annals of Physics* 321.1 (2006). January Special Issue, pp. 2–111. ISSN: 0003-4916. DOI: https://doi.org/10.1016/j.aop.2005.10.005. URL: https://www.sciencedirect.com/science/article/pii/S0003491605002381.

[136] Marek M Rams, Piotr Czarnik, and Lukasz Cincio. "Precise extrapolation of the correlation function asymptotics in uniform tensor network states with application to the Bose-Hubbard and XXZ models". In: *Physical Review X* 8.4 (2018), p. 041033.

[137] Bram Vanhecke et al. "Scaling hypothesis for matrix product states". In: *Physical Review Letters* 123.25 (2019), p. 250604.

[138] Boris Ponsioen and Philippe Corboz. "Excitations with projected entangled pair states using the corner transfer matrix method". In: *Phys. Rev. B* 101 (19 May 2020), p. 195109. DOI: 10.1103/PhysRevB.101.195109. URL: https://link.aps.org/doi/10.1103/PhysRevB.101.195109.

[139] Boris Ponsioen, Juraj Hasik, and Philippe Corboz. "Improved summations of n-point correlation functions of projected entangled-pair states". In: *Phys. Rev. B* 108 (19 Nov. 2023), p. 195111. DOI: 10.1103/PhysRevB.108.195111. URL: https://link.aps.org/doi/10.1103/PhysRevB.108.195111.

[140] Wei-Lin Tu et al. "Generating Function for Projected Entangled-Pair States". In: *PRX Quantum* 5 (1 Mar. 2024), p. 010335. DOI: 10.1103/PRXQuantum.5.010335. URL: https://link.aps.org/doi/10.1103/PRXQuantum.5.010335.

[141] J. Ignacio Cirac et al. "Entanglement spectrum and boundary theories with projected entangled-pair states". In: *Phys. Rev. B* 83 (24 June 2011), p. 245134. DOI: 10.1103/PhysRevB.83.245134. URL: https://link.aps.org/doi/10.1103/PhysRevB.83.245134.

[142] Hui Li and F. D. M. Haldane. "Entanglement Spectrum as a Generalization of Entanglement Entropy: Identification of Topological Order in Non-Abelian Fractional Quantum Hall Effect States". In: *Phys. Rev. Lett.* 101 (1 July 2008), p. 010504. DOI: 10.1103/PhysRevLett.101.010504. URL: https://link.aps.org/doi/10.1103/PhysRevLett.101.010504.

[143] N. Regnault. *Entanglement Spectroscopy and its Application to the Quantum Hall Effects*. 2015. arXiv: 1510.07670 [cond-mat.str-el]. URL: https://arxiv.org/abs/1510.07670.

[144] Jutho Haegeman and Frank Verstraete. "Diagonalizing Transfer Matrices and Matrix Product Operators: A Medley of Exact and Computational Methods". In: *Annual Review of Condensed Matter Physics* 8.Volume 8, 2017 (2017), pp. 355–406. ISSN: 1947-5462. DOI: https://doi.org/10.1146/annurev-conmatphys-

031016-025507. URL: https://www.annualreviews.org/content/journals/10.1146/annurev-conmatphys-031016-025507.

[145] Jutho Haegeman et al. "Elementary Excitations in Gapped Quantum Spin Systems". In: *Phys. Rev. Lett.* 111 (8 Aug. 2013), p. 080401. DOI: 10.1103/PhysRevLett.111.080401. URL: https://link.aps.org/doi/10.1103/PhysRevLett.111.080401.

[146] Alexei Kitaev and John Preskill. "Topological Entanglement Entropy". In: *Phys. Rev. Lett.* 96 (11 Mar. 2006), p. 110404. DOI: 10.1103/PhysRevLett.96.110404. URL: https://link.aps.org/doi/10.1103/PhysRevLett.96.110404.

[147] Michael Levin and Xiao-Gang Wen. "Detecting Topological Order in a Ground State Wave Function". In: *Phys. Rev. Lett.* 96 (11 Mar. 2006), p. 110405. DOI: 10.1103/PhysRevLett.96.110405. URL: https://link.aps.org/doi/10.1103/PhysRevLett.96.110405.

[148] Steven T. Flammia et al. "Topological Entanglement Rényi Entropy and Reduced Density Matrix Structure". In: *Phys. Rev. Lett.* 103 (26 Dec. 2009), p. 261601. DOI: 10.1103/PhysRevLett.103.261601. URL: https://link.aps.org/doi/10.1103/PhysRevLett.103.261601.

[149] M. Aidelsburger et al. "Experimental Realization of Strong Effective Magnetic Fields in an Optical Lattice". In: *Phys. Rev. Lett.* 107 (25 Dec. 2011), p. 255301. DOI: 10.1103/PhysRevLett.107.255301. URL: https://link.aps.org/doi/10.1103/PhysRevLett.107.255301.

[150] M. Aidelsburger et al. "Realization of the Hofstadter Hamiltonian with Ultracold Atoms in Optical Lattices". In: *Phys. Rev. Lett.* 111 (18 Oct. 2013), p. 185301. DOI: 10.1103/PhysRevLett.111.185301. URL: https://link.aps.org/doi/10.1103/PhysRevLett.111.185301.

[151] Hirokazu Miyake et al. "Realizing the Harper Hamiltonian with Laser-Assisted Tunneling in Optical Lattices". In: *Phys. Rev. Lett.* 111 (18 Oct. 2013), p. 185302. DOI: 10.1103/PhysRevLett.111.185302. URL: https://link.aps.org/doi/10.1103/PhysRevLett.111.185302.

[152] Marcos Atala et al. "Observation of chiral currents with ultracold atoms in bosonic ladders". In: *Nature Physics* 10.8 (2014), pp. 588–593.

[153] M Eric Tai et al. "Microscopy of the interacting Harper–Hofstadter model in the two-body limit". In: *Nature* 546.7659 (2017), pp. 519–523.

[154] Anne EB Nielsen, Germán Sierra, and J Ignacio Cirac. "Local models of fractional quantum Hall states in lattices and physical implementation". In: *Nature communications* 4.1 (2013), p. 2864.

[155] V Kalmeyer and RB Laughlin. "Equivalence of the resonating-valence-bond and fractional quantum Hall states". In: *Physical review letters* 59.18 (1987), p. 2095.

[156] Steven R White. "Density matrix formulation for quantum renormalization groups". In: *Physical review letters* 69.19 (1992), p. 2863.

[157] Erik Lennart Weerda. *Data for further optimization of the ladder-model.* Zenodo, June 2025. DOI: 10.5281/zenodo.15674451. URL: https://doi.org/10.5281/zenodo.15674451.

[158] Frank C Hawthorne, Mitsuyoshi Kimata, and Raymond K Eby. "The crystal structure of spangolite, a complex copper sulfate sheet mineral". In: *American Mineralogist* 78.5-6 (1993), pp. 649–652.

[159] Filippo Olmi, Cesare Sabelli, and Renza Trosti-Ferroni. "The crystal structure of sabelliite". In: *European Journal of Mineralogy* 7.6 (1995), pp. 1331–1337.

[160] SJ Mills et al. "Bluebellite and mojaveite, two new minerals from the central Mojave Desert, California, USA". In: *Mineralogical Magazine* 78.5 (2014), pp. 1325–1340.

[161] Anthony R Kampf et al. "Lead-tellurium oxysalts from Otto Mountain near Baker, California: VIII. Fuettererite, Pb3Cu62+ Te6+ O6 (OH) 7Cl5, a new mineral with double spangolite-type sheets". In: *American Mineralogist* 98.2-3 (2013), pp. 506–511.

[162] SJ Mills et al. "Bluebellite and mojaveite, two new minerals from the central Mojave Desert, California, USA". In: *Mineralogical Magazine* 78.5 (2014), pp. 1325–1340.

[163] Lasse Gresista et al. "Candidate quantum disordered intermediate phase in the Heisenberg antiferromagnet on the maple-leaf lattice". In: *Physical Review B* 108.24 (2023), p. L241116.

[164] Juraj Hasik and Philippe Corboz. "Incommensurate Order with Translationally Invariant Projected Entangled-Pair States: Spiral States and Quantum Spin Liquid on the Anisotropic Triangular Lattice". In: *Phys. Rev. Lett.* 133 (17 Oct. 2024), p. 176502. DOI: 10.1103/PhysRevLett.133.176502. URL: https://link.aps.org/doi/10.1103/PhysRevLett.133.176502.

[165] Jonas Beck et al. “Phase diagram of the J-J d Heisenberg model on the maple leaf lattice: Neural networks and density matrix renormalization group”. In: *Physical Review B* 109.18 (2024), p. 184422.

[166] Damian JJ Farnell et al. “Quantum s= 1 2 antiferromagnets on Archimedean lattices: The route from semiclassical magnetic order to nonmagnetic quantum states”. In: *Physical Review B* 89.18 (2014), p. 184407.

[167] Jutho Haegeman et al. “Time-dependent variational principle for quantum lattices”. In: *Physical review letters* 107.7 (2011), p. 070601.

[168] Giuseppe Carleo and Matthias Troyer. “Solving the quantum many-body problem with artificial neural networks”. In: *Science* 355.6325 (2017), pp. 602–606.

[169] Laurens Vanderstraeten, Jutho Haegeman, and Frank Verstraete. “Tangent-space methods for uniform matrix product states”. In: *SciPost Physics Lecture Notes* (2019), p. 007.

[170] Ao Chen and Markus Heyl. “Empowering deep neural quantum states through efficient optimization”. In: *Nature Physics* 20.9 (2024), pp. 1476–1481.

[171] Henning Labuhn et al. “Tunable two-dimensional arrays of single Rydberg atoms for realizing quantum Ising models”. In: *Nature* 534.7609 (2016), pp. 667–670.

[172] Sepehr Ebadi et al. “Quantum phases of matter on a 256-atom programmable quantum simulator”. In: *Nature* 595.7866 (2021), pp. 227–232.

[173] Rosario Fazio and Herre van der Zant. “Quantum phase transitions and vortex dynamics in superconducting networks”. In: *Physics Reports* 355.4 (2001), pp. 235–334. ISSN: 0370-1573. DOI: https://doi.org/10.1016/S0370-1573(01)00022-9. URL: https://www.sciencedirect.com/science/article/pii/S0370157301000229.

[174] P Krogstrup et al. “Epitaxy of semiconductor–superconductor nanowires”. In: *Nature materials* 14.4 (2015), pp. 400–406.

[175] Javad Shabani et al. “Two-dimensional epitaxial superconductor-semiconductor heterostructures: A platform for topological superconducting networks”. In: *Physical Review B* 93.15 (2016), p. 155402.

[176] CGL Bøttcher et al. “Superconducting, insulating and anomalous metallic regimes in a gated two-dimensional semiconductor–superconductor array”. In: *Nature Physics* 14.11 (2018), pp. 1138–1144.

[177] CGL Bøttcher et al. “Berezinskii-Kosterlitz-Thouless transition and anomalous metallic phase in a hybrid Josephson junction array”. In: *Physical Review B* 110.18 (2024), p. L180502.

[178] CGL Bøttcher et al. “Dynamical vortex transitions in a gate-tunable two-dimensional Josephson junction array”. In: *Physical Review B* 108.13 (2023), p. 134517.

[179] Bill Sutherland. “Localization of electronic wave functions due to local topology”. In: *Phys. Rev. B* 34 (8 Oct. 1986), pp. 5208–5211. DOI: 10.1103/PhysRevB.34.5208. URL: https://link.aps.org/doi/10.1103/PhysRevB.34.5208.

[180] Julien Vidal, Rémy Mosseri, and Benoit Douçot. “Aharonov-Bohm cages in two-dimensional structures”. In: *Physical review letters* 81.26 (1998), p. 5888.

[181] Matteo Rizzi, Vittorio Cataudella, and Rosario Fazio. “Phase diagram of the Bose-Hubbard model with $\mathcal{T}_3$ symmetry”. In: *Phys. Rev. B* 73 (14 Apr. 2006), p. 144511. DOI: 10.1103/PhysRevB.73.144511. URL: https://link.aps.org/doi/10.1103/PhysRevB.73.144511.

[182] G. Möller and N. R. Cooper. “Correlated Phases of Bosons in the Flat Lowest Band of the Dice Lattice”. In: *Phys. Rev. Lett.* 108 (4 Jan. 2012), p. 045306. DOI: 10.1103/PhysRevLett.108.045306. URL: https://link.aps.org/doi/10.1103/PhysRevLett.108.045306.

[183] S. E. Korshunov. “Uniformly Frustrated XY Model without a Vortex-Pattern Ordering”. In: *Phys. Rev. Lett.* 94 (8 Mar. 2005), p. 087001. DOI: 10.1103/PhysRevLett.94.087001. URL: https://link.aps.org/doi/10.1103/PhysRevLett.94.087001.

[184] G. H. Wannier. “Antiferromagnetism. The Triangular Ising Net”. In: *Phys. Rev.* 79 (2 July 1950), pp. 357–364. DOI: 10.1103/PhysRev.79.357. URL: https://link.aps.org/doi/10.1103/PhysRev.79.357.

[185] Christopher L Henley. “Ordering due to disorder in a frustrated vector antiferromagnet”. In: *Physical review letters* 62.17 (1989), p. 2056.

[186] D. H. Lee and G. Grinstein. “Strings in two-dimensional classical XY models”. In: *Phys. Rev. Lett.* 55 (5 July 1985), pp. 541–544. DOI: 10.1103/PhysRevLett.55.541. URL: https://link.aps.org/doi/10.1103/PhysRevLett.55.541.

[187] S. A. Kivelson, V. J. Emery, and H. Q. Lin. “Doped antiferromagnets in the weak-hopping limit”. In: *Phys. Rev. B* 42 (10 Oct. 1990), pp. 6523–6530. DOI: 10.1103/PhysRevB.42.6523. URL: https://link.aps.org/doi/10.1103/PhysRevB.42.6523.

[188] Erez Berg, Eduardo Fradkin, and Steven A Kivelson. "Charge-4 e superconductivity from pair-density-wave order in certain high-temperature superconductors". In: *Nature Physics* 5.11 (2009), pp. 830–833.

[189] Shao-Kai Jian, Yingyi Huang, and Hong Yao. "Charge-4e Superconductivity from Nematic Superconductors in Two and Three Dimensions". In: *Phys. Rev. Lett.* 127 (22 Nov. 2021), p. 227001. DOI: 10.1103/PhysRevLett.127.227001. URL: https://link.aps.org/doi/10.1103/PhysRevLett.127.227001.

[190] C. C. Abilio et al. "Magnetic Field Induced Localization in a Two-Dimensional Superconducting Wire Network". In: *Phys. Rev. Lett.* 83 (24 Dec. 1999), pp. 5102–5105. DOI: 10.1103/PhysRevLett.83.5102. URL: https://link.aps.org/doi/10.1103/PhysRevLett.83.5102.

[191] Laurens Vanderstraeten et al. "Approaching the Kosterlitz-Thouless transition for the classical XY model with tensor networks". In: *Phys. Rev. E* 100 (6 Dec. 2019), p. 062136. DOI: 10.1103/PhysRevE.100.062136. URL: https://link.aps.org/doi/10.1103/PhysRevE.100.062136.

[192] Feng-Feng Song and Guang-Ming Zhang. "Tensor network approach to the fully frustrated XY model on a kagome lattice with a fractional vortex-antivortex pairing transition". In: *Phys. Rev. B* 108 (1 July 2023), p. 014424. DOI: 10.1103/PhysRevB.108.014424. URL: https://link.aps.org/doi/10.1103/PhysRevB.108.014424.

[193] Feng-Feng Song, Tong-Yu Lin, and Guang-Ming Zhang. "General tensor network theory for frustrated classical spin models in two dimensions". In: *Phys. Rev. B* 108 (22 Dec. 2023), p. 224404. DOI: 10.1103/PhysRevB.108.224404. URL: https://link.aps.org/doi/10.1103/PhysRevB.108.224404.

[194] Alexander Altland and Ben D Simons. *Condensed matter field theory*. Cambridge university press, 2010.

[195] N. D. Mermin and H. Wagner. "Absence of Ferromagnetism or Antiferromagnetism in One- or Two-Dimensional Isotropic Heisenberg Models". In: *Phys. Rev. Lett.* 17 (22 Nov. 1966), pp. 1133–1136. DOI: 10.1103/PhysRevLett.17.1133. URL: https://link.aps.org/doi/10.1103/PhysRevLett.17.1133.

[196] V. Cataudella and R. Fazio. "Glassy dynamics of Josephson arrays on a dice lattice". In: *Europhysics Letters* 61.3 (Feb. 2003), p. 341. DOI: 10.1209/epl/i2003-00180-y. URL: https://dx.doi.org/10.1209/epl/i2003-00180-y.

[197] Erik Lennart Weerda. *Data for dice chapter*. Zenodo, June 2025. DOI: 10.5281/zenodo.15684143. URL: https://doi.org/10.5281/zenodo.15684143.

[198] C. Broholm et al. "Quantum spin liquids". In: *Science* 367.6475 (2020), eaay0668. DOI: 10.1126/science.aay0668. eprint: https://www.science.org/doi/pdf/10.1126/science.aay0668. URL: https://www.science.org/doi/abs/10.1126/science.aay0668.

[199] Simon Trebst and Ciarán Hickey. "Kitaev materials". In: *Physics Reports* 950 (2022). Kitaev materials, pp. 1–37. ISSN: 0370-1573. DOI: https://doi.org/10.1016/j.physrep.2021.11.003. URL: https://www.sciencedirect.com/science/article/pii/S0370157321004051.

[200] Immanuel Bloch, Jean Dalibard, and Wilhelm Zwerger. "Many-body physics with ultracold gases". In: *Rev. Mod. Phys.* 80 (3 July 2008), pp. 885–964. DOI: 10.1103/RevModPhys.80.885. URL: https://link.aps.org/doi/10.1103/RevModPhys.80.885.

[201] Sylvain Nascimbene. "Simulating quantum Hall physics in ultracold atomic gases: prospects and challenges". In: *Comptes Rendus. Physique* 26.G1 (2025), pp. 317–338.

[202] Mingpu Qin et al. "The Hubbard Model: A Computational Perspective". In: *Annual Review of Condensed Matter Physics* 13.Volume 13, 2022 (2022), pp. 275–302. ISSN: 1947-5462. DOI: https://doi.org/10.1146/annurev-conmatphys-090921-033948. URL: https://www.annualreviews.org/content/journals/10.1146/annurev-conmatphys-090921-033948.

[203] M. R. Norman. "Colloquium: Herbertsmithite and the search for the quantum spin liquid". In: *Rev. Mod. Phys.* 88 (4 Dec. 2016), p. 041002. DOI: 10.1103/RevModPhys.88.041002. URL: https://link.aps.org/doi/10.1103/RevModPhys.88.041002.

[204] H. H. Zhao et al. "Renormalization of tensor-network states". In: *Phys. Rev. B* 81 (17 May 2010), p. 174411. DOI: 10.1103/PhysRevB.81.174411. URL: https://link.aps.org/doi/10.1103/PhysRevB.81.174411.

[205] Bram Vanhecke et al. "Solving frustrated Ising models using tensor networks". In: *Phys. Rev. Res.* 3 (1 Jan. 2021), p. 013041. DOI: 10.1103/PhysRevResearch.3.013041. URL: https://link.aps.org/doi/10.1103/PhysRevResearch.3.013041.

[206] Philipp Schmoll et al. “The classical two-dimensional Heisenberg model revisited: An $SU(2)$-symmetric tensor network study”. In: *SciPost Phys.* 11 (2021), p. 098. DOI: 10.21468/SciPostPhys.11.5.098. URL: https://scipost.org/10.21468/SciPostPhys.11.5.098.

[207] Lander Burgelman et al. “Contrasting pseudocriticality in the classical two-dimensional Heisenberg and RP^2 models: Zero-temperature phase transition versus finite-temperature crossover”. In: *Phys. Rev. E* 107 (1 Jan. 2023), p. 014117. DOI: 10.1103/PhysRevE.107.014117. URL: https://link.aps.org/doi/10.1103/PhysRevE.107.014117.

[208] Jielun Chen et al. “Sign Problem in Tensor-Network Contraction”. In: *PRX Quantum* 6 (1 Jan. 2025), p. 010312. DOI: 10.1103/PRXQuantum.6.010312. URL: https://link.aps.org/doi/10.1103/PRXQuantum.6.010312.